THE PERFORMANCE OF A 22 GHz RADIO TELESCOPE

A thesis submitted for the degree of Master of Science at

Rhodes University, Grahamstown

by

MICHAEL JOHN GAYLARD

Supervisor: Prof. E.E. Baart

November 1976

ACKNOWLEDGEMENTS

My thanks for their advice and help during this work go to the leaders of the radio astronomy group, Prof. E.E. Baart, Dr. G. de Jager and Clive Way-Jones, and to the many members of the Physics department who have assisted the project. From the staff these include Ron Arnott, Angus Barnard, Owen Campbell, Del Gillam, Dr. Georg Gruber, Jörg Lichtenburg, Joey MacKay, Billy Ndwebisa and Moses Sixaba, while the students who have participated in the development of the telescope are Pete Mountfort, Laurie Mutch, Brian Nunn, and Graham Oberem.

I would particularly like to thank Dr. J.W.M. Baars for the many useful comments and suggestions on the testing of the telescope which he provided during his visit to Rhodes in 1975.

The financial support of the Beit Trust, Mr. J.K. Bennie, the Charelick Salomon Scholarship Fund, the CSIR grant, and my parents, has been greatly appreciated and without which this thesis would not have been possible.

In conclusion, I am very grateful to Sheri Lambert for her invaluable aid, to Daisy Turner for her excellent typing.

Mike Gaylard

CONTENTS

CHAPTER ONE

THE 22 GHz TELESCOPE 1

CHAPTER TWO

THE ANTENNA

2.1 Introduction 4

2.2 Initial paraboloid measurements 4

2.3 The necessity for a paraboloid surface survey 6

2.4 The triangulation instrument 7

2.5 The template measuring system 8

2.6 The paraboloid surveys 11

2.7 Accuracy of the surveys 16

2.8 Summary of improvements to the paraboloid 17

2.9 The subreflector 19

2.10 Gravitational deformation of the antenna 20

2.11 Thermal effects on the antenna 26

CHAPTER THREE

THE FRONT END

3.1 Introduction 30

3.2 General description of the front end 30

3.3 Continuum studies 33

3.4 Spectral line studies 33

3.5 The initial front end layout 36

3.6 Early operation of the front end 38

3.7 Microwave component testing 39

3.8 Mixer temperature measurements using the noise tube 40

3.9 Determination of the mixer temperature using liquid air 43

3.10 Measurements of the mixer power output 47

3.11 The final front end layout 50

CHAPTER FOUR

THE CONTINUUM AND SPECTRAL LINE RECEIVERS

4.1 The Continuum receiver 54

4.2 The spectral line receiver 57

4.3 The automatic gain controls 59

4.4 The system sensitivity 62

CHAPTER FIVE

OBSERVATIONS WITH THE TELESCOPE

5.1 Introduction 66

5.2 The predicted solar temperature at 22 GHz 67

5.3 The predicted lunar temperature and its variation at 22 GHz 68

5.4 Atmospheric attenuation theory at 22 GHz 69

5.5 Atmospheric attenuation measurements 71

5.6 Continuum observation theory 73

5.7 Corrections to observations for the aperture efficiency 74

5.8 Solar and lunar observations prior to the front end reconstruction 76

5.9 Later solar observations 78

5.10 Later lunar observations 83

5.11 The antenna efficiency 83

CHAPTER SIX

THE CONVOLUTION PROGRAM AND THE ANTENNA BEAM PATTERN

6.1 Introduction 86

6.2 General description of program CONVOLVE 87

6.3 Convolution theory and its application to the program 88

6.4 The program source guidance routine 90

6.5 Solar and lunar transit scaling for the program 90

6.6 The beam pattern models 94

6.7 Factors affecting the beam pattern 95

CHAPTER SEVEN

A SUMMARY OF THE TELESCOPE DEVELOPMENT 101

LITERATURE CITED 103

APPENDICES

2a Thermal effects in the paraboloid survey 110

2b Antenna structure deformation 112

2c Antenna structure deformation by subreflector supports 113

3a Specifications of microwave components 115

3b Production of waveguide bends 117

4a Specifications of intermediate frequency components 118

6a Listing of program CONVOLVE 119

ABSTRACT

The performance of the Rhodes 22 GHz radio telescope and its improvement are discussed in this thesis. The reflector surfaces of the Cassegrain antenna were surveyed and the surface errors minimised, while the magnitude of thermal and gravitational deformations was calculated. The design and operation of the microwave front end has been improved, and the mixer performance characterised. The continuum and spectral line receivers and their sensitivity are described. The aperture efficiency, which has been raised from 0,47 to 0,57, was deduced from solar and lunar observations and atmospheric attenuation measurements. The antenna beam pattern was also obtained from the observations, with the aid of a computer program, and is compared to that predicted for the telescope.

CHAPTER ONE

THE 22 GHz TELESCOPE

The Rhodes telescope was designed to be suitable for both continuum and spectral line measurements. The operating frequency was chosen to enable it to be used for a sky survey to locate new Galactic water maser emission sources, for which the multichannel spectral line receiver was built. The continuum capability was incorporated primarily for the study of objects within the solar system.

Masering occurs when water molecules in interstellar clouds are 'pumped' to a high energy state, resulting in a population inversion compared to the normal thermal distribution. The transition from the higher energy 6_{16} state to the lower 5_{23} state, where the quantum numbers refer to the angular momentum of the molecule, is accompanied by microwave radiation at a frequency of 22,23508 GHz. The same transition, in absorption, is responsible for much of the atmospheric attenuation of cosmic signals at this frequency. The masers are associated particularly with young H II regions and star formation (Lo et al., 1975), but also with late M type red dwarf stars (Schwartz and Barrett, 1970). Their properties have been summarised by Sullivan (1973) and Haar and Pelling (1975): they may be very intense, up to 80 000 Jy, are variable on a timescale of weeks, show little polarisation, and are frequently associated with OH masers. Each source may exhibit a range of velocities of up to 200 km s^{-1} (Goss et al., 1976) which corresponds to a frequency range of 15 MHz, due to the doppler shift. However the main structure normally lies within a range of 1 to 2 MHz, and this defined the 2,5 MHz bandwidth

of the spectral line receiver. The maser pump mechanism is probably the excitation of H_2O rotational or vibrational states either by collisions with H_2 molecules, or by infra-red radiation, followed by infra-red emission and relaxation to the 6_{16} state.

Two continuum sources visible without long integration times are the sun and moon. Venus also falls into this category when near inferior conjunction. In each case thermal radiation is being detected: from the solar chromosphere, the top layer of the lunar surface, and the venusian atmosphere. Sources such as M17 (474 Jy) and Orion A (295 Jy) (Janssen et al., 1974) would be detectable after several minutes integration.

The telescope uses a 1,86 m diameter Cassegrain antenna (figure 1.1). Measurements of the antenna surface and its improvement are described in Chapter two, while its efficiency and sidelobe levels are discussed in Chapters five and six. The 'front end' microwave detection system (Chapter three) uses beam- and frequency-switching for continuum and spectral line observations respectively. The operation and sensitivity of the two receivers is described in Chapter four, and Chapter five contains details of observations. Finally, progress made with the telescope is summarised in Chapter seven.

figure 1.1 THE 22 GHz TELESCOPE LAYOUT

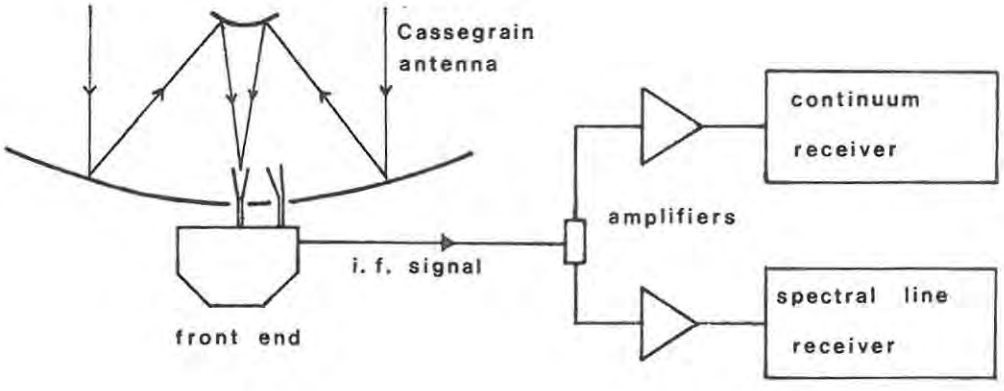

CHAPTER TWO

THE ANTENNA

2.1 Introduction

2.2 Initial paraboloid measurements

2.3 The necessity for a paraboloid surface survey

2.4 The triangulation instrument

2.5 The template measuring system

2.6 The paraboloid surveys

2.7 Accuracy of the surveys

2.8 Summary of improvements to the paraboloid

2.9 The subreflector

2.10 Gravitational deformation of the antenna

2.11 Thermal effects on the antenna

CHAPTER TWO

THE ANTENNA

2.1 Introduction

The antenna is a conventional Cassegrain with a 1,86 m diameter 'dish' and a 0,21 m diameter hyperboloid subreflector (figure 1.1). The incoming radiation is received by two microwave horns, one axially mounted and the other displaced laterally in the same focal plane. In this chapter the instruments that were built to measure the paraboloid surface in order to increase its accuracy and raise its efficiency are described. The contour maps obtained are depicted and the improvements to the surface enumerated. The subreflector surface errors were also measured. Gravitational deformation of the antenna and the effect of temperature variations on the focusing were analyzed to determine whether there could be a significant degradation of the aperture efficiency.

2.2 Initial Paraboloid Measurements

To ensure accurate placing of the microwave horns at the secondary focus the focal length of the paraboloid was measured using a steel beam and steel ruler (figure 2.1). The beam was clamped across opposite corners of the octagonal dish support framework, and the depth at a given radius was measured by the ruler, which was held in a steel block with a locking screw. Readings were taken along eight radii at 50,0 mm intervals, providing eighteen points per radius.

The equation of the paraboloid surface is given by

figure 2.1 THE FIRST DISH MEASURING SYSTEM

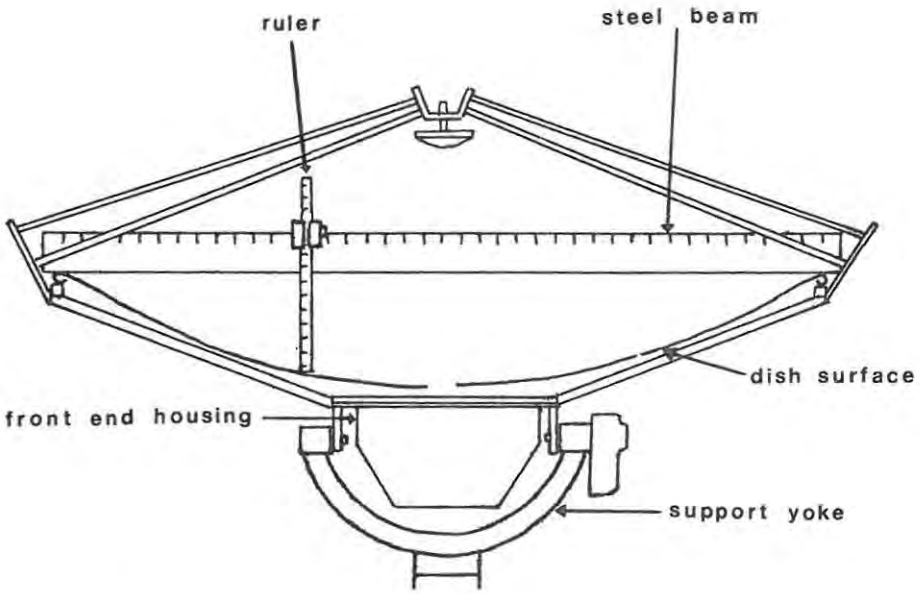

figure 2.2 THE TRIANGULATION MEASURING SYSTEM

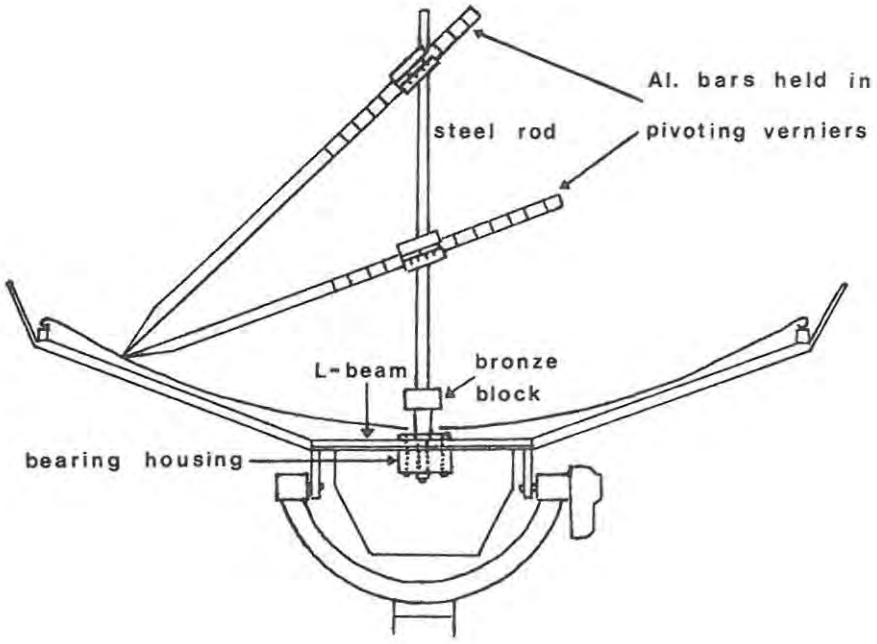

$$r^2 = 4\,fd \qquad 2.1$$

where r = radial distance to point on paraboloid

f = focal length

d = paraxial dish centre to surface point distance.

Using this formula the measurements gave a focal length of 0,704 $\pm$ 0,007 m. The large error was primarily due to the weight of the steel beam on the rim further deforming the already distorted dish.

2.3 The necessity for a Paraboloid surface survey

Initial operation of the telescope indicated that the aperture efficiency was low (section 5.8), largely due to distortion of the paraboloid. This was caused by the dish being clamped directly to the uneven steel octagon which supported it. However the surface could be adjusted by inserting shims under the dish rim at the sixteen points of contact with the octagon. For a minimal signal loss due to reflector errors the surface should be accurate to within λ /32, or 0,4 mm; measurements to $\pm$ 0,1 mm would clearly show such errors (Ruze, 1966).

Measurement of large antennas is normally carried out by theodolite and tape, or photographic survey, or laser- or radar-ranging, of surface targets (Mar and Liebowitz, 1969, pages 57, 136, 172, 195, 228; Findlay and Payne, 1974). Medium-sized antennas are surveyed by similar means; trolley mounted depth sensors (Payne et al., 1976) and templates have also been used (Zhuravlev et al., 1966). For small antennas, templates (Cowles and Parker, 1975) or large machine tools are normally used (Findlay, 1971).

Initially a triangulation system, supported independently of

the dish, was suggested by Baart (1975), this being a mechanical analogue of the twin pentaprism method of Greve (1975).

2.4 The Triangulation Instrument

The general form of the instrument is shown in figure 2.2. Two pivots clamped a fixed distance apart on the axially-mounted steel rod held aluminium bars whose tips were placed together at a point on the dish surface. The pivot separation was known, and the lengths of the bars to the pivot points was measured, using engraved scales in conjunction with verniers on their holders. This enabled the horizontal and vertical coordinates of the surface point to be calculated. A computer program was written for this purpose, which also calculated the best-fit paraboloid along each radius. To enable it to rotate the steel rod was mounted in a bronze block held in two bearings, the housing for which was clamped to the two L-beams which normally supported the front end.

Tests of the instrument on a flat surface indicated that the errors in each of the three measured lengths were $\pm$ 0,2 mm, and that these combined to give a final accuracy of $\pm$ 0,5 mm, which was unacceptable. An error analysis indicated that the accuracy could be significantly improved with a more compact and rigid system where fewer independent measurements were needed.

This led to the concept of a rotatable parabolic template, mounted in an improved form of the bearing housing, where only the perpendicular depth from the template edge to the dish surface needed to be measured. The absolute accuracy then depended largely on that of the parabolic template edge, the curvature of which was chosen from

the focal length obtained in previous measurements.

2.5 The Template Measuring System

A computer program was written to generate the full size parabola needed for the template. As computer-controlled milling facilities were not available, the Rhodes ICL-1901T computer was used to plot the parabola. This was repeated twice to check the plotting accuracy. The graph plotter's specified accuracy is $\pm$ 0,1 mm, and to retain this the computed parabola consisted of 10^4 points.

Using the graphs a 1,6 mm thick steel plate was cut and filed to the correct shape, as shown in figure 2.3. The template was held in a slotted brass rod by seven Allen screws, the template edge being located on the rod's centre-line by two grub-screws. The r.m.s. error on the parabolic edge was estimated to be within 0,2 mm, and it was correctly positioned laterally to within 0,1 mm, as measured on a large mill. The edge error only causes a constant systematic error in the mean reading at each radius (section 2.7).

Vertical slots were milled in the template at 50,0 mm intervals, 10,0 mm from the lower edge. Holes were cut in the outer half of the template to reduce its mass, bending moment about the centre-line, and wind resistance. The upper template edge was strengthened with a screwed-on steel L-beam. To counterbalance the template bending moment a 2,2 kg lead mass was mounted on a 0,5 m steel rod fitted horizontally on top of the brass rod.

A Baty D6 dial gauge with an accuracy of 0,01 mm was used for depth measurement. This was screwed onto an aluminium mounting (figure 2.4) and fitted with a small steel wheel, offset to lie with its

figure 2.3 THE TEMPLATE MEASURING SYSTEM

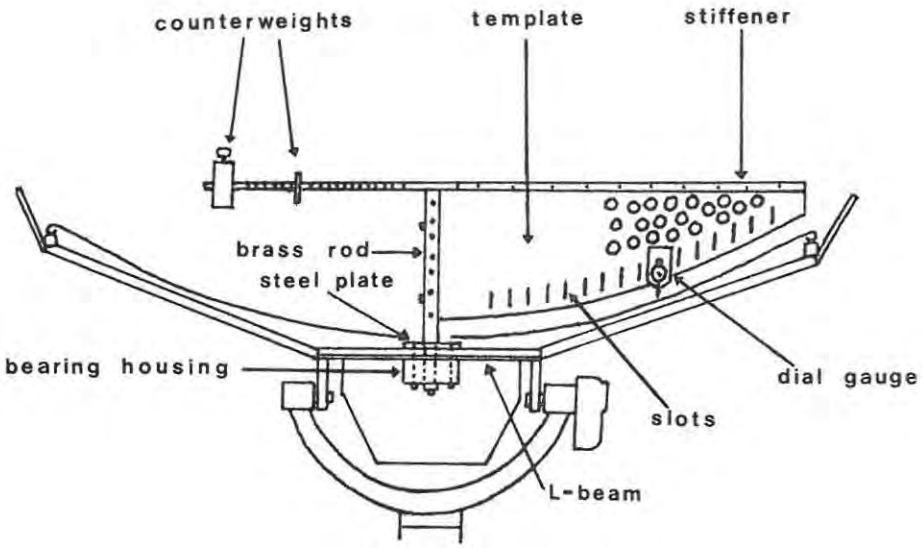

figure 2.4 THE DIAL GAUGE MOUNTING

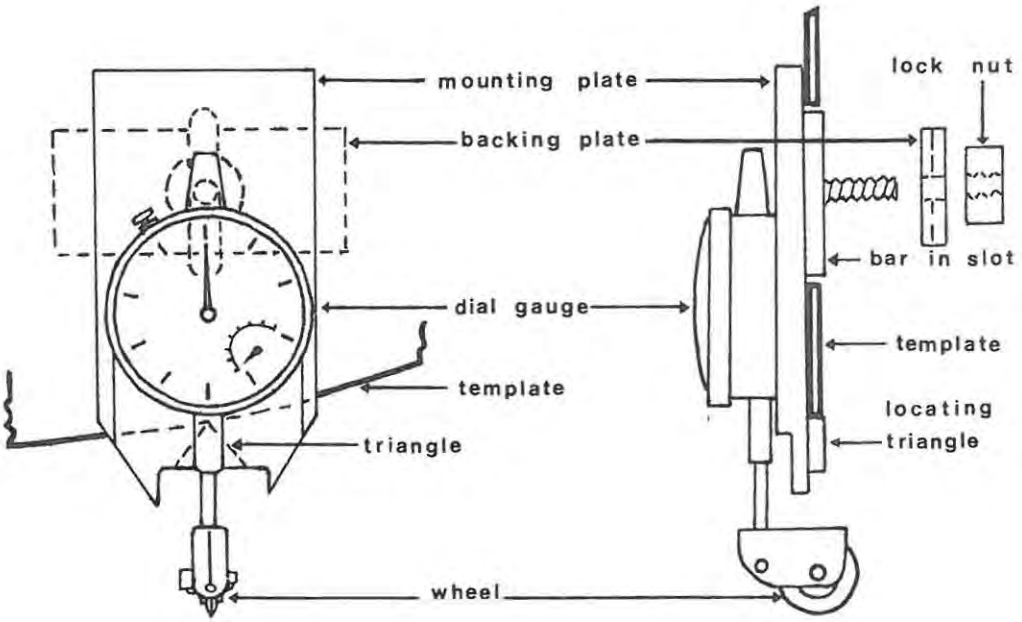

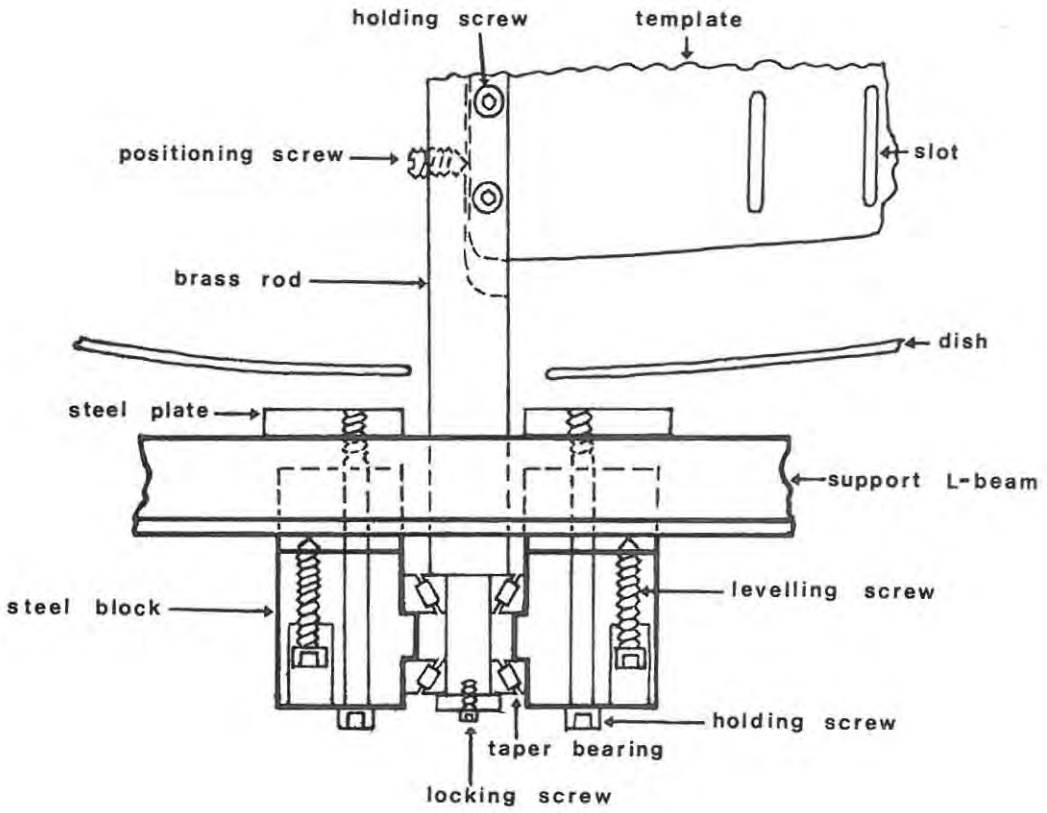

figure 2.5 BEARING HOUSING CROSS-SECTION

figure 2.6 UNDERSIDE OF HOUSING

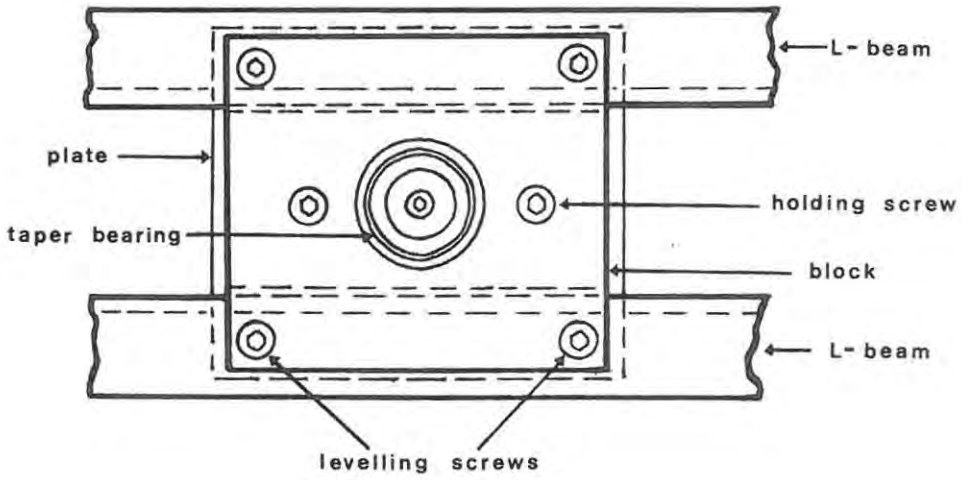

axis below the template centreline. The mounting carried a locating steel bar which was held in one of the template slots by a backing plate and lock nut. Accurate vertical positioning with respect to the template edge was by means of a steel triangle which butted against it. The force required to drive the dial gauge was approximately 1,5N. To counterbalance the net bending moment of the gauge and its mounting, a o,33 kg mass was added to the counterweight rod, this being placed at a radial distance half that of the gauge.

An electrical recording system was built using a potentiometer driven by gears engaged in a spring-loaded rack mounted above the gauge shaft extension, but this proved to load the system too heavily, necessitating a 10 N driving force, and was abandoned.

The final form of the bearing housing, using two taper bearings, is shown in figures 2.5 and 2.6. The housing was held under the L-beams by two screws and was levelled by four corner-mounted screws.

2.6 The Paraboloid Surveys

While the dial gauge mounting design was being finalised the dish was marked out at 45° intervals and the template installed. Repeated measurements were made of the horizontal and vertical template alignment with respect to the dish by means of vernier calipers, in order to centre and level the template accurately. After completion of the gauge mounting the dish was marked out at 5° intervals. Template positioning errors appeared as a sinusoidal variation in the gauge readings, with the maximum and minimum at opposite ends of a dish diameter. Surface errors were indicated by rapid gauge fluctuations on rotation of the template.

To improve the positioning accuracy initial corrections were made to the dish surface by altering the shims. After centralisation of the bearing mounting its support beams were clamped to those of the outer front end housing structure, in order to maximise structural rigidity. After the final reshimming the residual levelling error was estimated to be within $\pm$ 0,1 mm at the maximum radius of 0,90 m. A complete dish survey was then undertaken; to maintain approximately constant coverage per measuring point 516 readings were taken, as shown in table 2.1. Measurement time in each survey was about three hours.

The mean gauge reading and the r.m.s. error in the measurements were calculated at each radius, and the readings were plotted as deviations from each mean. The first contour map produced from the survey is depicted in figure 2.7. As was expected the surface irregularities were concentrated around the edge of the dish. The largest positive error was + 1,2 mm at 180°, and the largest negative error was -1,0 mm at 350°, where the dish surface was visibly damaged. Other large positive peaks occured at 90°, 200° and 270°, and another significant depression was located at 100°. From the mean readings at each radius the focal length of the paraboloid was calculated to be 0,697 $\pm$ 0,001 m. The r.m.s. surface error at each radius is shown as the dashed curve in figure 2.9, and the deviation of the mean reading

Table 2.1 First Survey Measurement Points

Radius limits (m)	Separation ($^{\circ}$)	Points per Radius
0,15 to 0,30	20	18
0,35 to 0,55	15	24
0,60 to 0,80	10	36
0,85 and 0,90	5	72

figure 2.7 CONTOUR MAP FROM FIRST PARABOLOID SURVEY
15 to 90 cm radius

contours at 0,2 mm intervals

—1— elevation

---1--- depression

figure 2.8 CONTOUR MAP FROM SECOND PARABOLOID SURVEY
15 to 90 cm radius

contours at 0,2 mm intervals

—1— elevation

– – –1– – depression

figure 2.9 RADIAL DEPENDENCE OF PARABOLOID'S RANDOM SURFACE ERRORS

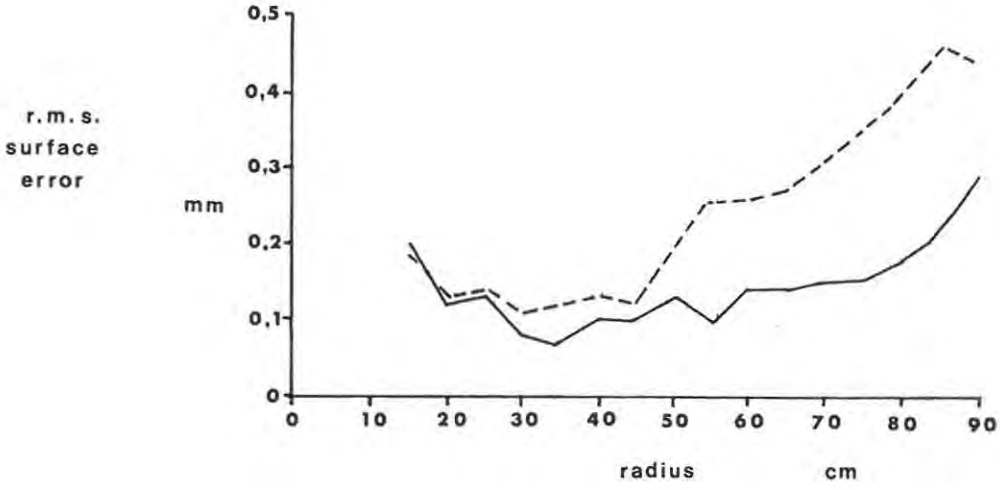

figure 2.10 DEVIATION OF MEAN SURFACE FROM BEST FIT PARABOLOID

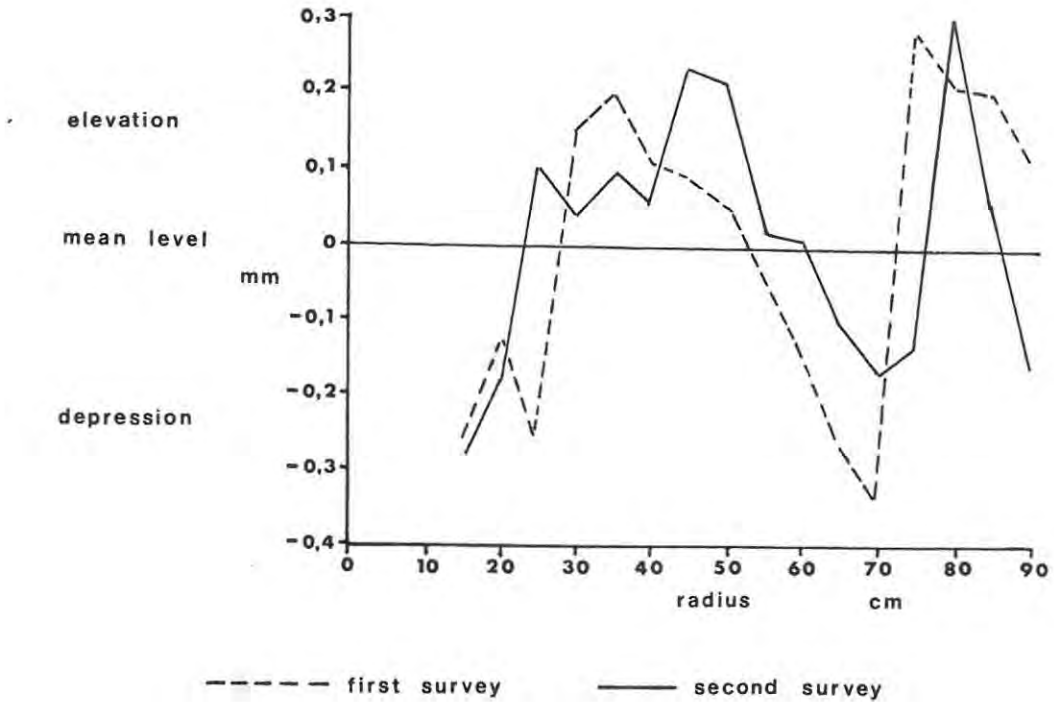

at each radius from the best-fit paraboloid is similarly depicted in figure 2.10.

Using the contour map reshimming was carried out at the points mentioned above, to increase the surface accuracy further. As the resolution from points at 5^{o} intervals was not significantly better than that for 10^{o} intervals, subsequent readings at 0,85 and 0,90 m were taken at the larger interval. The surface was resurveyed and the resulting contour map is illustrated in figure 2.8. In comparison with the previous map the large peaks at 90^{o}, 180^{o} and 200^{o} were reduced to 0,2 mm, 0,4 mm and 0,2 mm respectively and the depressions at 100^{o} and 350^{o} both decreased to - 0,4 mm.

It was noticeable that contours towards the dish centre, where reshimming had little effect, were almost identical, indicating good measurement accuracy and repeatability. The r.m.s. surface errors and the deviations of the mean levels from the best fit paraboloid are shown in figures 2.9 and 2.10. The improvement to the r.m.s. error is clear, while the deviations show little change as they are primarily due to template error. The revised focal length was 0,696 $\pm$ 0,001 m.

2.7 Accuracy of the Surveys

The systematic error in the mean level at each radius, due to template inaccuracy, was within $\pm$ 0,2 mm, and this formed the major contribution to the deviation of the mean surface from the best fit paraboloid (figure 2.10). The r.m.s. deviation from the best-fit curve was 0,20 mm in the first survey and 0,16 mm in the second; the peak values were $\pm$ 0,3 mm, at 70-80 cm radius.

The repeatability of readings indicated that the random error

in the measurements was within $\pm$ 0,03 mm near the dish centre and $\pm$ 0,07 mm near the rim. These errors are largely due to residual structural flexure, bearing wobble, and paint surface roughness. The first two factors increase linearly with the radial distance, and are the cause of the doubled error at the dish edge.

Temperature variations during the measurements are responsible for a further systematic error which affects the calculated focal length. A detailed discussion of the errors is given in appendix 2a. It was concluded that, to a first approximation, the lateral and vertical expansion of the dish and the lateral template expansion were self-compensating, leaving a residual error due to vertical expansion of the template. This amounted to a differential v of 0,0035 mm K^{-1} between the template centre and edge. Using equation 2.1, $r^2 = 4\,fd$, a small apparent change v in d at a radius of 0,9 m causes a change ϕ in the calculated focal length f of

$$\phi = 4\,vf^2/(r^2 - 4\,vf) \qquad 2.2$$
$$= 0{,}01 \text{ mm } K^{-1}.$$

This is only significant for temperature changes of 10K or more.

The template system used by Zhuravlev et al. (1966) on a 15 m paraboloid resulted in a surface accuracy of $\pm$ 0,75 mm, while that used by Cowles and Parker (1975) on a 2.8 m dish was capable of measuring to $\pm$ 0,3 mm, an accuracy similar to that achieved here.

2.8 Summary of Improvements to the Paraboloid.

The 0,9 m radius dish profiles, where the surface errors are largest, have been plotted in figure 2.11 for different stages in the

figure 2.11 PARABOLOID SURFACE CONTOURS AT 90 cm RADIUS

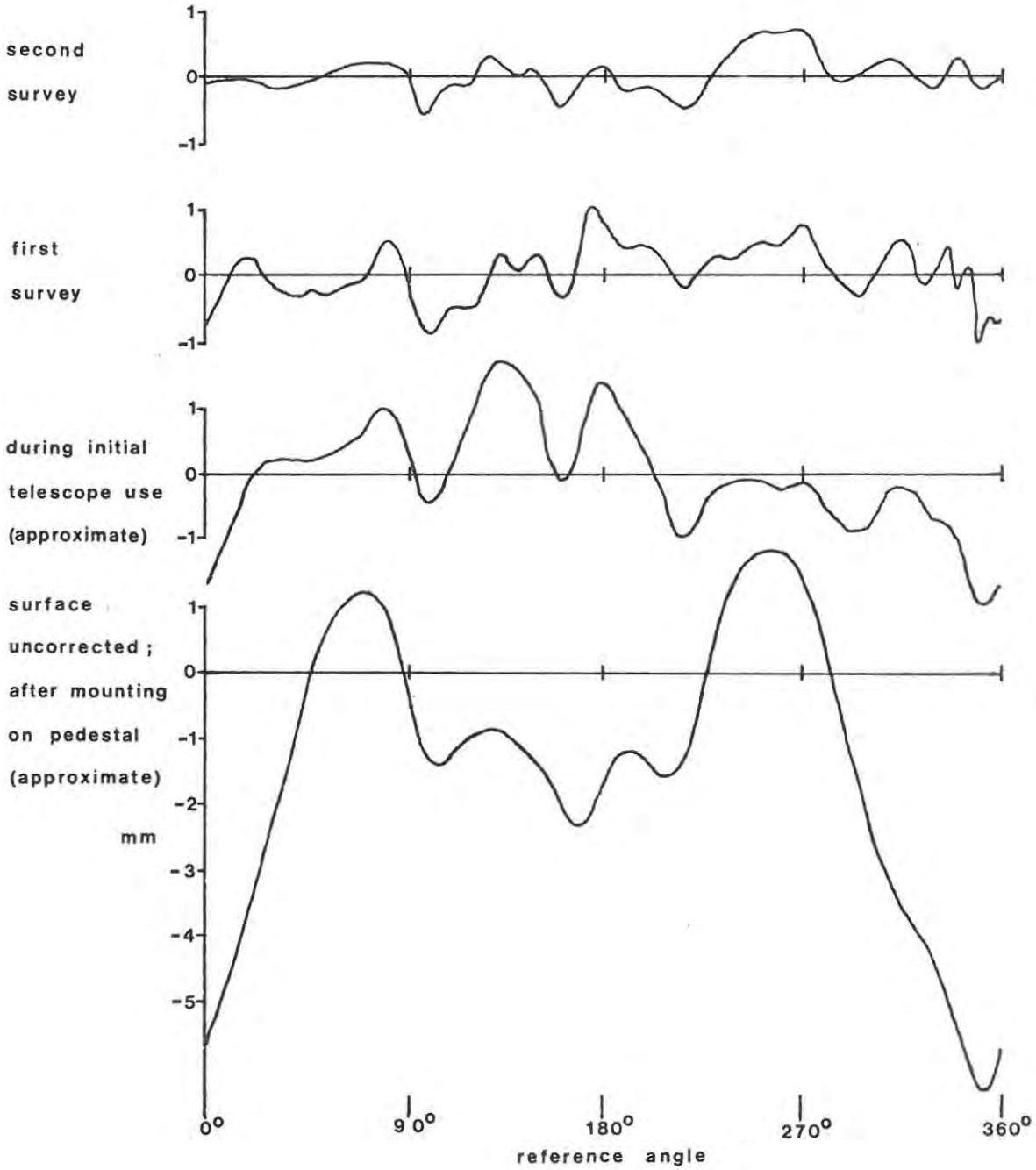

use of the telescope. The lowest profile shows the approximate contour immediately after the dish was mounted, when it was clamped directly to its support framework; the r.m.s. error was 2,2 mm. The second curve illustrates the approximate profile after some reshimming had been carried out, during initial telescope operations; the corresponding r.m.s. error was 0,85 mm. The third contour was obtained during the first survey, the r.m.s. error being 0,44 mm, and the last profile was measured in the second survey, after final reshimming, the r.m.s. error having been reduced to 0,28 mm. The correspondence of major features between each of the profiles is easily seen; through adjustment of the dish rim its r.m.s. error has been reduced by almost one magnitude. The effect of the surface errors on the antenna efficiency has been calculated in section 6.7.

2.9 The Subreflector

The design and manufacture of the hyperboloid subreflector for the Cassegrain antenna has been described by Nunn (1974) page 40; it has a diameter of 0,21 m and is located 0,53 m from the aperture plane of the primary horn. The simple paraboloid equivalent of this Cassegrain system would have a focal length of 4,35 m.

The first subreflector was distorted by inadvertent overheating; the manufacture of a second was supervised by this author and has been used for all telescopic observations. The hyperboloid surface was checked following the initial operation of the telescope. The subreflector was supported in a lathe and rotated slowly while a dial gauge, fitted with the wheel used for the dish measurements, was held in contact with its surface. The gauge was mounted in the tool-holding section of the lathe and was positioned by means of the control wheels on the holder.

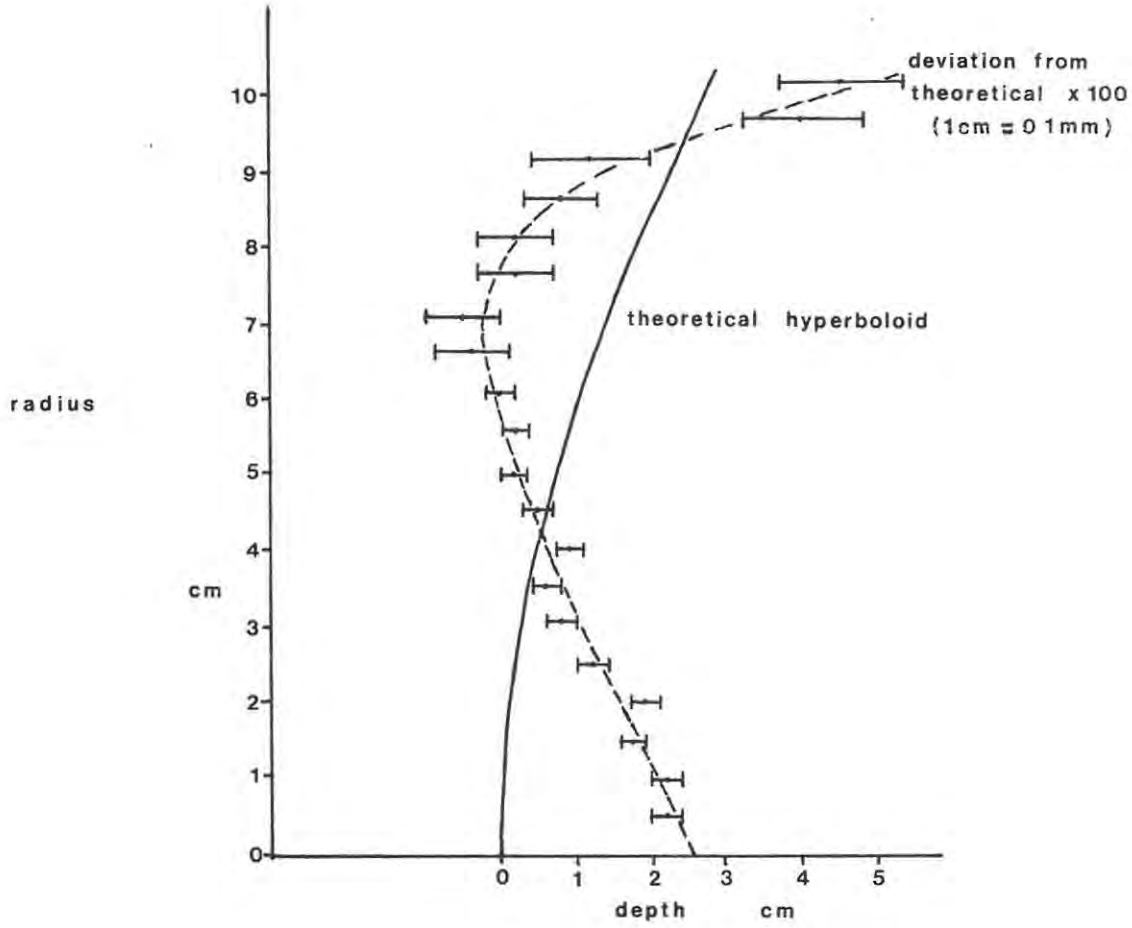

figure 2.12 DEVIATION OF SUBREFLECTOR FROM CALCULATED PROFILE

Figure 2.12 depicts the theoretical hyperboloid surface and the measured deviations from this surface, magnified one-hundred fold. The systematic departure from the calculated surface is apparent; the maximum deviation is 0,25 mm and the r.m.s. deviation 0,14 mm. The random surface error at each radius was typically $\pm$ 0,05 mm. The systematic measurement tolerances are shown as error bars in the figure.

2.10 Gravitational Deformation of the Antenna

The paraboloid surface was optimised with the antenna in the vertical position, and without the subreflector and its supports

installed. It is of interest to see whether the surface accuracy is maintained at all elevation angles and over a range of operating temperatures.

There are three principal gravitational effects, which are considered separately. These are:

(a) deflection of the paraboloid surface under its own weight at varying elevations;

(b) deformation of the large octagon supporting the paraboloid by the subreflector mounting;

(c) lateral movement of the subreflector at varying elevations.

The following analysis is not rigorous, but is intended to find the probable magnitude of these effects.

(a) The paraboloid is supported at its rim only; when the antenna is pointing at the zenith, the dish centre sags with respect to the rim by an amount δv. When the telescope is pointing at the horizon, the bending moment of the antenna about its support bearings causes it to flex downwards, by an amount δh. The general formula for the deflection Δ at any zenith angle z is then given by Hachenberg et al. (1973) as

$$\Delta = \delta v \ (1 - \sin z) + \delta h \cos z \qquad 2.3$$

By measurement of the separation of the dish centre and front end housing in the vertical and horizontal positions, δv was found to be 0,2 mm. This causes a change in focal length of 0,5 mm.

The value of δh cannot be measured directly, but its approxi-

mate magnitude can be calculated. It is shown in appendix 2b that deformation of the framework supporting the antenna (figure 2.13) is by bending of structural members and not by a change in their length. Further, all joints in the paraboloid support framework are welded, and so to a first approximation joint angles will not alter.

Following the method of Duncan (1949) pages 151-78, the deflection d of a beam of length L, fixed at one end, by a perpendicular force W on its free end is given by

$$d = WL^3/3EI \qquad 2.4$$

where E = Young's modulus

I = moment of inertia of the beam cross-section.

However if the beam end to which the force is applied is constrained to be parallel to the fixed end, the deflection is given by

$$d = W L^3/24\ EI \qquad 2.5$$

The deflections being considered here occur where a support beam from the small octagon is joined to a large octagon corner (labelled a to h in figure 2.13). The bending moment at each corner then occurs in three beams simultaneously. The relationship giving the deflection of each is intermediate between the two cases discussed above, as the joint can twist slightly to minimise the overall strain. Consequently the geometric mean of the two values has been used, or

$$d = WL^3/10\ EI \qquad 2.6$$

for each beam.

If the antenna is at an angle z to the zenith its weight W is not directly over its support bearings but has a component W cos z towards the bearings and W sin z normal to the antenna axis. This

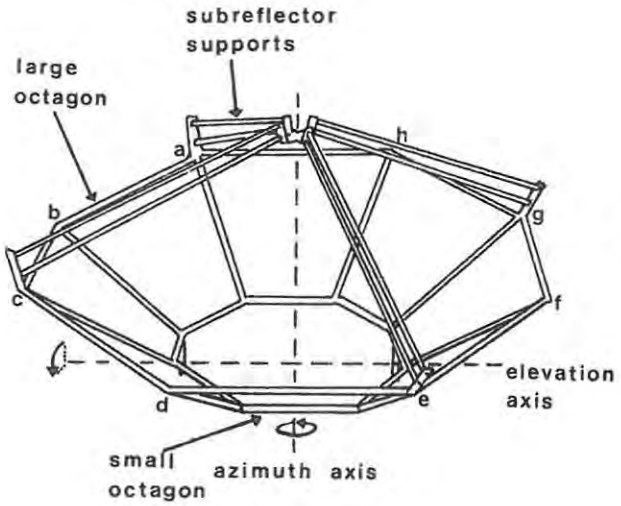

figure 2.13

THE ANTENNA SUPPORT STRUCTURE

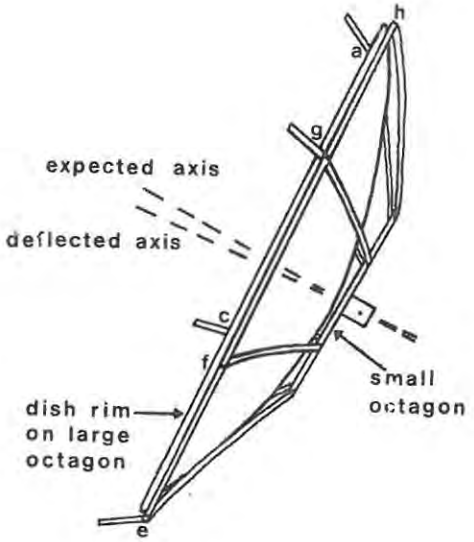

figure 2.14

EXAGGERATED DEFORMATION FROM DISH AND STRUCTURE WEIGHT

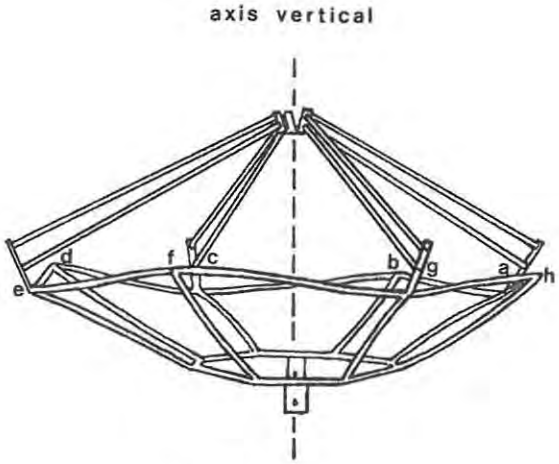

figure 2.15

SYMMETRICAL DEFORMATION FROM SUBREFLECTOR AND ITS SUPPORTS

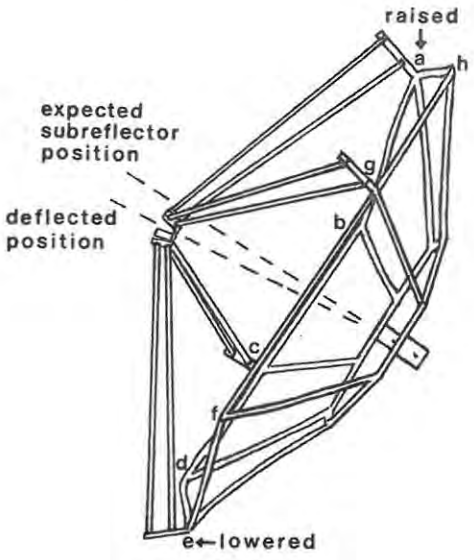

figure 2.16

ASYMMETRIC DEFORMATION AND SUBREFLECTOR TILT

bending moment causes the deflection of the antenna axis (figure 2.14), with little distortion of the large octagon or dish. When pointing at the horizon the weight is carried equally by each of the octagon supports; the deflection δh is approximately

$$\delta h = WL^3/80\ EI \qquad 2.7$$

$$= 0,7 \text{ mm}$$

This corresponds to an antenna axis tilt of 2 arcminutes.

The dish and structure weight causes an elevation dependent paraboloid surface deflection which affects the focal length and antenna pointing. The occurence of this is well known in large antennas (Mar and Liebowitz, 1969, pages 140-1, 190-7, 232-4).

(b) The deformation caused by the weight of the subreflector and its supports is also elevation dependent. As bending of the support frame is preferred to compression or extension, in any deformation the length of each octagon arm does not alter. If one of the corner joints a to h is depressed by an amount d, the two octagon arms joined there would tend to stretch (appendix 2c); to compensate for this the joints on either side are raised, so shortening the arms again. Consequently a calculated depression d at a joint is approximately transformed into a deflection of d/2, and a corresponding elevation of d/4 of its neighbouring joints.

When the antenna axis is vertical (figure 2.15) the weight of the subreflector and its supports acts equally on four of the octagon joints. At each joint the load is spread over three almost equally long bars, and its line of action is nearly normal to all three. For an isolated corner joint the deflection is given by one third of the value for a single beam, in equation 2.6, or

$$d = WL^3/30\ EI \qquad 2.8$$

$$= 0,2 \text{ mm}$$

where W = subreflector structure weight/4.

Using the result above, the support joints are actually depressed 0,1 mm, and the intermediate joints raised 0,1 mm.

If the antenna is pointing near the horizon approximately half the weight of the subreflector structure acts on joint a, and half, in tension, on joint e. Using equation 2.8 the deflections at a and e, as isolated joints, are + 0,4 mm (upwards) at a and -0,4 mm at e. In practice e is depressed 0,2 mm, and its neighbours raised 0,1 mm, while a is raised 0,2 mm, and its neighbours depressed 0,1 mm (figure 2.16).

Similar deformation induced by subreflector structures has been encountered in other antennas. It is noticeable in the relatively flexible Parkes 64 m telescope, but was virtually eliminated by the much more rigid structure of the N.A.S.A/J.P.L. 64 m Goldstone antenna (Mar and Liebowitz, 1969, pages 141 and 194).

(c) The double quadrupod subreflector structure itself is light and was designed to resist compressive forces and bending moments when pointing away from the zenith. When the antenna is nearly horizontal, as in figure 2.16, the subreflector is moved laterally less than 0,04 mm due to compression of the structure under its own weight, but a shift of 0,2 mm is introduced by the deformation of the large octagon as described above.

In summary, gravitational deformation of the telescope causes variations in the focal length and pointing direction; it introduces

an additional surface error around the dish rim, and causes a lateral motion of the subreflector.

2.11 Thermal Effects on the Antenna

The operating temperature of the antenna lies between $0^{\circ}C$ and $40^{\circ}C$. Thermal expansion causes a defocusing of the antenna, due to a change in shape of the paraboloid and to axial motion of the subreflector relative to the dish.

The antenna was focused when at a temperature of approximately $20^{\circ}C$. In the following calculations a 20 degree temperature rise is assumed in order to find the maximum defocusing effect. A temperature change t in an object of length L and coefficient of expansion α causes a change in length e given by

$$e = \alpha L t \qquad 2.9$$

The coefficients for steel and aluminium are given by Bolz and Tuve (1973) page 118, as $\alpha_{Fe} = 12 \times 10^{-6} K^{-1}$ and $\alpha_{Al} = 25 \times 10^{-6} K^{-1}$.

The paraboloid depth of 0,30 m will increase by Δd = 0,15 mm (figure 2.17), while its radius increases by Δr = 0,48 mm. As the dish edge is at 30° to the aperture plane, at a given radius near the rim the surface will appear to be lowered by $\Delta r \tan 30^{\circ}$, using the result in appendix 2a, or 0,28 mm. The differential change in depth between the dish centre and rim is then 0,15 - 0,28 mm or -0,13 mm, the paraboloid now being shallower. Using equation 2.2 this corresponds to an increase Δf in the focal length of 0,32 mm.

The axial position of the subreflector is governed by two

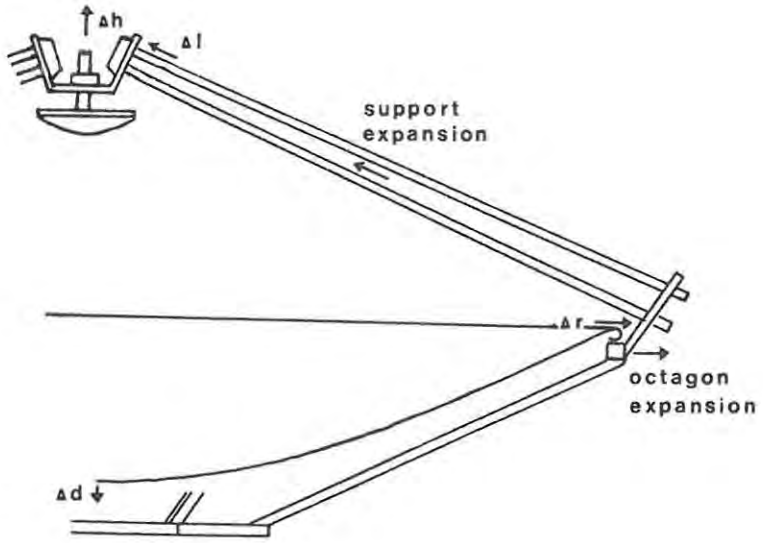

figure 2.17 THERMAL ANTENNA DEFORMATION

competing effects : the expansion of its support rods, which raises it, and the expansion of the large octagon, which lowers it.

The subreflector supports are at 25° to the octagon plane. A net expansion Δl of the supports increases the subreflector height by Δh, where

$$\Delta h = \Delta l \operatorname{cosec} 25^{\circ} \qquad 2.10$$

The net expansion Δl is the actual support expansion, minus the apparent contraction due to expansion of the large octagon.

$$\text{Support expansion} = l_s \alpha_{Al} t$$

$$\text{Apparent contraction} = r_{oct} \alpha_{Fe} t \sec 25^{\circ}$$

$$\therefore \quad \Delta h = t \operatorname{cosec} 25^{\circ} (l_s \alpha_{Al} - r_{oct} \alpha_{Fe} \sec 25^{\circ}) \qquad 2.11$$

$$= 0{,}56 \text{ mm.}$$

The effect of this motion is partly offset by the increased focal length of the paraboloid due to its thermal expansion. The net

apparent movement Δz of the subreflector relative to the new focal point is

$$\Delta z = \Delta h + \Delta d + \Delta f \qquad 2.1$$
$$= 0,4 \text{ mm}$$

As this is well within the range of the subreflector focusing error (section 6.7), there should be no appreciable effect on antenna performance when observing extended sources.

Thermal affects have been noted in large antennas (Mar and Liebowitz, 1969, pages 172, 190, 238), the main result being defocusing as considered above. As the Rhodes antenna consists of a single piece of spun aluminium, it should not suffer from the differential heating effects also seen in large antennas where the surface is made of many separate panels.

CHAPTER THREE

THE FRONT END

3.1 Introduction

3.2 General description of the front end

3.3 Continuum studies

3.4 Spectral line studies

3.5 The initial front end layout

3.6 Early operation of the front end

3.7 Microwave component testing

3.8 Mixer temperature measurements using the noise tube

3.9 Mixer temperature measurements using liquid air

3.10 Measurement of the mixer power output

3.11 The final front end layout

CHAPTER THREE

THE FRONT END

3.1 Introduction

In the 'front end' microwave section the 22 GHz radiation from the antenna is converted to an intermediate frequency (i.f.) signal, which is amplified and carried by cable to the receivers.

For continuum observations beam switching is used, which is obtained by means of an on-source primary horn feed and an off-source reference horn. The mixer input is switched between the two beams at 95 Hz. An alternative method of beam switching is to nod the sub-reflector (Slobin et al., 1970), but this has the disadvantage that it is slower than the electronic method, the optimum switch frequency being 100 Hz or more (Kraus, 1966, page 249). The basic front end design is similar to that in use at Hat Creek (Wrixon et al., 1971), which, however, has an additional microwave switch to allow for dual beam use or switching against a matched load.

For spectral line observations only the primary beam is used, the signal being detected by the standard method of frequency switching onto, and off, the spectral line.

3.2 General Description of the Front End

The first front end layout is shown in figure 3.1. For clarity, waveguide supports have been omitted. The microwave components were mounted on one side of an aluminium plate, the reverse side carrying the power supplies and i.f. amplifiers.

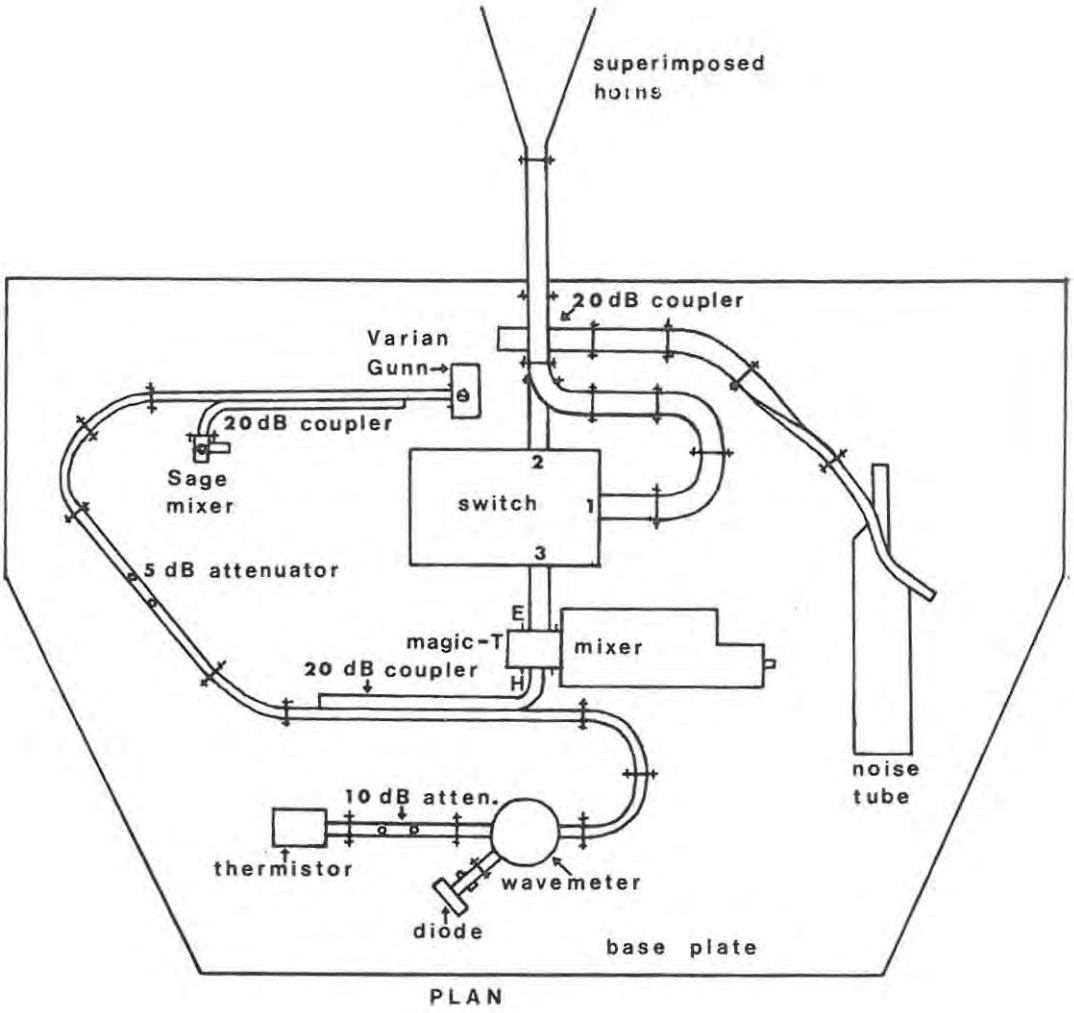

figure 3.1 INITIAL FRONT END

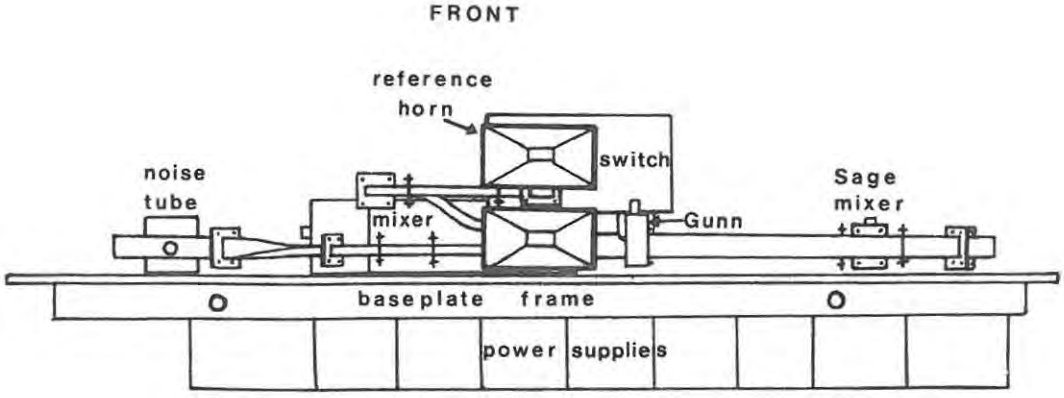

The two pyramidal horns were superimposed, giving a beam separation of $0,6^{o}$, or 1,3 beamwidths, in the vertical plane. The waveguide from the horns passed through the central hole in the paraboloid into the waterproofed front end housing between the antenna support arms. Local oscillator (l.o.) power was provided by a Gunn diode, mechanically or electromechanically tuned. The latter is coarse tuned by adjusting the resonant cavity size; fine tuning is by varying the D.C. voltage applied to the varactor diode, which alters the capacitance of the resonant circuit (Joshi and Cornick, 1973). For line work it is locked to a particular frequency by a Sage coherent microwave oscillator synchroniser, or 'lock-box', the mixer for which was mounted on an adjacent coupler. A wavemeter and diode detector were used to find the local oscillator frequency, while a thermistor could be mounted in place of the normal terminating matched load, for measurement of the l.o. power output. Calibration of the system was carried out with an Argon gas discharge tube, or 'noise tube', which provides white noise equivalent to a known temperature, coupled to the primary feed.

The mixer receives microwave signals via a magic-T junction. The signal from the feed connected via the switch enters the E-plane arm, and that from the l.o. the H-plane arm. Two Schottky diodes act as detectors, in a push-pull arrangement, in which the l.o. noise is out of phase and gives no output, while the signal from the antenna is in phase and is detected (Collin, 1970, page 286). The output is the difference frequency between the l.o. and input signals, and is amplified by an i.f. amplifier with a 10-110 MHz pass-band incorporated into the mixer mount. The i.f. signal is passed to a wideband amplifier for the continuum receiver, or a narrowband amplifier for the spectral

line receiver. Only the former system has been used operationally.

3.3 Continuum Studies

The mixer input is switched between the primary (figure 3.2a) and reference (figure 3.2c) beams, at a frequency of 95 Hz. The on-source primary beam sees both the sky and source radiation, while the off-source beam only sees sky radiation. Both sidebands on either side of the local oscillator frequency (figures 3.2b and d) contribute to the observed signal (figure 3.2e), and the double-sideband noise temperature of the mixer is applicable in determining the receiver sensitivity (section 4.4). The signals are detected synchronously in the continuum receiver (section 4.1), so that only the difference between the two, due to the source radiation, is integrated.

3.4 Spectral Line Studies

Only the primary beam is used for spectral line observations (figure 3.3a). The 95 Hz signal is now used to switch the local oscillator frequency so that the spectrum is observed every half cycle. The signal is normally buried in the noise and is only detectable on integration. The noise, being random, has equal positive and negative fluctuations which cancel out when integrated over a period of time, leaving only the signal, which is positive and in phase with the switch, for synchronous detection in the receiver channels.

The Gunn diode local oscillator is locked 30 MHz, the centre frequency of the spectral line receiver channels (section 4.2), below the expected maser frequency (figure 3.3b). This is doppler shifted away from 22,235 GHz due to the relative source-Earth motion. The Sage lock-box compares the l.o. frequency with that of an harmonic of an

a input from on-source beam

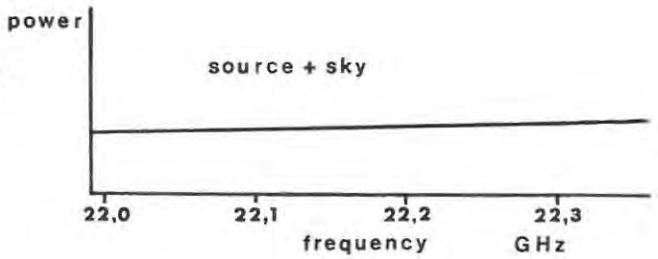

b on-source i.f. output bands' positions in the signal band

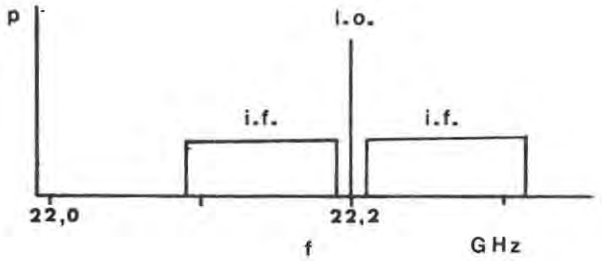

c off-source input

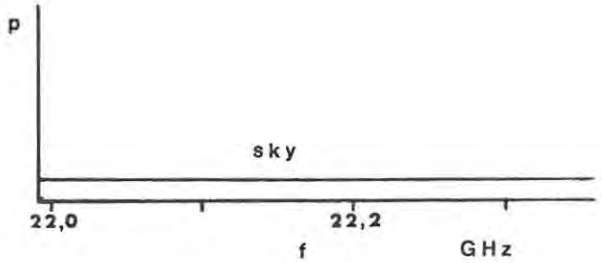

d off-source i.f. bands

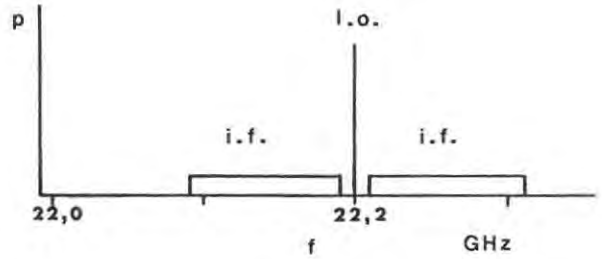

e signals detected in continuum receiver

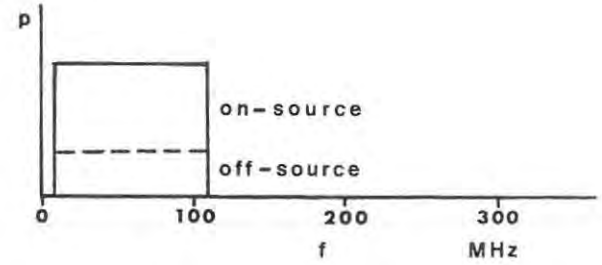

figure 3.2 IDEALIZED CONTINUUM RECEIVER OPERATION

a input signal

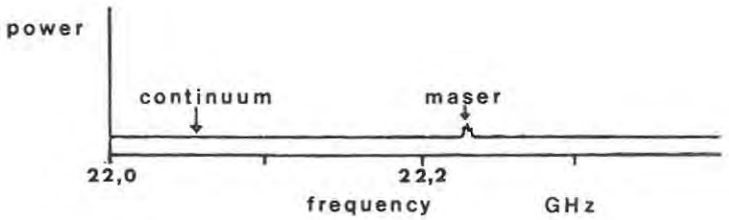

b i.f. bands , l.o. locked

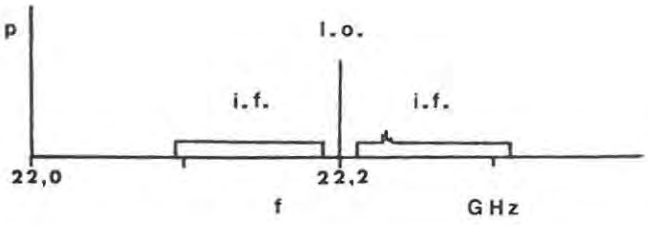

c i.f. bands , l.o. out of lock

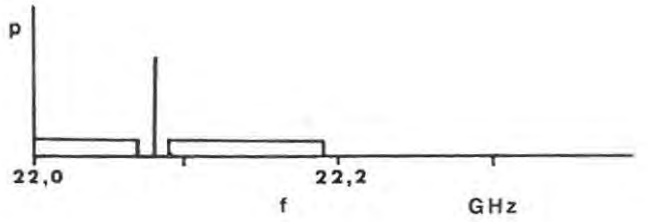

d i.f. amplifier output

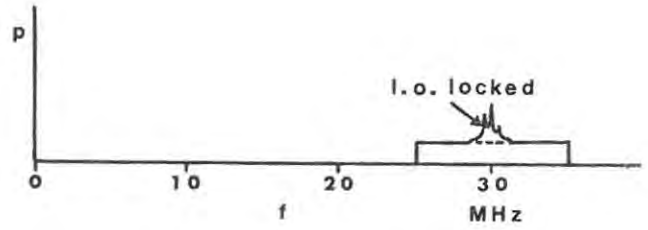

e alternate signals in centre ten channels

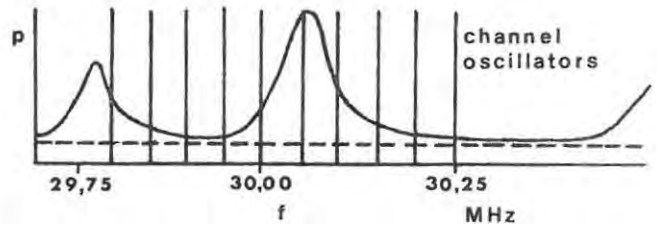

f histogram from the centre channels

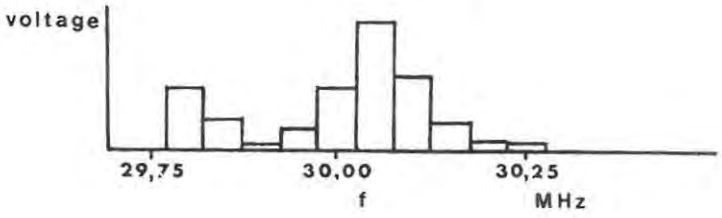

figure 3.3 IDEALIZED SPECTRAL LINE RECEIVER OPERATION

internal crystal oscillator. The comparator supplies a correction voltage proportional to the phase difference between the two signals to the varactor diode in the Gunn diode mount. In order that no spectral signal is seen from the source during the second half of the switch cycle, a voltage is applied to the varactor diode to alter the l.o. frequency so that the spectrum no longer falls within the passband of the receiver channels (figure 3.3c). The Gunn is not locked in this state. The signal passes to a narrowband amplifier (figure 3.3d), and is distributed to the receiver channels.

3.5 The Initial Front End Layout

The criteria which determined the components to be used in the actual layout, while incorporating the operating principles described above, are listed below.

(a) The space available for the front end was 0,50 x 0,33 x 0,15 m, the microwave components being mounted on one side of the baseplate.

(b) Specific signal levels were required for the mixer, lock-box mixer, thermistor, and from the noise tube. The component specifications are listed in appendix 3a. The mixer required 2 mW l.o. power; however early tests indicated that 0,25 mW was optimum (Mutch, 1975, page 22). To obtain this with the L or S Varian Gunn diodes a 20 dB coupler and 5 dB fixed attenuator were used. The lock-box mixer required between 0 and -30 dBm l.o. power, obtained with a 20 dB coupler; locking performance was marginal with a 30 dB coupler. The thermistor's maximum permitted continuous power level was 10 mW, the input l.o. power being kept below this level with a 10 dB attenuator. The noise tube has a specified excess noise ratio (ENR) of 16,4 $\pm$ 0,2 dB

(Olson, 1971). If T_G is the effective noise temperature of the tube, and the standard temperature T_o = 290 K, then from Kraus (1966) page 286

$$ENR = (T_G - T_o) / T_o \qquad 3.1$$

$$\text{or } T_G = 12950 \pm 600 \text{ K.}$$

As observed temperatures are normally less than 100 K, excepting that of the sun, a 20 dB coupler was used to feed the calibration signal into the waveguide between the primary horn and switch.

(c) The dual-beam feed used 20 dB gain pyramidal horns, which were the highest gain horns available. For weather protection their apertures were covered with sheet mylar, which causes very little microwave attenuation (< 0,03 dB).

(d) Attenuation of the signal between the horns and mixer had to be minimised to maintain the receiver sensitivity (section 4.4). For a given waveguide cross-section, propagation mode, and frequency, the attenuation is due primarily to the finite conductivity of the wall material, and is affected by the presence of standing waves, surface roughness, and any semiconducting film on the metal walls (Harvey, 1963 , pages 15 and 46). The waveguide used was WG 20 (or WR 42); preformed components were made of silver-plated copper, and those made in the workshop were of brass or copper. Assuming the surface roughness to be small in comparison with the skin depth (of the order of 10^{-6} m), the attenuation at 22 GHz is:brass, 0,58 dB m^{-1}; silver, 0,37 dB m^{-1}; copper, 0,36 dB m^{-1} (Skolnik, 1970, page 8-10). Oxides on copper waveguide are non-conductive and have little effect on attenuation. However a layer of silver sulphides is formed if silver-plated waveguide is exposed to a corrosive atmosphere, which can increase attenuation by up to 160 per cent (Harvey, 1963, pages 47-8).

The waveguide used in the microwave switch has a slightly larger internal cross-section, 11,4 x 4,8 mm, than that of the standard waveguide, for which it is 10,7 x 4,3 mm. The VSWR caused by a small waveguide discontinuity is given by $a_1 b_2 / a_2 b_1$, where a and b are the internal waveguide dimensions (Harvey, 1963, page 63). This corresponds to a VSWR of 1,07 at the switch, which is slightly less than the measured value (table 3.2). Attenuation also occurs at waveguide joints, especially from a twisting of components. Consequently both the length of waveguide used, and the number of components, has to be minimised.

In order to complete the layout some non-standard waveguide sections were needed. Straight sections were produced by silver-soldering flanges, either commercial examples or workshop made substitutes, to the appropriate length of waveguide. A number of simple and reflex E-plane bends were also produced. Several manufacturing methods were tried before a successful one was adopted, which is described in appendix 3b.

3.6 Early Operation of the Front End

The front end was initially bench tested by detecting the noise tube calibrator or a heavily attenuated Gunn diode, simulating continuum and spectral line sources respectively. Two modifications were made to the front end during its early use on the antenna, as a result of operating experience:

(a) A variable, frequency- and temperature-dependent difference in output from the two beams was found, when both were off-source, when using the Varian S Gunn diode as the local oscillator. This was attributed to l.o. signal, with its associated f.m. noise, passing

through the mixer, which has > 18 dB isolation between ports, and being reflected from the switch and waveguide discontinuities. The resulting frequency-dependent standing waves affect the mixer operation (Benson, 1969, page 478). The problem was largely solved by the use of the Mid-century Microwavegear (M.M.) Gunn diode, which presumably generates less f.m. noise. As the l.o. frequency is temperature dependent, front end thermal control was established by means of ten heater elements mounted between asbestos sheets and aluminium plates, with a thermistor feedback control.

(b) A precision variable attenuator was installed between the noise tube and coupler, so that the magnitude of the calibration signal could be varied as required. The wavemeter feedline was also slightly revised.

Following the rebuilding of the improved layout, the remaining problem was that complete cancellation of the sky signal could not be achieved as the two beams were at different elevations. The front end was removed in June 1975, to enable the antenna to be moved to a new site for testing of its drive system. The opportunity was taken to carry out tests on the microwave components, and in particular to re-measure the mixer temperature. Finally the front end was rebuilt to an improved design.

3.7 Microwave Component Testing

The insertion loss, isolation, and VSWR of a number of components was measured. The Mid-century Microwavegear Gunn diode and VSWR meter were used for these measurements. Calibration of the 1N26 diode detector in the latter indicated that it was operating as a square law device, and was used in conjunction with a galvanometer. A summary of the measurements is given in table 3.1. The two precision

Table 3.1 Microwave Component Performance

Component	Insertion Loss (dB)	Isolation (dB)	VSWR
Switch	0,25	22,0	1,07-1,12
Circulator (port 1-2)	0,27	24,0	1,10
Circulator (port 1-3)	0,30	30,0	1,08
10 dB horn			1,16
15 dB horn			1,10
20 dB horn			1,05
Matched load 25081			1,01
Matched load 1948			1,03

variable attenuators were also recalibrated. A newly-acquired switchable circulator was also tested to find its maximum switch rate: the 90% rise time for a square wave signal was 9 ms , and the 90% fall time 6 ms , precluding its use at 95 Hz.

3.8 Mixer Temperature Measurements using the Noise Tube.

The double channel mixer noise temperature had been measured prior to front end assembly, using the noise tube fed via a variable attenuator. Mutch (1975) pages 18-23 obtained a figure of 600 ± 100 K using the Y-factor and 3 dB methods. There appear to have been unforseen errors in these measurements:

(a) the insertion loss of the attenuators was not allowed for;

(b) too high a signal level from the noise tube was used, leading to mixer non-linearity;

(c) there was some confusion in the noise tube ENR, 16,07 dB being

used in place of 16,4 dB.

All mixer temperature measurements made by this author used the Y-factor method, the theory of which is given below. The microwave switch was used to inject noise corresponding to two different known temperatures into the mixer. The mixer i.f. output was amplified and the power levels corresponding to the two input temperatures measured. A variable attenuator was used to set the l.o. power, in order to find the optimum level, and the frequency was measured using the wavemeter.

Kraus (1966), page 260, relates the mixer noise temperature T_R to its noise figure F by

$$T_R = (F-1)\ T_o \qquad 3.2$$

where T_o = ambient temperature = 290 K.

If one of the noise sources is a matched load at T_o, and is switched through to the mixer, the output power indication is

$$I_1 \propto T_o + T_R \qquad 3.3$$

Attenuation in the waveguide to the mixer does not affect the temperature seen by the mixer as all the waveguide is at T_o. If the second noise source is at a known temperature T_G, the mixer will actually see a temperature T_c, due to the attenuation L of the signal, and the output power indication is

$$I_2 \propto T_c + T_R \qquad 3.4$$

The linear Y-factor, or ratio of the two power outputs, is given by Kraus (1966)page 287 as

$$Y = I_2 / I_1 = (T_c + T_R) / (T_o + T_R) \qquad 3.5$$

A modified form of the initial front end was used for the measurements. A matched load was mounted on port 2 of the switch, to

Table 3.2 Mixer Performance as a function of Input Signal

Input Temp. T_c (K)	Minimum Mixer Temp. T_R (K)
1250	635
900	615
680	585
540	575
490	570
450	590

provide T_o, and port 1 was connected to a 10 dB directional coupler, terminated in a matched load. The noise tube was connected to the coupled arm via a precision variable attenuator. The Varian S Gunn was used as the l.o., at 22,25 GHz. The temperature T_c seen by the mixer was the sum of the attenuated noise tube temperature, T_G / L, and T_o from the matched load terminating the coupler.

Hence $T_c = T_G / L + T_o$ 3.6

rearranging eqn. 3.5 $T_R = (T_c - Y T_o) / (Y - 1)$ 3.7

substituting in eqn. 3.6 $T_R = T_G / L (Y - 1) - T_o$ 3.8

An HP 8558B spectrum analyzer, initially used to measure the change in mixer output, was not sufficiently accurate, and was replaced by an HP8471A crystal detector and a Philips microvoltmeter, but this combination suffered from excessive drift. Finally an HP thermistor and HP432A power meter were used. Two Alan Industries attenuators, calibrated at 1 dB and 0,1 dB intervals, were inserted before the thermistor, as a check on the latter's linearity. With this system power levels were estimated to $\pm$ 0,02 dB.

Measurements were made with T_c between 1250 K and 450 K, and l.o. power from 0,27 to 2,22 mW.

The values of T_R obtained at T_c = 1250 K and 900 K were significantly higher than those at lower signal levels, indicating mixer non-linearity for $T_c > T_R$ (Kraus , 1966, page 287). The minimum measured mixer temperature at each input temperature is given in table 3.2. The values of T_R obtained for T_c less than 900 K have been averaged and plotted against the l.o. power in figure 3.4. The optimum l.o. power is between0,5 and 0,9 mW. Due to the uncertainty in the noise tube ENR, the systematic error in the measurements is up to 30 K, while the random error is $\pm$ 10 K, and that in the l.o. power, $\pm$ 5%. The mean mixer temperature from these measurements is 590 K $\pm$ 30 K, at 22,25 GHz, which corresponds to a double sideband noise figure F of 4,8 $\pm$ 0,2 dB.

3.9 Determination of the Mixer Temperature using Liquid Air

The conventional hot/cold load method was used to provide confirmation of the mixer temperature independently of the noise tube measurements. This differed from the Y-factor method only in replacing the noise tube with a cold load at a known temperature. The design of a black-body for use at microwave frequencies has been discussed by Carli (1974). Similar principles are used in the design of anechoic chambers (Emerson, 1973), which employ arrays of pyramidal carbon-impregnated material.

Tests indicated that charcoal was a good microwave absorber, so a crude black-body was constructed by partly filling a large vacuum flask containing small charcoal chips with liquid air. An aluminium plate with a small aperture for the waveguide formed the lid. This apparatus, used as the cold load, is shown in figure 3.5. To avoid specular reflection of room temperature radiation from the waveguide back up the horn, it was placed at a 45° angle and partly immersed in

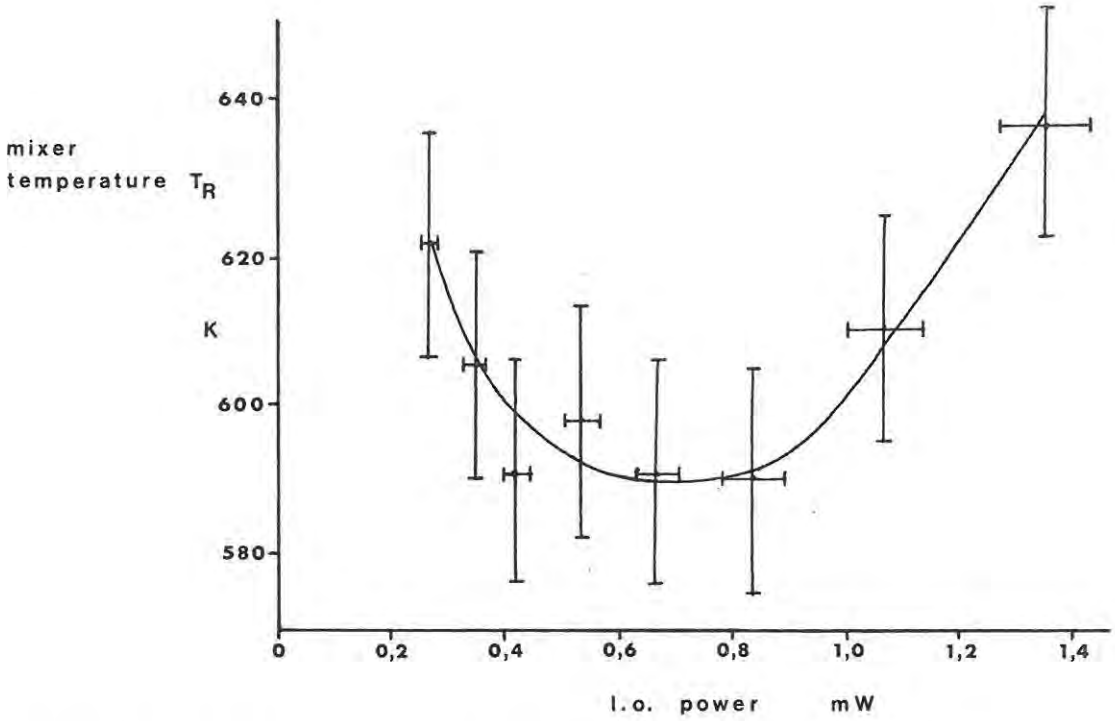

figure 3.4 DEPENDENCE OF MIXER SENSITIVITY ON L.O. POWER

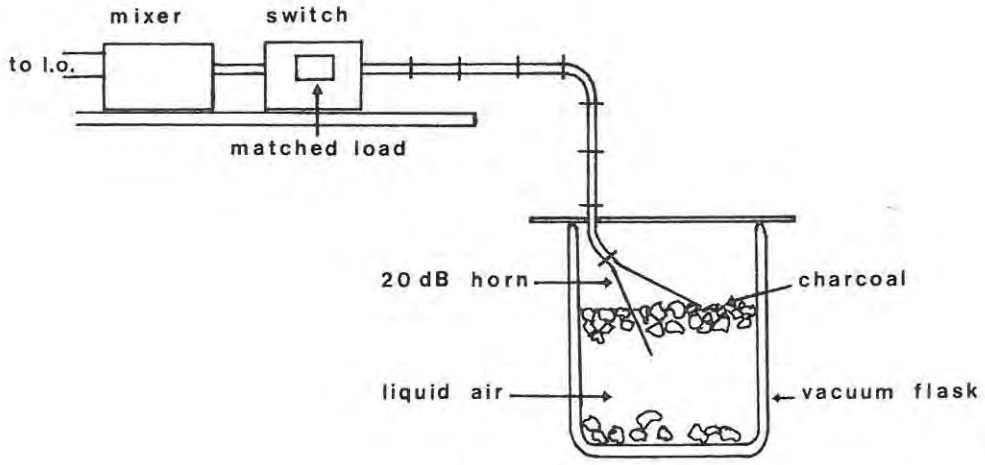

figure 3.5 HOT/COLD LOAD APPARATUS FOR T_R DETERMINATION

Molar % Oxygen	Boiling Point (K)
10	78,2
20	78,9
20,9	79,0
30	79,7
40	80,6
50	81,7

Table 3.3 Boiling point of liquid air (Wasburn, 1926 , page 103)

the liquid air, with charcoal chips covering the liquid surface.

The temperature T_c seen by the mixer is now the sum of the attenuated temperature of the liquid air, T_{la}/L, and the noise contribution of the waveguide and switch, $T_o(1 - 1/L)$.

Hence $T_c = (T_{la} - T_o)/L + T_o$ 3.9

which, with equation 3.7 gives (Kraus, 1966, page 286)

$$T_R = (T_{la} - T_o)/L(Y - 1) - T_o \qquad 3.10$$

The temperature of liquid air does not remain constant, but rises slowly as nitrogen boils off. The boiling point as a function of molar percentage of oxygen is given in table 3.3, 20,9% corresponding to the atmospheric oxygen content. A mean temperature of 80 ± 1 K was used in the calculations. The matched load temperature was monitored with a mercury thermometer. The VSWR of the horn immersed in the liquid air was measured as 1,06, which, compared to the free space value of 1,05, indicated little mismatch, due to the absorption of radiation from the waveguide by the charcoal. The measurements were made over a range of frequencies, using both the Varian S and Mid-century Microwavegear Gunns, and also with the circulator installed between the switch and mixer, as in the final front end layout (section 3.11).

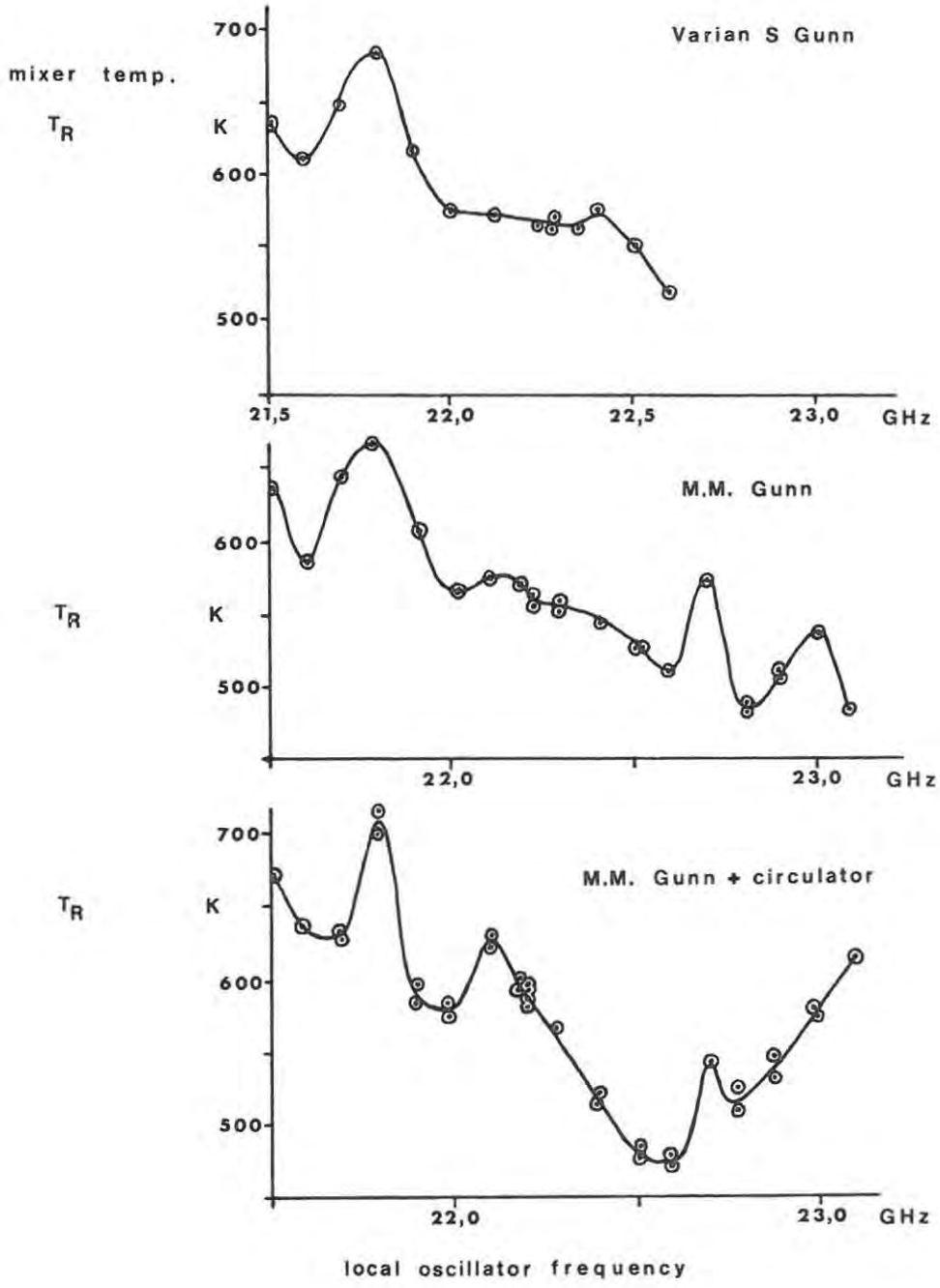

figure 3.6 FREQUENCY DEPENDENCE OF MIXER TEMPERATURE

The results of the measurements on the three test layouts are shown in figure 3.6. In each case the lowest noise figure occurs near 22,5 GHz, giving the optimum operating point for continuum observations. The variation between the curves is due to the different l.o. characteristics and standing waves in the system. The upper frequency limit of the Varian S Gunn is 22,6 GHz. The accuracy of the results may be summarised:

$T_{la} = 80 \pm 1$ K $\qquad\qquad T_o = 290 \pm 2$ K

$L = 0{,}52 \pm 0{,}02$ dB without circulator

$L = 0{,}72 \pm 0{,}02$ dB with circulator

measured $Y = 0{,}8 \pm 0{,}02$ dB

The resulting error in T_R for each measurement is $\pm$ 20 k. For spectral line work at 22,2 GHz, T_R from the three layouts is 570 K, 567 K and 580 K, the mean being 572 ± 7K, while at 22,5 GHz the corresponding figures are 460 K, 530 K and 550 K. In practice the value obtained on the final front end was approximately 550 K at this frequency, at an operating temperature of 300 K.

The noise temperature calculated using the hot/cold load is in agreement with that found by the Y-factor method with the noise tube, within the limits of error.

3.10 Measurements of the Mixer Power Output

Ideally, the i.f. output power of the mixer should be independent of the l.o. frequency when the mixer's signal port is terminated with a matched load at a constant temperature. This is of particular importance when frequency switching, as any change in the output might be interpreted as a signal. Two factors prevent this ideal state from being achieved:

(a) the mixer temperature, and hence its sensitivity, is frequency dependent;

(b) standing waves in the system, which affect the mixer operation, are frequency dependent.

For continuum observations, if the front end is not accurately temperature controlled the mixer should not be used where its sensitivity varies rapidly with frequency, as is seen at 21,8 GHz and above 22,6 GHz in figure 3.6 , and operation should be kept at a point where output variations are small.

To measure the mixer output variation with a minimal VSWR, a matched load with a VSWR of 1,01 was mounted directly on the mixer input. The resulting dependence is shown in figure 3.7a ; anomalous behaviour is visible at 22,15 GHz and above 22,6 GHz, which may be due to standing waves in the mixer's magic-T. A 20 dB gain horn mounted on the mixer produced similar results. Further measurements were carried out on test versions of the revised front end, incorporating the circulator and with the horns in the same horizontal plane. The mixer output for one such layout (figure 3.7b), which was subsequently rejected, shows a pronounced ripple above 22,3 GHz. The results obtained from the final redesigned front end are shown in figure 3.7c. Reliable operation should be possible between 22,2 and 22,6 GHz.

The standard cure for standing wave problems is the inclusion of an isolator between the mixer and switch. However these have a high insertion loss, of the order of 1dB, which would significantly degrade the receiver sensitivity. The use of the circulator, which has a lower insertion loss, 0,27 dB, has proved adequate.

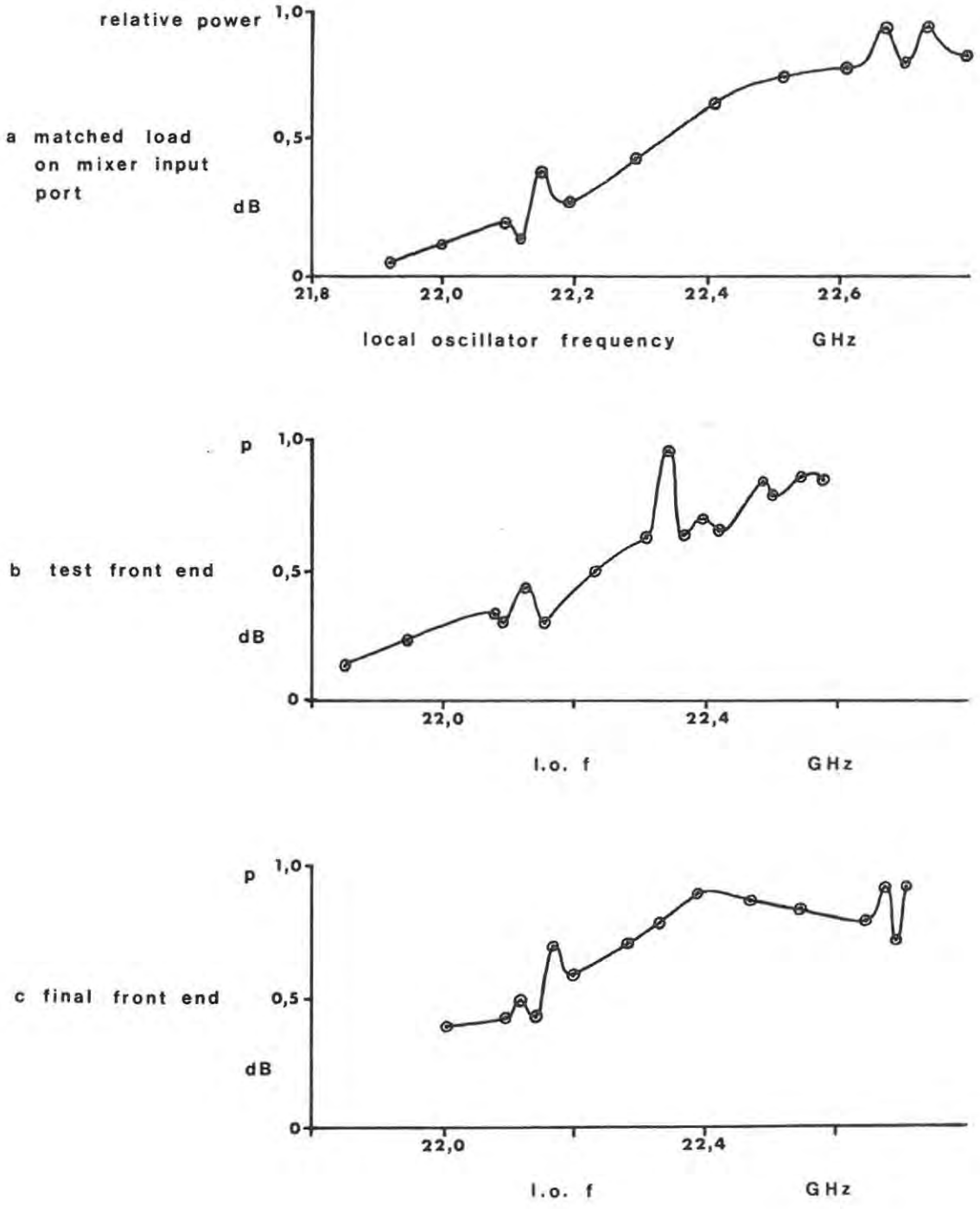

figure 3.7 FREQUENCY DEPENDENCE OF MIXER POWER OUTPUT

3.11 The Final Front End Layout

The layout (figure 3.8) was completely revised to incorporate the modifications and test results described above. The microwave switch was mounted so that the horns were connected symmetrically, to ports 2 and 3 instead of 1 and 2, to minimise VSWR differences in the two feeds which had been noted in the earlier arrangement. The circulator was mounted between the mixer and switch so that the attenuated l.o. signal which has passed through the mixer is transmitted to the matched load on port 3, the incoming signal passing directly from port 1 to 2.

The local oscillator arm was designed so that either type of Gunn diode could be mounted, a precision variable attenuator being used to obtain the correct power level. The minimum attenuation between the l.o. and mixer is 11,4 dB, through the 10 dB coupler. The attenuator is normally set at 12,0 dB for the Varian S Gunn. The mixer is mounted directly on the baseplate, the waveguide to the horns and noise tube lying in a plane above it. The beam separation is now $2{,}0^{\circ}$, or 4,4 beamwidths. The attenuation between the primary horn and mixer is 0,70 dB, and between the reference horn and mixer 0,53 dB. A precision variable attenuator is mounted between the noise tube and 20 dB coupler in the line from the primary horn. The minimum attenuation between the noise tube and mixer is 22,0 dB, giving a maximum calibration signal of 80 K, as seen in figures 5.1 and 5.2. For spectral line calibrations a microwave switch capable of 95 Hz operation should be included in the noise tube line, as the present calibration system requires beam switching.

Five waveguide sections in the layout were made in the workshop: two straights, that to the primary horn having 0,10 dB insertion loss; the long reflex bend to the reference horn (0,15 dB i.l.); the

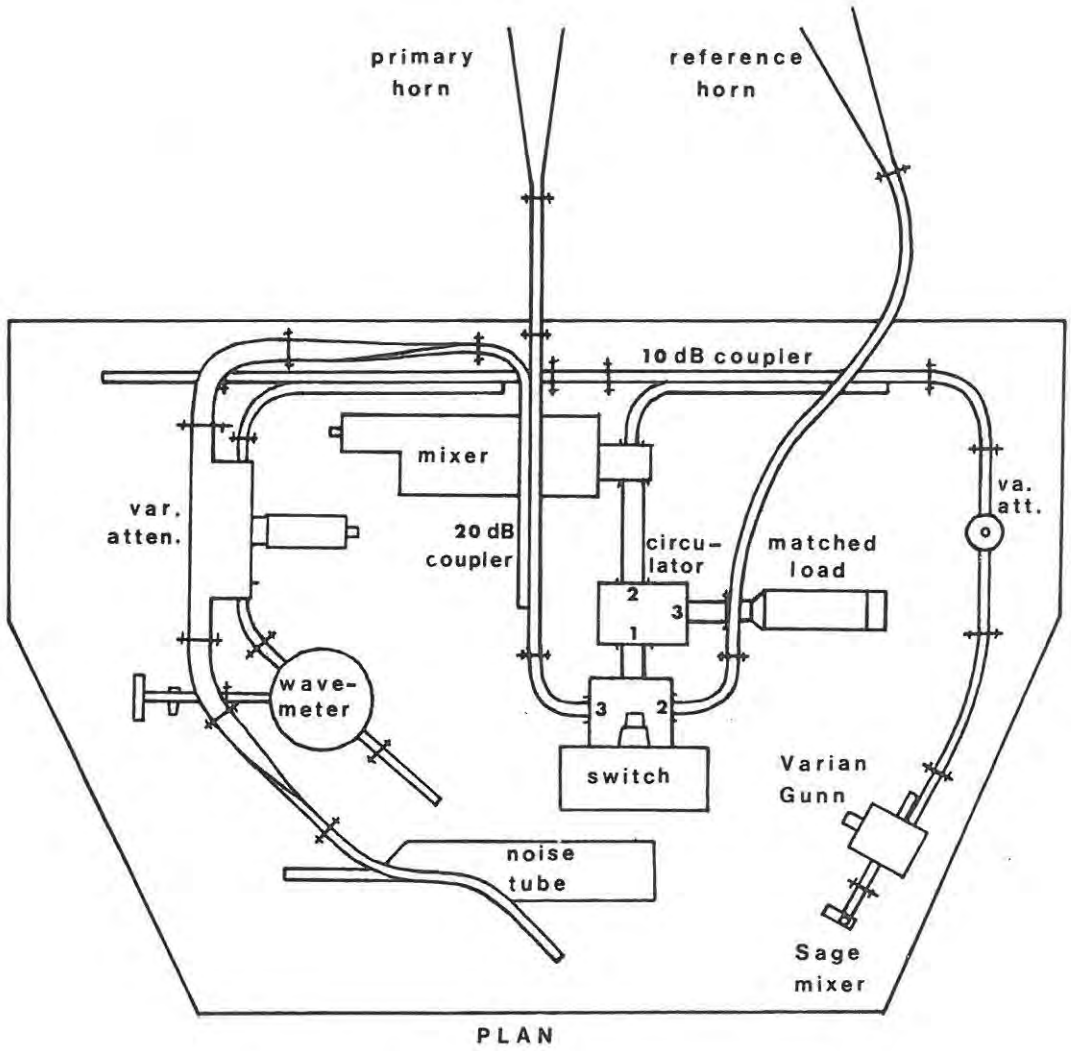

figure 3.8 FINAL FRONT END

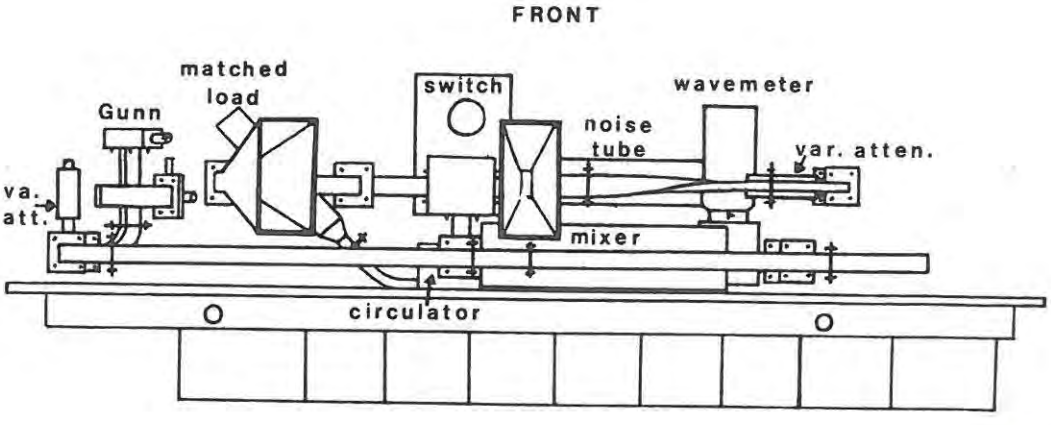

reflex bend between the mixer and circulator (0,1 dB i.l.); and the 30° bend to the Gunn diode (0,09 dB i.l.). The Varian Gunns are mounted on a 90° bend with a 20 dB coupler for the Sage mixer, but the Mid-century Microwavegear Gunn is connected directly onto the 30° bend.

To ensure linear operation of the Trontech i.f. amplifier, mounted on the reverse side of the baseplate, an attenuator has been included after the mixer, and is normally set at 5 dB.

Following bench testing of the front end, a new hole was cut in the paraboloid to accommodate the reference horn. The framework supporting the front end was redesigned for greatly increased rigidity while still providing for movement along three perpendicular axes for antenna alignment. After assembly the antenna was refocused using the sun as a test source.

CHAPTER FOUR

THE CONTINUUM AND SPECTRAL LINE RECEIVERS

4.1 The continuum receiver

4.2 The spectral line receiver

4.3 The automatic gain controls

4.4 System Sensitivity

CHAPTER FOUR

THE CONTINUUM AND SPECTRAL LINE RECEIVERS

Operation of the 22 GHz telescope to date has been with the continuum receiver as a back end. Source tracking by the antenna, which is not yet available, is needed for spectral line work owing to the long integration times needed at this frequency. The spectral line receiver has been used for test observations at lower frequencies. The gain control circuits and chart recorder drive described in this chapter were designed with Way-Jones.

4.1 The Continuum Receiver

The continuum receiver was originally mounted in the mainframe housing the spectral line receiver, control logic trays, and power supplies, but has since been divorced from it to allow for simultaneous spectral line observations elsewhere. Regulators in the receiver tray convert + and - 20 V D.C. to the necessary supply voltages for the receiver and chart recorder drive housed within the tray. The 95 Hz switch signal for the front end and receiver is provided by a Beckman 9030 signal generator, and start/stop buttons in the tray connected to a + 24 V power supply allow for remote control of the front end noise tube.

A schematic diagram of the continuum receiver is given in figure 4.1. The 10-110 MHz signal from the i.f. amplifier (figure 3.2e) is rectified by the diode, and passes through the 95 Hz filter to an adjustable gain amplifier. At this point the signal is a 95 Hz square wave, the magnitude of which corresponds to the difference in mixer output power when switching between the two beams. During half

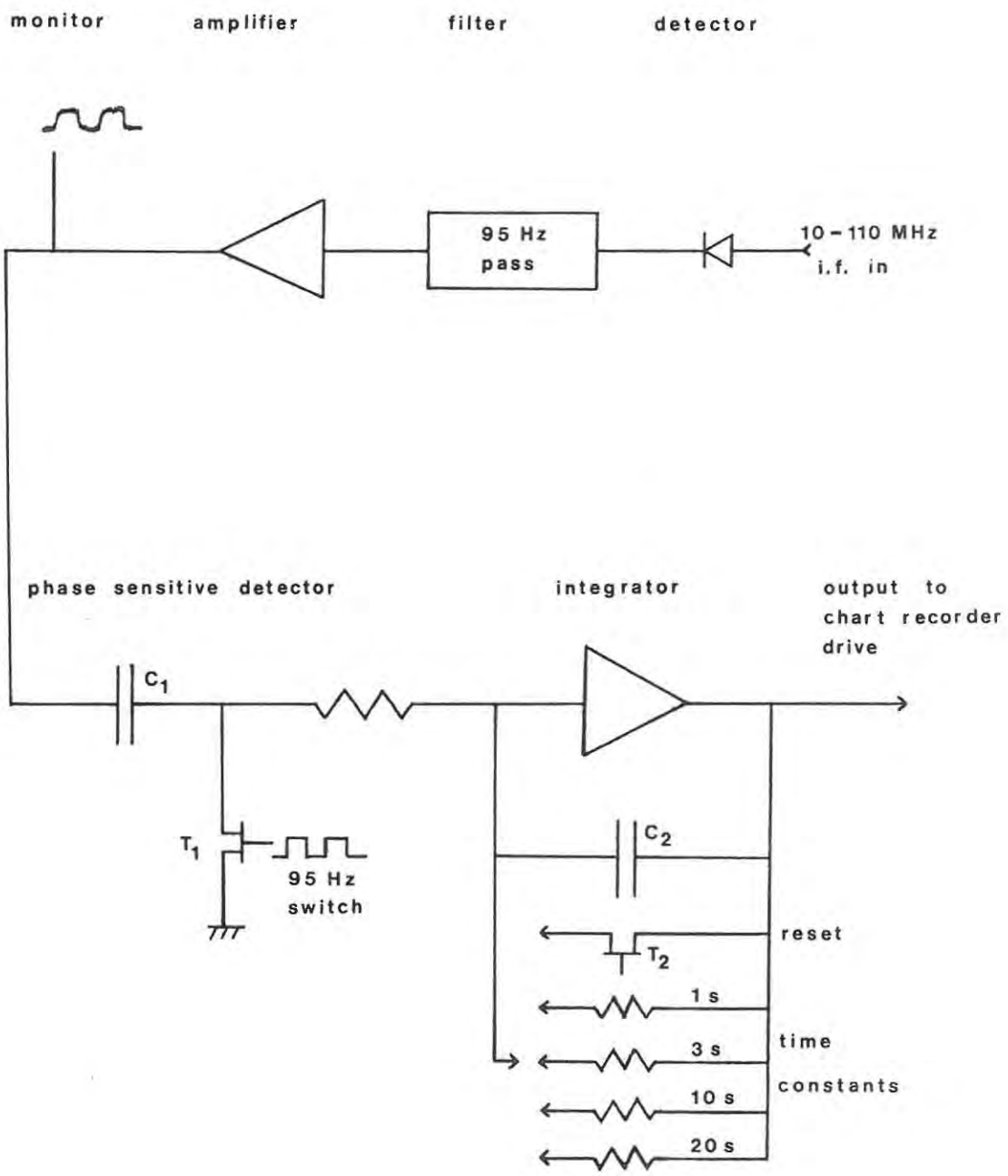

figure 4.1 THE CONTINUUM RECEIVER

the switch cycle the f.e.t. switch T_1 in the phase sensitive detector is 'closed' and grounds the output side of capacitor C_1; the input side of C_1 is then at the voltage corresponding to the sky background signal. During the second half cycle, when T_1 is 'open', the input side of C_1 is at a voltage corresponding to the source plus background signal and the output side is now at the difference in voltage between the two signal levels, which is that due to the source alone. This latter voltage charges up the integrating capacitor C_2, which may be discharged after a set period by closing the f.e.t. switch T_2, or may charge continuously with one of four resistors across it providing RC decay constants of 1, 3, 10 or 20 seconds. This arrangement for the variable time constant is unsatisfactory in that the gain of the integrating amplifier is proportional to the time constant, and should be replaced by a fixed resistor with alternative capacitors. Integrator drift is controlled by two potentiometers giving coarse and fine adjustment. The integrator (or detector) voltage is connected to the chart recorder drive, in which two op-amps are used to set the scale ranges via a ganged switch, and to provide a zeroing adjustment for the chart recorder.
The signal can be monitored continuously on a chart recorder. Alternatively the integrator output may be connected to the multiplex unit of the spectral line receiver, where it is sampled by a digital voltmeter (section 4.2).

Receiver temperature variations cause integrator output drift; however an eight hour period in an overnight drift scan on a 1 s time constant, without front end or receiver thermal control, showed a drift of less than 1K. Temperature control is necessary when timed integration of the signal is required. Observations made with the continuum receiver are described in chapter five.

4.2 The Spectral Line Receiver

The spectral line receiver consists of forty-nine contiguous channels, each of 50 kHz bandwidth , covering the frequency range from 28,80 to 31,20 MHz. The design was optimised for the study of cosmic water masers, in conjunction with the 22 GHz front end. Its operation with the latter is described below.

The 25-35 MHz RHG i.f. amplifier output (figure 3.3d) is carried to the primary distribution amplifier, of small overall gain, which passes it to five trays containing ten channels each. Further distribution amplifiers in the trays supply the signal to each channel. These contain crystal-controlled local oscillators, the signal from which is mixed with the incoming i.f. signal in a dual gate f.e.t. The difference frequency output is limited by a 25 kHz low pass filter, giving 50 kHz bandwidth centred on the channel l.o. frequency (figure 3.3e). As described for the continuum receiver, the signal passes to an adjustable gain amplifier, followed by the diode rectifier, filter, amplifier, phase sensitive detector, and integrator, which has a reset f.e.t. only. At the end of a given integration time the integrator voltage in each channel is read sequentially by a digital voltmeter via a multiplex unit and the integrators are then reset to zero. The voltmeter readings are displayed as a histogram on an oscilloscope (figure 3.3f) and punched out on paper tape or transferred directly to an on-line computer.

This author was largely responsible for the construction and testing of thirty of the spectral line channels and for their experimental use during two observation periods at the Hartebeesthoek Radio Astronomy Observatory. The first trial revealed that the distribution amplifiers were inadequate and they were replaced by an improved design. During

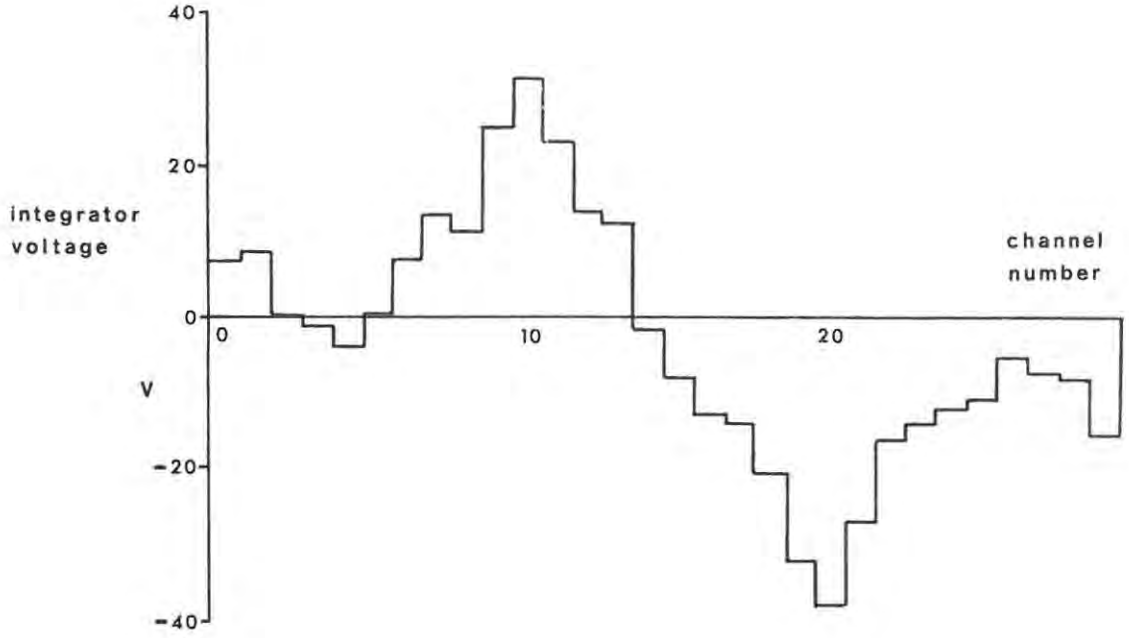

figure 4.2 2272 MHz HYDROGEN RECOMBINATION LINE IN ORION A

the second period the receiver was used as a back end to the 26 m telescope, which has a 33 K system temperature, to observe the hydrogen recombination line at 2272,661 MHz. Observations were also made of Galactic neutral hydrogen at 1420,405 MHz, using a 1 GHz horn connected to the RHG 1-2 GHz mixer and preamplifier (Appendix 4a). Only thirty channels were then available, the limited bandwidth preventing adequate baselines for spectra from being obtained.

Observations were made in pairs, with the phase of the switch signal reversed for the second run. On subtracting the two voltages from each channel the signal added but the drift voltage cancelled. Background runs made in the same way were subtracted from the on-source runs, and the signal in each channel was then multiplied by the normalised gain of that channel. A hydrogen recombination line spectrum obtained from twenty minutes integration on Orion A is shown in figure 4.2. Frequency switching was carried out with an l.o. frequency difference of 500 kHz so that any spectral line would appear as two antiphase integrator

voltage peaks separated by ten channels. The frequency resolution is rather poor as the channel bandwidth was designed for use at 22 GHz, rather than 2,27 GHz, because for a given velocity v of approach or recession, the frequency shift $\Delta\nu$ is proportional to the frequency ν (Kraus, 1966, page 364):

$$\pm \Delta\nu = (\mp v)\nu / c \qquad 4.1$$

where C = speed of light.

The signal to noise ratio was worse than expected, probably due to interference with the i.f. signal.

The remaining twenty channels were completed subsequent to the second set of test observations. To minimise possible i.f. interference the 95 Hz switch signal distribution amplifier was removed from the tray housing the RHG i.f. amplifier and installed in a separate tray. The RG 174 50 Ω cables carrying the i.f. and switch signals to each tray were replaced by the thicker RG 58 u 50 Ω cable which has better radiation shielding. A 60 to 30 MHz downconverter was installed in the i.f. tray to allow the Hartebeesthoek 60 MHz amplifier to be used, this having a lower noise figure than their 30 MHz amplifier.

4.3 The Automatic Gain Controls

Variations in the signal strength to the spectral line receiver are caused by mixer and amplifier gain fluctuations and the elevation dependent antenna temperature. This results in spurious signals in the receiver if the variation has a 95 Hz component. To minimise this the i.f. amplifier output power can be maintained at the optimum operating level with an automatic gain control (AGC) circuit. In the continuum receiver, where the source itself may cause large changes in the i.f. power levels (up to 6 dB from the sun), an AGC has not been used. The

AGC s were designed to provide two time constants (τ); one very slow compared to 95 Hz, with a τ of 1 s or more, and one fast acting, with a τ of less than 100 μ s. When the signal is completely buried in noise either τ can be used, the fast AGC correcting for both rapid and slow gain variations, but if the signal is above the noise level the slow AGC must be used to prevent loss of signal through the AGC action.

The RHG i.f. amplifier has a facility for an AGC circuit. An AGC output provides a D.C. voltage derived from the i.f. power level, and an AGC input into which a D.C. voltage may be fed to control the amplifier gain. There is also a manual gain control and an AGC delay, the former normally being set for maximum gain and the latter for minimum delay.

The first AGC designed for the amplifier (figure 4.3) used a 2,2 MΩ resistor with a capacitor to earth for a simple RC time constant. Two slow time constants of approximately 5 s and 2 s were provided by 2,2 μ F and 1 μ F capacitors, and the fast time constant was obtained with the switch open, using the circuit capacitance. The 741 op-amp is a buffer amplifier to provide the necessary current. The manual on/off switch is in parallel with a GB 814 A electronic switch, operated by a TTL signal via the BC 107 transistor driver, for remote control. The output is connected by an AGC select switch to the AGC input of the RHG amplifier.

Following the operation of the receiver at Hartebeesthoek it was decided that the effects of passband shape change with l.o. frequency, or of i.f. passband ripple, might be better controlled by an AGC responding only to the bandwidth covered by the spectral line channels. This uses one i.f. output from the primary distribution amplifier, of 2,5 MHz half power bandwidth. The i.f. signal passes through a D.C.

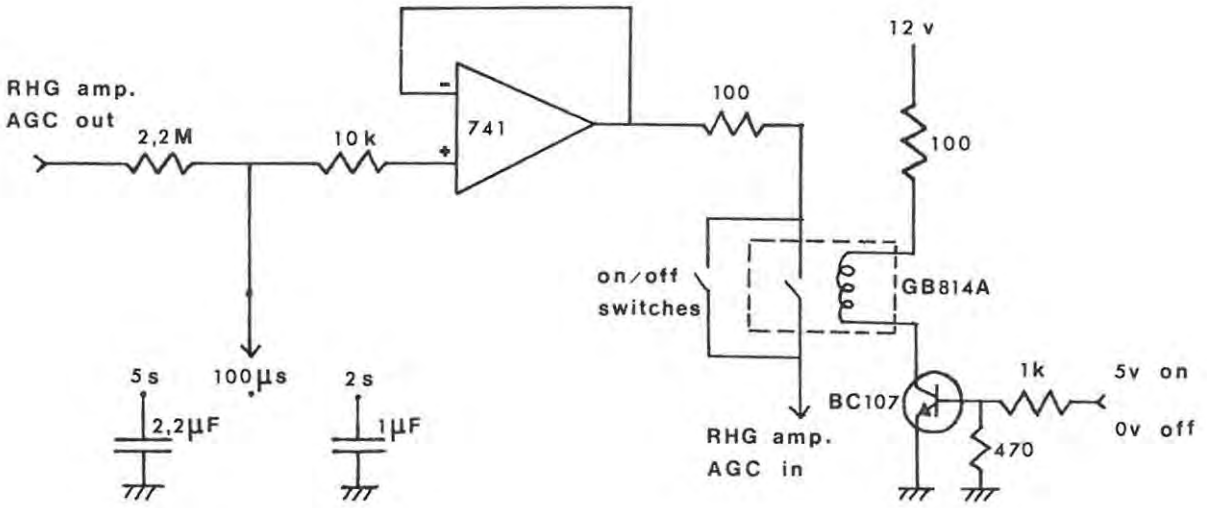

figure 4.3 10 MHz BANDWIDTH I.F. AMPLIFIER GAIN CONTROL

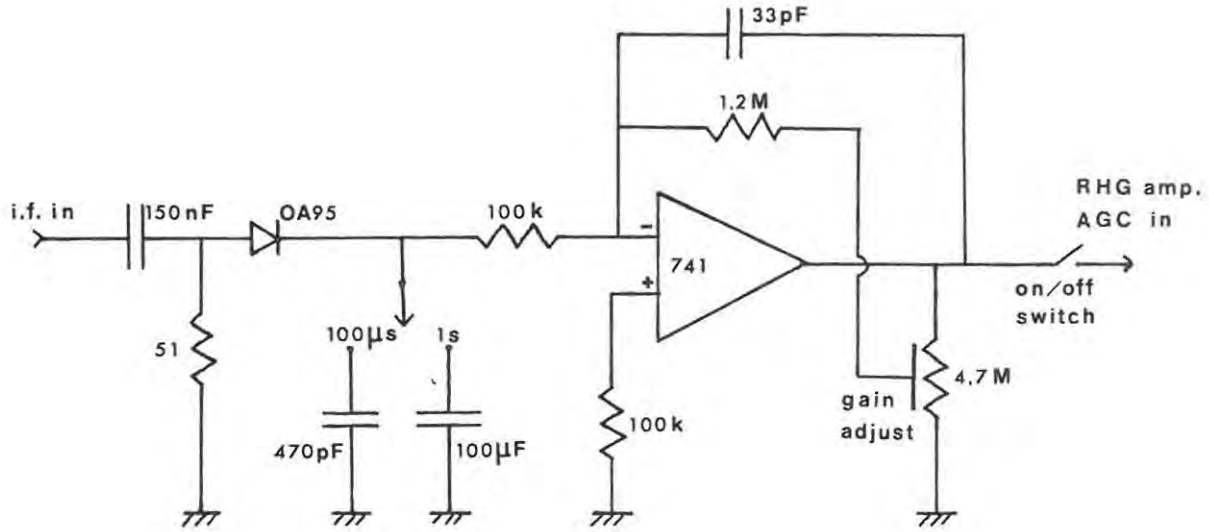

figure 4.4 2,5 MHz BANDWIDTH I.F. AMPLIFIER AGC

isolating capacitor with a 51 Ω resistor for impedance matching and is rectified by an 0A95 germanium diode (figure 4.4). Two capacitors to earth in conjunction with the 100 k Ω resistor provide the fast and slow time constants. The D.C. output is amplified by an adjustable gain 741 op-amp to set the required output level for the RHG amplifier. The 33 pF capacitor prevents high frequency oscillations.

Performance of the circuits has been verified by observing the output of the RHG amplifier with a spectrum analyzer while the i.f. input was alternated between two power levels at 95 Hz by a switchable attenuator in the i.f. line.

4.4. The System Sensitivity

The sensitivity of the receivers, expressed as the minimum detectable temperature, is primarily determined by the system temperature and predetection signal bandwidth. The continuum receiver detects the signal in both mixer i.f. sidebands of 100 MHz bandwidth , but in each 50 kHz bandwidth spectral line channel the signal occurs in only one sideband. The system temperature T_{sys} (Kraus, 1966, page 240) is the sum of the antenna temperature T_A and the effective receiver temperature T_{RT}:

$$T_{sys} = T_A + T_{RT} \qquad 4.2$$

The antenna temperature T_A consists primarily of the sky temperature, which is 30 K or more, while the effective receiver temperature T_{RT} is given by

$$T_{RT} = (L_1 - 1)\, T_o + L_1\, T_R \qquad 4.3$$

where T_o = temperature of front end (300 K)

L_1 = primary horn to mixer attenuation (0,70 dB)

T_R = effective mixer temperature.

The minimum detectable temperature ΔT_{min} is given by Kraus (1966) page 102 as

$$\Delta T_{min} = K_S T_{sys} / (\Delta\nu \; t \; n)^{\frac{1}{2}} \qquad 4.4$$

where K_S = sensitivity constant of receiver

$\Delta\nu$ = predetection bandwidth

t = postdetection integration time

n = number of records averaged

Owing to the beam- or frequency-switching the signal is seen half the time, with square wave modulation, so the sensitivity is half what it would be if the signal were seen continuously. Consequently the minimum detectable temperature is double that for continuous detection, and $K_S = 2$.

For the continuum receiver the double sideband mixer temperature $T_R = 570$ K at 22,2 GHz (Chapter three).

then $T_{RT} = 720$ K

and $T_{sys} \geqslant 750$ K

$\Delta\nu = 100$ MHz

hence $\Delta T_{min} \geqslant 0{,}15/(tn)^{\frac{1}{2}}$ K 4.5

For the spectral line receiver the single sideband mixer temperature $T_R = 1140$ K at 22,2 GHz

then $T_{RT} = 1390$ K

and $T_{sys} \geqslant 1420$ K

$\Delta\nu = 50$ kHz

hence $T_{min} \geqslant 12{,}7 / (tn)^{\frac{1}{2}}$ K 4.6

The figure for the minimum detectable temperature ΔT_{min} may be checked in practice as ΔT_{min} is equivalent to the r.m.s. system noise temperature T_{rms}, which is approximately one third of the peak to peak temperature fluctuations such as are exhibited by the continuum receiver in figure 5.4. The peak fluctuation with a one second decay constant on the integrator is 0,5 K, giving T_{rms} = 0,17 K, in good agreement with the figure of 0,15 K calculated from equation 4.5.

The minimum detectable flux density ΔS_{min} may be calculated from T_{min} as (Kraus, 1966, page 99)

$$S_{min} = 2 k\Delta T_{min} / \varepsilon_{ap} A_p \qquad 4.7$$

where k = Boltzmann's constant ($1,38 \times 10^{-23}$ JK^{-1})

ε_{ap} = aperture efficiency (0,57; section 5.11)

A_e = physical antenna area ($2,7$ m^2)

The minimum flux detectable by the continuum receiver is then

$$\underline{\Delta S_{min} \geq 270 / (tn)^{\frac{1}{2}}} \quad Jy \qquad 4.8$$

and by the spectral line receiver

$$\underline{\Delta S_{min} \geq 23000 / (tn)^{\frac{1}{2}}} \quad Jy \qquad 4.9$$

(1 Jy = 1 Jansky = 10^{-26} Wm^{-2} Hz^{-1})

For a single ten minute spectral line observation the minimum detectable flux is approximately 1000 Jy, which is typical of the intensity of a number of stronger water masers. The strongest observed features (in W49) reach 80 000 Jy.

The calculations above assume that atmospheric turbulence does not affect viewing, and do not allow for the increasing atmospheric attenuation with zenith angle (section 5.4). Consequently the results obtained are regarded as an upper limit on system sensitivity.

CHAPTER FIVE

OBSERVATIONS WITH THE TELESCOPE

5.1 Introduction

5.2 The predicted solar temperature at 22 GHz

5.3 The predicted lunar temperature and its variation at 22 GHz

5.4 Atmospheric attenuation theory at 22 GHz

5.5 Atmospheric attenuation measurements

5.6 Continuum observation theory

5.7 Corrections to observations for the aperture efficiency

5.8 Solar and lunar observations prior to the front end reconstruction

5.9 Later solar observations

5.10 Later lunar observations

5.11 The antenna efficiency

CHAPTER FIVE

OBSERVATIONS WITH THE TELESCOPE

5.1 Introduction

Observations of the sun and moon were carried out with the aim of deducing the aperture efficiency of the telescope. Precise knowledge of the solar and lunar temperatures at 22 GHz is necessary for an accurate determination of the efficiency. They have been measured extensively in the past, but there remains a relatively large uncertainty as to their correct values. A discussion is given on the sky temperature and atmospheric attenuation at this frequency, which can cause a considerable reduction in signal strength; measurements of the attenuation made following the front end reconstruction are compared to the predicted values. The attenuation is due primarily to the pressure-broadened water vapour absorption line at 22 GHz, the intensity of which depends on the water vapour content and air temperature .

The observation theory is derived, enabling the antenna temperature due to the source to be calculated from the output of the continuum receiver. This includes the corrections for factors such as the finite source size and the atmospheric attenuation. The aperture efficiency is then the ratio of the corrected observed source antenna temperature to the expected source temperature. Solar and lunar observations were made both before and after the front end reconstruction and antenna refiguring, and the aperture efficiency was calculated for both cases. Sky temperatures were measured during the later observations to enable the atmospheric attenuation factor to be calculated each time. In the final section the resulting aperture efficiencies are summarised.

5.2 The Predicted Solar Temperature at 22 GHz

The solar temperature at a given frequency in the microwave band shows little variation in the absence of flares. A summary of past measurements of the solar temperature at or near 22 GHz is given in table 5.1. The temperature starts to decrease fairly rapidly as a function of frequency above 25 GHz (Shimabukuro and Stacey, 1968), but this is masked by the errors in the measurements over the range shown. A mean temperature of 10250 $\pm$ 900 K was used in the calculations for the aperture efficiency on the basis of the quoted results.

The quiet sun may be regarded as a nearly uniform disc source at 22 GHz, measured fluctuations being less then 90 K (Fürst et al., 1974). The same authors showed that the small limb-brightening effect which had been predicted does not occur. Elzner (1976) suggests that this is primarily due to the presence of relatively cool spicules at 6000 K to 7500 K in the 10000 K chromosphere, which is that part of the sun observed at this frequency. Spatial fine structure has been observed in the solar emission (Kundu and Velusamy, 1974) and is probably associated with spicules. This structure would not be seen by the relatively broad beam of the Rhodes telescope. However solar flares may be very intense, and would be visible, as these are normally monitored by widebeam solar patrol antennas (Castelli et al., 1974). Wrixon and Hogg (1971) estimated that the slowly varying component of the solar emission probably contributes less than 1% to the solar flux at this frequency. Their measurements also indicated that the diameter of the radio sun exceeds the optical diameter by 3,1% at 16 GHz and 2,1% at 30 GHz.

Frequency (GHz)	Temperature (K)	Author
16,0	12005 ± 300	Wrixon and Hogg (1971)
16,7	9800	Fürst et al. (1974)
21,0	10800 ± 700	Staelin et al. (1968)
22,0	11000 ± 700	"
22,7	9700 ± 600	Efanov and Moiseev (1971)
23,4	10700 ± 700	Staelin et al. (1968)
25,0	8900	Fürst et al. (1974)
30,0	10479 ± 300	Wrixon and Hogg (1971)

Table 5.1 Solar Temperature Measurements

5.3 The Predicted Lunar Temperature and its Variation at 22 GHz

The moon behaves like a near-black body whose temperature varies with its phase as the surface heats and cools during the long lunar day. The phase variation of the microwave temperature lags behind the optical phase due to the thermal time constant of the lunar surface.

Theory and observations both indicate that the mean temperature T_c at the centre of the lunar disc decreases with increasing frequency. Linsky (1973) proposed a theoretical value for T_c of 240 ± 10 K at 22 GHz, predicting an enhancement of T_c centred on a frequency of 30 GHz. Observations do not appear to have confirmed this. Those summarised by Hagfors (1971) give the centre of disc temperature T_c as 220 K at 22 GHz, and the mean disc temperature T_d, averaged over the visible face of the moon, as 205 K, as there is limb-darkening due to the rough lunar surface. Krotikov and Schuko (1965) suggested that the mean disc temperature T_d is observed if the beamwidth is greater than 40'. That of the Rhodes telescope is 27' and so the observed temperature is weighted towards the

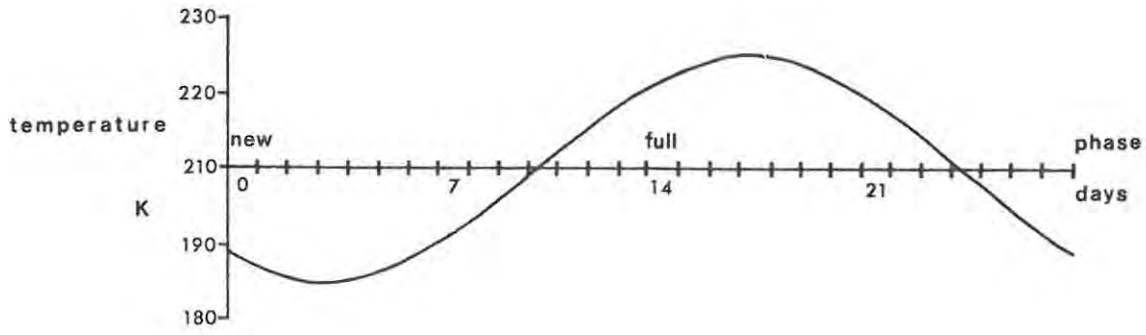

figure 5.1 LUNAR TEMPERATURE VARIATION AT 22 GHz

centre of disc value and should lie between T_c and T_d. This mean temperature has been taken as 210 K.

The surface temperature varies sinusoidally with the lunar phase. The range of the variation is approximately 15% of the mean temperature, or 30 K, and the lag behind the optical phase is 35 ± 10^{o} (Hagfors, 1971). The lunar temperature at 22 GHz is then given by

$$T_n = 210 - 15 \cos (12{,}86\ n - 35)\ K \qquad 5.1$$

for the n-th day in the lunar cycle. The accuracy is of the order of $\pm$ 10 K. The temperature variation from equation 5.1, used in calculations for the aperture efficiency, is shown graphically in figure 5.1.

5.4 Atmospheric Attenuation Theory at 22 GHz

At 22 GHz atmospheric attenuation is largely due to water vapour, with a small contribution from oxygen. The subject has been reviewed from a theoretical viewpoint by Staelin (1966, 1969), and the effects of clouds and rain have been discussed by Haroules and Brown (1969).

Crane (1971) has calculated the zenith attenuation in the absence of water vapour to be 0,03 dB, and with a saturated atmosphere to be 2,0 dB,

with a mean value of 0,30 dB. The attenuation range at any site would be affected by its altitude above sea level and the atmospheric temperature and humidity profiles. From observations Sullivan (1971) obtained an empirical relationship between the optical depth τ of the atmosphere and the water vapour density ρ in gm^{-3}:

$$\tau = 0,03 + 0,01\ \rho \qquad 5.2$$

The most complete set of measurements has been made by Fogarty (1975) at Itapetinga, Brazil, who found that the clear sky zenith attenuation varied from 0,2 to 2,6 dB.

The antenna temperature T_{sky} due to the atmospheric water vapour at a mean temperature T_{at} is given by

$$T_{sky} = T_{at}\ (1 - \exp\ (-\ \tau \sec z)) \qquad 5.3$$

where z = angle from zenith.

The sky may be regarded as a passive attenuator so that

$$T_{sky} = T_{at}\ (1 - 1/L_{at}) \qquad 5.4$$

where $L_{at} = \exp \tau \sec z$ = atmospheric attenuation (O'Brien et al., 1972).

Hence if T_{sky} is measured and T_{at} is known, the atmospheric attenuation may be calculated. This author has used a mean figure for T_{at} of 280 K (Fogarty, 1975), in the absence of radiosonde measurements.

The standard method for determining the sky temperature is to compare the sky signal with that from a matched load at a known temperature. In the present case this was carried out by replacing the reference horn with a matched load whose temperature was measured. The microwave switch was then either switched manually between the main beam and the termination, and the i.f. signal levels measured with a power meter, or normal beam-switching at 95 Hz was used, the continuum receiver output being monitored on a chart recorder. The first method required the

mixer temperature to be accurately known, but not the second, where the chart recorder trace is calibrated with the noise tube.

A second method for finding the atmospheric attenuation is to measure the variation in the observed temperature of a celestial source as a function of elevation (O'Brien et al. 1972). The procedure has been used in reverse by this author, to correct the observed source temperature after obtaining the atmospheric attenuation by the first method.

The effects of the elevation dependent sky temperature, and of atmospheric turbulence, are considerably reduced if a beam-switching system is used, with one beam on-source and the other off-source in an adjacent area of sky. This technique was first described by Conway (1963) and was developed by Baars (1970). Optimum use of the technique is made if the beams are in the same elevation plane, as the sky temperature is then the same in both beams. This is obtained with an altazimuth mounting when the reference feed horn is displaced horizontally from the primary feed, as in the revised front end (section 3.11).

5.5 Atmospheric Attenuation Measurements

The measurements were made as described in section 5.4, the sky temperature being compared to that of a matched load at ambient temperature. The elevation range covered was normally 20° to 90°, and T_{sky} was calculated from equation 5.9 or 5.10 (section 5.6) as appropriate. The atmospheric attenuation L_{at} was found using equation 5.4 rewritten as

$$L_{at} = T_{at} / (T_{at} - T_{sky}) \qquad 5.5$$

where T_{at} = mean atmospheric temperature (280 K assumed).

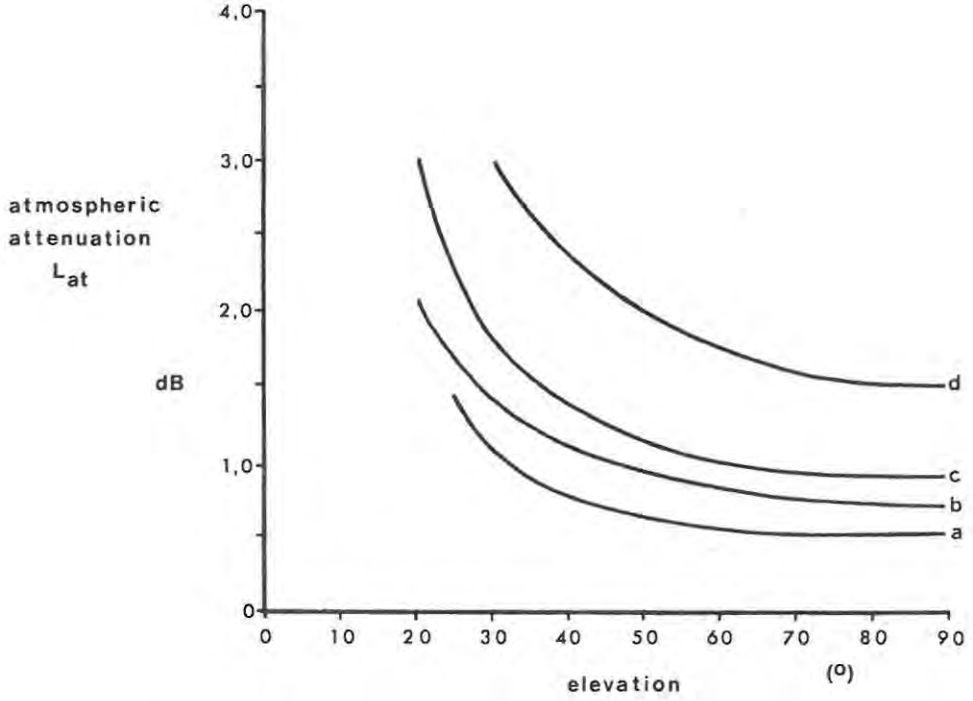

a clear sky, min. b standard atmosphere

c clear sky, max. d overcast

figure 5.2 ATMOSPHERIC ATTENUATION MEASUREMENTS

The lowest and highest clear sky attenuations measured are shown plotted as a function of elevation in figure 5.2 (curve a and c), and had zenith attenuations of 0,5 dB and 0,9 dB respectively. For comparison the attenuation observed on a heavily overcast day, with 1,5 dB attenuation at zenith, is given in curve d. The predicted attenuation of a standard atmosphere obeying the exp (- τ sec z) zenith angle factor (section 5.4) is depicted in curve b, using figures from Skolnik (1970) page 2-51. A small departure from the predicted type of curve is seen in the measurements below 30° elevation, and is caused by trees in the beam sidelobes. At a less obstructed site this effect would only be noticeable below about 10° elevation.

5.6 Continuum Observation Theory

The i.f. signal from the mixer is proportional to the microwave temperature seen by the mixer. When the primary beam is switched through to the mixer, and is off-source, the mixer sees its own effective temperature T_R, the sky temperature T_{sky} attenuated by the waveguide, the signal from the waveguide itself at a temperature T_o, and a small signal from the matched load terminating the unfired noise tube, also at T_o, seen through the 20 dB coupler (figure 3.8). The off-source primary beam temperature is then

$$T_1 = T_R + (1 - 1/L_1)\ T_o + T_{sky} / L_1 + T_o / L_2 \qquad 5.6$$

where T_o = front end temperature

L_1 = attenuation from primary horn to mixer

L_2 = attenuation from 20 dB noise tube coupler to mixer.

When the reference horn is switched through to the mixer, the latter again sees its own temperature, the attenuated sky signal, and that due to the waveguide:

$$T_2 = T_R + (1 - 1/L_3)\ T_o + T_{sky}/L_3 \qquad 5.7$$

where L_3 = attenuation from reference horn to mixer.

The small difference between these signals sets the baseline level on the continuum receiver integrator output, monitored on the chart recorder.

A source giving an antenna temperature T_S entering the main beam increases T_1 by T_S / L_1, the source temperature having previously been reduced by atmospheric attenuation and the loss in the antenna. This signal is seen as a departure from the chart recorder baseline. Alternatively, if the noise tube, at a temperature T_G, is fired, the temperature T_1 from the primary beam increases by $(T_G - T_o)/ L_4$

(Kraus,1966 , page 289), where L_4 is the attenuation from the noise tube to the mixer.

For sky attenuation measurements a matched load at a temperature T_{ml} replaces the reference horn, and the reference beam temperature T_3 becomes

$$T_3 = T_R + (1 - 1 / L_3)\ T_o + T_{ml} / L_3. \qquad 5.8$$

If 95 Hz beam switching is used the change in the integrator output is proportional to $T_3 - T_2$, which, rewritten to give the sky temperature T_{sky}, becomes

$$T_{sky} = T_{ml} - L_3\ (T_3 - T_2) \qquad 5.9$$

Alternatively, if the power meter is being used for a measurement of the outputs of the two beams, T_3 is being compared directly to T_1, and the sky temperature becomes

$$T_{sky} = L_1\ (T_3 - T_1) + T_o\ (L_1 / L_3 + L_1 / L_2 - 1) - T_{ml}\ L_1 / L_3 \qquad 5.10$$

Sky temperatures were only measured during the second period of telescope operation, when L_1 = 0,70 dB, L_2 = 21,0 dB, L_3 = 0,53 dB and L_4 = 22,0 dB. During early observations L_1 was approximately 0,4 dB.

5.7 Corrections to Observations for the Aperture Efficiency

Two equivalent methods can be used to obtain the aperture efficiency of the telescope. In the first method the real source temperature is divided by numerical factors to correct for effects such as the atmospheric attenuation and the finite source size, to obtain the antenna temperature that would be observed by an ideal antenna. The ratio of the actual antenna temperature to this predicted value gives the aperture efficiency.

Alternatively the observed antenna temperature is multiplied by the correction factors and the resulting predicted source temperature divided by the actual source temperature gives the aperture efficiency. The latter method has been followed by this author. The relevant correction factors are detailed below.

(a) Finite source size. For solar and lunar observations a correction must be made to the observed source temperature to allow for the finite source size. This has been analyzed by Baars (1973) and Stutzman and Ko (1974). The method of the former author gave a value for the actual half-power beamwidth θ_A, deduced from the observed value θ_o, similar to that expected from the aperture illumination (section 6.7), while that of the latter authors gave a value for θ_A 7% smaller than anticipated. This is unlikely to occur in practice, as factors reducing the aperture efficiency (section 6.7) cause a broadening of the main beam. Baars' method has been followed below.

For a disc source the observed temperature is multiplied by a correction factor K, assuming a Gaussian main-beam shape, such that

$$K = x^2 / (1 - \exp(-x^2)) \qquad 5.11$$

where $x = R / 0{,}6\ \theta_A$ 5.12

R = source radius.

The observed half-power beamwidth θ_o is that due to the convolution of the disc source with the beam pattern. The actual half-power beamwidth θ_A is given by

$$\theta_A = (\theta_o^2 - 0{,}5 \ln(2) \times (2R)^2)^{\frac{1}{2}} \qquad 5.13$$

(b) Receiver time constant. The second correction is that for the decay time constant on the integrator, which broadens the observed beamwidth, and decreases and delays the peak signal. For the 1 s and 3 s time constants the effect is negligible, but for the 10 s time constant the beam broadening and reduction in peak signal are both approximately 1% (Baars, 1973). Only the 1 s time constant was used in the later observations, so as to have the sun and moon recorded under the same conditions and to prevent saturation of the integrator.

(c) Waveguide attenuation. The observed signal is multiplied by the attenuation L_1 of the waveguide from the primary horn to the mixer (section 5.6).

(d) Atmospheric attenuation. This was discussed in sections 5.4 and 5.5.

(e) Mixer non-linearity. In the case of solar transits the non-linearity of the mixer for input signals equivalent to temperatures above 600 K must be allowed for. The apparent broadening of the observed half-power beamwidth θ_o due to the real reduction in peak height of a transit is used to correct the observed peak temperature. This gives a correction factor of approximately 1,15 for a typical observed solar temperature of 2000 K.

5.8 Solar and Lunar Observations Prior to the Front End Reconstruction

A number of solar transits were recorded during the early use of the telescope. The best of these was used for the antenna beam pattern program (section 6.5). The most accurate value of the observed solar temperature was that measured by Mutch (1975) page 81, and corrected by Baars (1976) to 2610 K. The half-power beamwidth θ_A of

$0,45^{\circ}$ and solar radius of $0,268^{\circ}$ gave a correction factor K of 1,57. The measured solar temperature quoted above allowed for waveguide losses and mixer non-linearity. The sky attenuation during the observation was not measured, but on the basis of later measurements was taken as $0,8 \pm 0,3$ dB. The resulting corrected solar temperature was 4850 ± 300 K, and dividing this figure by an assumed solar temperature of 10250 ± 900 K (section 5.2), the aperture efficiency was $0,47 \pm 0,04$.

Lunar transits through the primary beam were recorded on three days, but only on the last of these, on the 22nd April 1975, were sufficient reliable observations made to obtain a calibrated transit through the beam centre. This transit showed a peak antenna temperature of 45 ± 5 K, scaled from the calibrator. The correction factors applied to this were : K = 1,53; waveguide attenuation $L_1 = 0,4 \pm 0,1$ dB; assumed atmospheric attenuation = $0,8 \pm 0,3$ dB. These gave a predicted lunar temperature of 91 ± 10 K. The lunar phase was eleven days after new moon, giving an expected lunar temperature of 214 ± 10 K (section 5.3). The corresponding aperture efficiency was $0,42 \pm 0,05$.

This value is less than that obtained from the solar measurement owing to the beam overlap effect: the $0,6^{\circ}$ beam separation resulted in the coincidence of the first sidelobe of the reference beam and the primary beam mainlobe. During a source transit the antiphase signal from the reference beam caused a reduction in the peak intensity. The solar measurement used only the primary beam and consequently this effect did not occur, whereas for the lunar transit beam switching was used. The size of the loss is twice that predicted by the computed beam pattern (section 6.6), but the program made no allowance for sidelobe asymmetry in the offset beam, and the errors in the calculated efficiencies were of the same magnitude as the loss.

5.9 Later Solar Observations

Following the front end reconstruction and paraboloid refiguring an extended series of observations was made of the sun and moon in order to remeasure the aperture efficiency. All solar observations were made during June 1976, when the maximum elevation reached by the sun was 33°. Reliable observations could not be made below 20° elevation owing to trees in the immediate vicinity of the telescope. Measurements were only made under clear sky or light cloud conditions as visual positioning of the antenna on source was used, with the aid of a small optical telescope. A power splitter was used in the i.f. line so that the signal could be monitored at the telescope on a power meter. Following each set of observations the sky temperature was measured over a range of elevations, in order to find the atmospheric attenuation.

A typical solar transit is shown in figure 5.3, a twenty second noise tube firing being shown for comparison. The asymmetry to the left of the peak is due to the sun entering the reference beam, which was 2° west of the primary beam. The passage of the sun through the second sidelobes is seen by the presence of the two 20 K 'bumps' on either side of the main peak. The first sidelobe has been smeared into the mainlobe by the large angular size of the sun. A more sensitive chart scale was used for accurate measurement of sidelobe levels.

The observations are summarised in table 5.2. The correction factor K for all the measurements was 1,54, while the measured waveguide attenuation of 1,175 and non-linearity constant of 1,15 were used. The linear atmospheric attenuation for each observation is given in the table.

The corrected solar temperature averaged from the results is 5960 ± 180 K. Assuming a solar temperature of 10250 ± 900 K, the aperture efficiency is $0{,}58 \pm 0{,}04$.

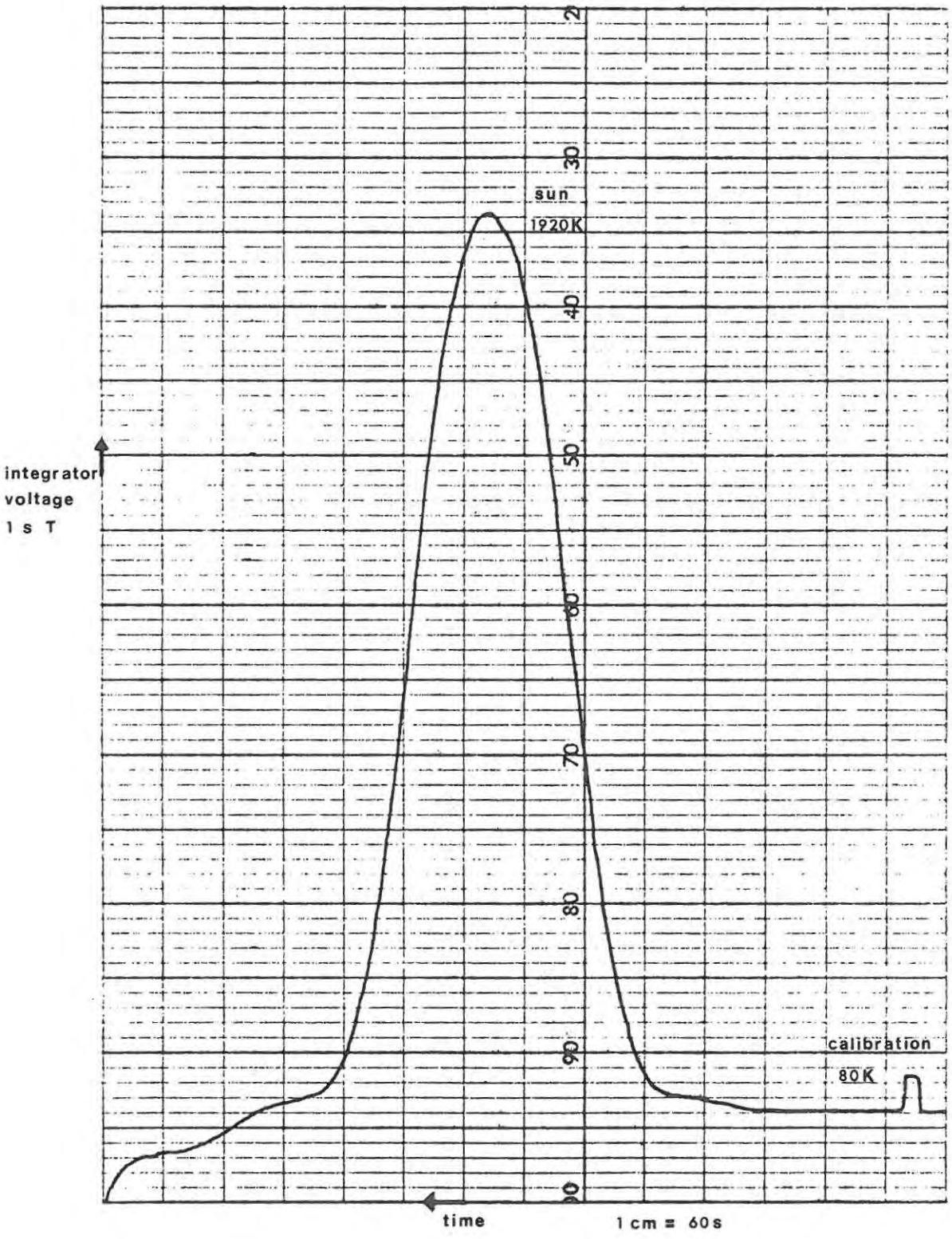

figure 5.3 TYPICAL SOLAR TRANSIT

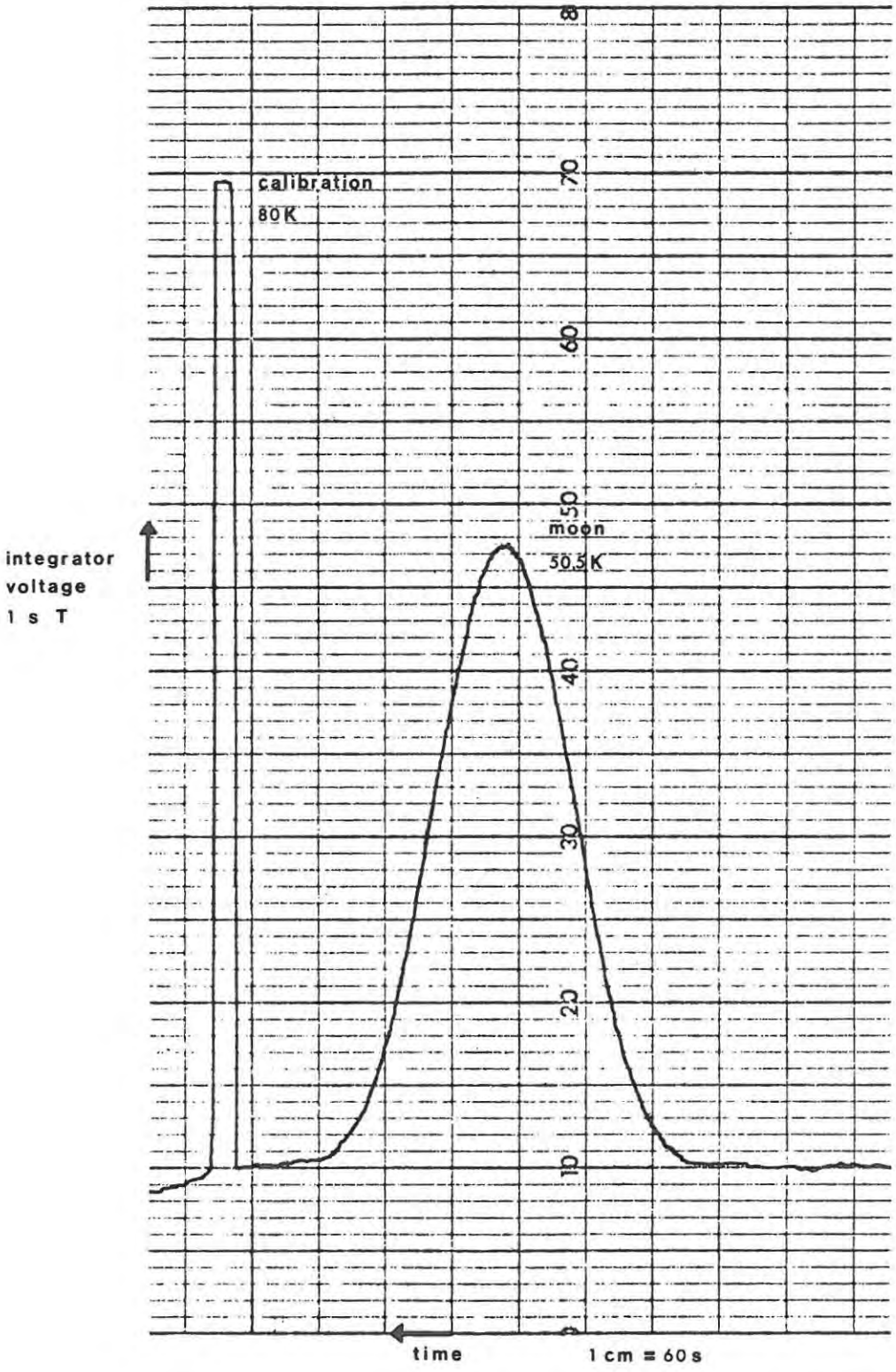

figure 5.4 TYPICAL LUNAR TRANSIT

Date (1976)	Elevation (^{o})	Observed solar antenna temp. T_S (K)	Atmospheric attenuation L_{at}	Corrected antenna temperature T_S (K)
9/6	33	1990	1,44	5980
10/6	33	2090	1,32	5730
11/6	33	2240	1,36	6340
"	29	2100	1,42	6210
12/6	32	2100	1,29	5640
14/6	24	1880	1,55	6060
"	28	2000	1,44	5990
"	30	2030	1,40	5910
"	32	2100	1,37	5990
17/6	32	2170	1,29	5820
24/6	24	2070	1,40	6020
"	27	2080	1,36	5900
"	28	2090	1,34	5840
"	27	2140	1,36	6060

Table 5.2 Later Solar Observations

Date (1976)	Elevation (^{o})	Observed lunar antenna temp. T_M (K)	Correction factors K	L_{at}	Corrected antenna temperature T_m(K)	Predicted lunar temperature (K)	Aperture efficiency
10/6	57,5	61,2	1,59	1,23	141	220	0,64
"	57,5	60,2	"	"	138	"	0,63
17/6	45,0	57,2	1,49	1,21	121	223	0,54
"	58,5	60,0	"	1,18	124	"	0,56
18/6	37,3	53,7	1,49	1,26	119	221	0,54
"	32,5	52,5	"	1,35	124	"	0,56
21/6	41,0	53,0	1,47	1,31	120	212	0,57
"	35,0	50,0	"	1,36	118	"	0,57
22/6	41,0	53,3	1,46	1,25	114	209	0,55
"	38,0	52,1	"	1,28	113	"	0,54
23/6	39,5	51,5	1,47	1,23	109	206	0,53
"	40,0	52,0	"	"	110	"	0,54
24/6	36,5	49,0	1,47	1,21	104	203	0,51
"	37,3	50,0	"	1,20	104	"	0,51
1/7	44,7	47,6	1,54	1,31	113	196	0,58
"	46,0	47,7	"	1,30	112	"	0,57
2/7	53,0	52,0	1,55	1,16	110	197	0,56
"	53,2	53,2	"	"	112	"	0,57
3/7	57,3	52,1	1,56	1,16	111	199	0,56
"	58,0	52,6	"	"	112	"	0,56
4/7	62,4	51,6	1,57	1,21	115	201	0,57
"	62,6	51,5	"	"	114	"	0,57
6/7	71,1	54,0	1,57	1,20	120	208	0,58

Table 5.3 Later Lunar Observations

5.10 Later Lunar Observations

Observations were carried out during June and July 1976 at a range of elevations between 32° and 71°. The antenna half power beam-width θ_A was calculated from a number of transits, using equation 5.13, the mean value being $0{,}453^{\circ}$, with a random error of $0{,}002^{\circ}$. The systematic error depends on the validity of assumptions in the theory. The mean figure was used for the calculation of the correction factor K for solar and lunar transits. As for solar observations the noise tube was fired before and after every transit, at least three being observed on each day. A typical lunar transit is shown in figure 5.4, again in comparison with the 80 K signal from the noise tube. The noise level of the receiver (section 4.4) is now just visible. The results are summarised in table 5.3; the observed lunar temperature is divided by the predicted temperature after the appropriate corrections have been applied to the former.

The mean value of the aperture efficiency, $0{,}56 \pm 0{,}04$, is in good agreement with that calculated from solar observations (section 5.9).

As the lunar measurements cover most of a lunar day, errors in the estimation of the lunar temperature range and phase lag cancel approximately in obtaining the mean aperture efficiency, but increase the error range. The accuracy of the mean lunar temperature affects all the calculations equally and remains a source of error in the efficiency. As the range of values for the efficiency is much larger than for the solar observations, the lunar temperature range has probably been underestimated and/or the phase lag overestimated.

5.11 The Antenna Efficiency

The observations during the first use of the telescope gave single and dual beam efficiencies of $0{,}47 \pm 0{,}04$ and $0{,}42 \pm 0{,}05$ respec-

tively, the dual beam efficiency being reduced by the beam overlap . Following the refiguring of the paraboloid surface and the front end reconstruction the beam overlap is negligible and the measured dual beam aperture efficiency has been raised to 0,58 $\pm$ 0,04, from solar measurements, and 0,56 $\pm$ 0.04,from lunar observations, or a mean value of ε_{ap} = 0,57 $\pm$ 0,04. The increase in aperture efficiency of 21% may be compared to the figure of 12% calculated from the paraboloid measurements (section 6.7). The discrepancy is probably due to better focusing of the antenna, and errors in the efficiency measurements.

The present beam efficiency is (Kraus, 1966, page 213)

$$\varepsilon_m = A_p \, \varepsilon_{ap} \, \Omega_m \, / \, (k_o \, \lambda^2) \qquad 5.15$$

where A_p = physical aperture area (2,90m^2)

Ω_m = beam solid angle

= 1,133 x θ_A^2 (0,233 deg^2)

or $\pi/4$ x beamwidth to first null (0,246 deg^2)

k_o = ohmic loss factor (assumed to be unity)

λ = wavelength (13,3 mm)

Substituting in these values ε_m = 0,62 $\pm$ 0,05.

The antenna beam pattern and factors affecting the antenna efficiency are discussed further in section 6.7.

CHAPTER SIX

THE CONVOLUTION PROGRAM AND THE ANTENNA BEAM PATTERN

6.1 Introduction

6.2 General description of program CONVOLVE

6.3 Convolution theory and its application to the program

6.4 The program source guidance routine

6.5 Solar and lunar transit scaling for the program

6.6 The beam pattern models

6.7 Factors affecting the beam pattern

CHAPTER SIX

THE CONVOLUTION PROGRAM AND THE ANTENNA BEAM PATTERN

6.1 Introduction

As part of the investigation into the low aperture efficiency measured during the initial observations (section 5.8), a computer program was written to obtain the antenna sidelobe levels. Ideally a strong point source was needed in the far-field of the antenna to map the beam pattern; as the telescope was surrounded by buildings an earth-bound transmitter could not be placed in the far-field and so celestial sources were used. At this frequency the sun and moon are the only strong sources, but are not pointlike, having angular sizes comparable to the antenna beamwidth. However if an extended source passes through the telescope beam, the receiver output is the convolution of the source brightness distribution with the antenna beam pattern (Kraus, 1966, page 68). The beam pattern can be obtained from direct deconvolution by differentiation of the slope of the transit curve (Baars, 1973), or by a computed simulation of the passage of the source through models of the beam pattern, comparing the output, representing the convolution envelope, with that of the actual transit. The latter method was chosen.

A general description of the program CONVOLVE, written for this purpose, is given in the second section, followed by a discussion on convolution theory and its application here. The program's source guidance routine which was used to simulate the path of the source through the antenna beam is detailed. The continuum receiver output from solar and lunar transits was scaled to provide the data against which the program output was compared (section 6.5), and the beam pattern which on convolution

gave the best fit to the observed data is illustrated and described in the penultimate section. Finally the predicted theoretical antenna pattern is compared with that obtained from the program, and the causes of loss of aperture efficiency are analyzed.

6.2 General Description of Program CONVOLVE

The program CONVOLVE simulated a transit of a uniform disc source through a model of the antenna beam, the position of which was assumed to be fixed, while the source could be at any declination and could pass within any desired distance of the beam centre. The program output represented a sampling of the integrator voltage, or convolution integral, at fixed time intervals, which was then compared graphically with a composite solar-lunar transit (section 6.5), and the model adjusted accordingly. For simplicity the beam model was taken to be a function of angle from the beam centre only (section 6.3). A program listing is given in appendix 6a.

The source size, angle of closest approach to the beam centre, the number and weighting of segments defining the beam pattern, and the sampling time interval were entered on cards. The source was initially at an hour angle of -12 hours with respect to the beam, and was moved in steps corresponding to the time interval towards it. The source to beam angle was calculated at each step; if the source was not in the beam the hour angle was incremented. Once in the beam, if partly over the beam centre some segments would be completely on source, and their 'volume', or contribution to the convolution integral, was calculated. The inner and outer summation limits for partly on-source segments was found, and their on-source 'volume' calculated, the total on-source 'volume' giving a point on the convolution envelope, after which the hour angle was incremented and the process repeated. Owing to the

assumed symmetry all the information was contained in the first half of the transit, the program stopping when the source was at the beam's hour angle.

6.3 Convolution Theory and its Application to the Program

The response of a radio telescope to a source in its beam is a convolution of the source brightness distribution and the antenna beam pattern (Braceweil and Roberts, 1954; Burr, 1955). If the antenna pattern is $f(x,y)$ and the source distribution is $h(x,y)$, the receiver output $g(x',y')$ is given by the convolution integral:

$$g(x',y') = \int_{-\infty}^{\infty} \int_{-\infty}^{\infty} h(x,y) f(x'-x,y'-y)\, dx\, dy \qquad 6.1$$

For simplicity circular symmetry was assumed for f, g and h to enable polar coordinates to be used, with $r^2 = x^2 + y^2$ 6.2

so $$g(r') = \int_0^{\infty} \int_0^{2\pi} h(r) f(r'^2 + r^2 - 2rr' \cos\theta)^{\frac{1}{2}} r\, dr\, d\theta \qquad 6.3$$

The source was assumed to be a uniform disc of radius r_o so

$$h(r) = k \quad r \leq r_o \qquad 6.4$$

$$= 0 \quad r > r_o$$

The real antenna pattern is not given by a simple analytic function because of effects such as aperture blockage and surface errors, so a numerical model was used where

$$f(r) = Z_n \quad n\Delta r < r \leq (n+1)\Delta r \qquad 6.5$$

and Δr = segment width

The convolution was carried out in practice by finding the areas of the segments defining the beam pattern which are on-source at a given moment, and these areas, multiplied by the relative power of the segments, give one point on the convolution envelope. The contribution

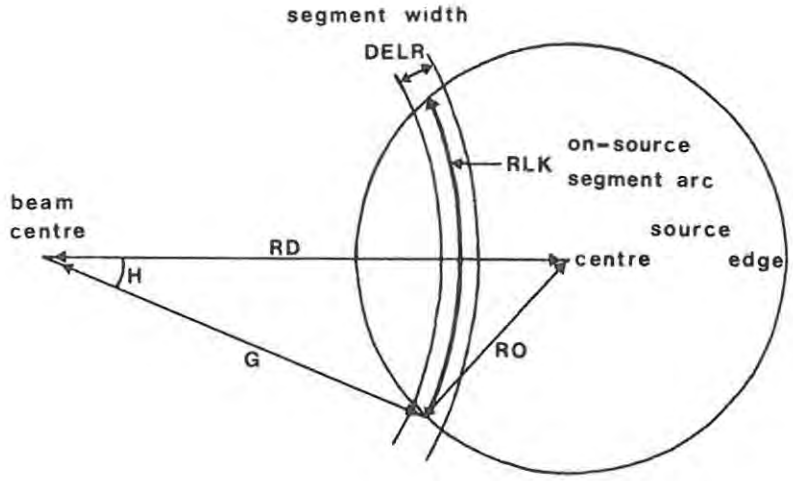

figure 6.1 COORDINATES FOR PARTLY ON-SOURCE SEGMENT

or 'volume' of the (K+1)th fully on-source segment of width DELR(Δr) and relative power Z(K+1) is

$$VDASH = 2\pi \times (DELR)^2 \times (K+0,5) \times Z(K+1) \qquad 6.6$$

The geometry for the contribution from a partly on-source segment is shown in figure 6.1. The on-source segment length is taken as the arc-length RLK between the points of interception of the source edge with the segment centreline. The source, of radius RO, is at a distance RD from the beam centre, while the centreline of the (K+1)th segment is at a distance G = (K+0,5) x DELR. If H is the half angle subtended by the intercepted arc RLK, then by the cosine rule

$$\cos(H) = (RD^2 + G^2 - RO^2)/(2 \times G \times RD) \qquad 6.7$$

The full subtended angle is THETAK, giving the arclength RLK = G x THETAK, and the segment 'volume' on-source is

$$VK = RLK \times DELR \times Z\ (K+1) \qquad 6.8$$

The final 'volume' at this point on the convolution envelope is

$$V(MM) = \Sigma\ VK + \Sigma\ VDASH \qquad 6.9$$

The true power distribution in the beam pattern cannot be completely restored as high spatial frequencies are lost in the convolution process owing to the large source size. However if the real pattern is assumed to have a similar principal spatial frequency to that of the theoretical pattern, i.e. if no extra sidelobes are introduced, the approximate sidelobe level can be deduced.

6.4 The Program Source Guidance Routine

In order to obtain the convolution envelope, the source must be guided along a path through the beam model simulating that of the actual transit, as shown in figure 6.2. If the celestial sphere is assumed to have unit radius, angles defining the object positions are numerically equal to the corresponding arc-lengths on the surface of the sphere. The source travels in a circle at declination DEC; the beam centre is a further distance RMIN from this, which may be negative, zero, or positive. The difference in hour angle, Q, changes with time, and the angle between the source and beam centres is given by the great circle arc RD:

$$RD = \arccos(\cos RMIN - \cos DEC \times \cos(DEC + RMIN)(1-\cos Q)) \qquad 6.10$$

This was derived from first principles, but is identical to the expression obtained using the cosine rule of spherical trigonometry, which, rewritten, becomes (Beste et al., 1974, appendix 5a)

$$RD = \arccos(\sin DEC \sin(DEC+RMIN) + \cos DEC \cos(DEC+RMIN) \cos Q) \qquad 6.11$$

6.5 Solar and Lunar Transit Scaling for the Program

A combined solar and lunar transit was used to provide the real convolution envelope with which the program output was compared

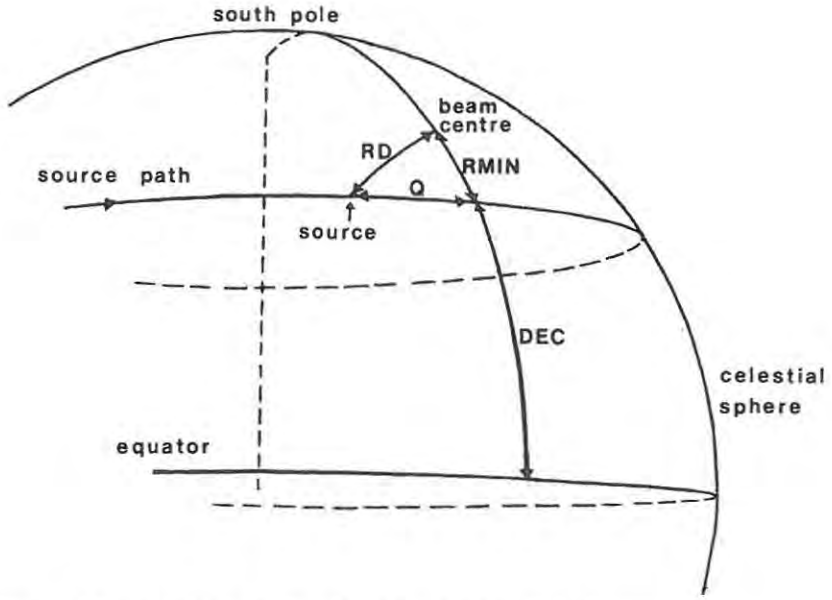

figure 6.2 SOURCE GUIDANCE COORDINATES

The sun gives the best signal to noise ratio, but when in the beam mainlobe the antenna temperature is over 600 K, and the mixer output becomes non-linear (section 5.7). To compensate for this a lunar transit taken under the same operating conditions was multiplied by the ratio of the solar and lunar temperatures (sections 5.2 and 5.3) and used to provide the data for the centre of the transit. Allowance was made for the slightly different solar and lunar sizes during the two observations, and for their differing angular velocities.

The output from the continuum receiver integrator on a 1s decay constant was used, replotted in decibels below the centre of transit level. The basic solar transit is shown in this fashion as the continuous curve in figure 6.3, while the scaled up lunar transit is depicted by the long dashes, which merged with the solar transit near the 300 s elapsed time mark. The reduced output towards the centre of the solar transit due to mixer non-linearity is evident.

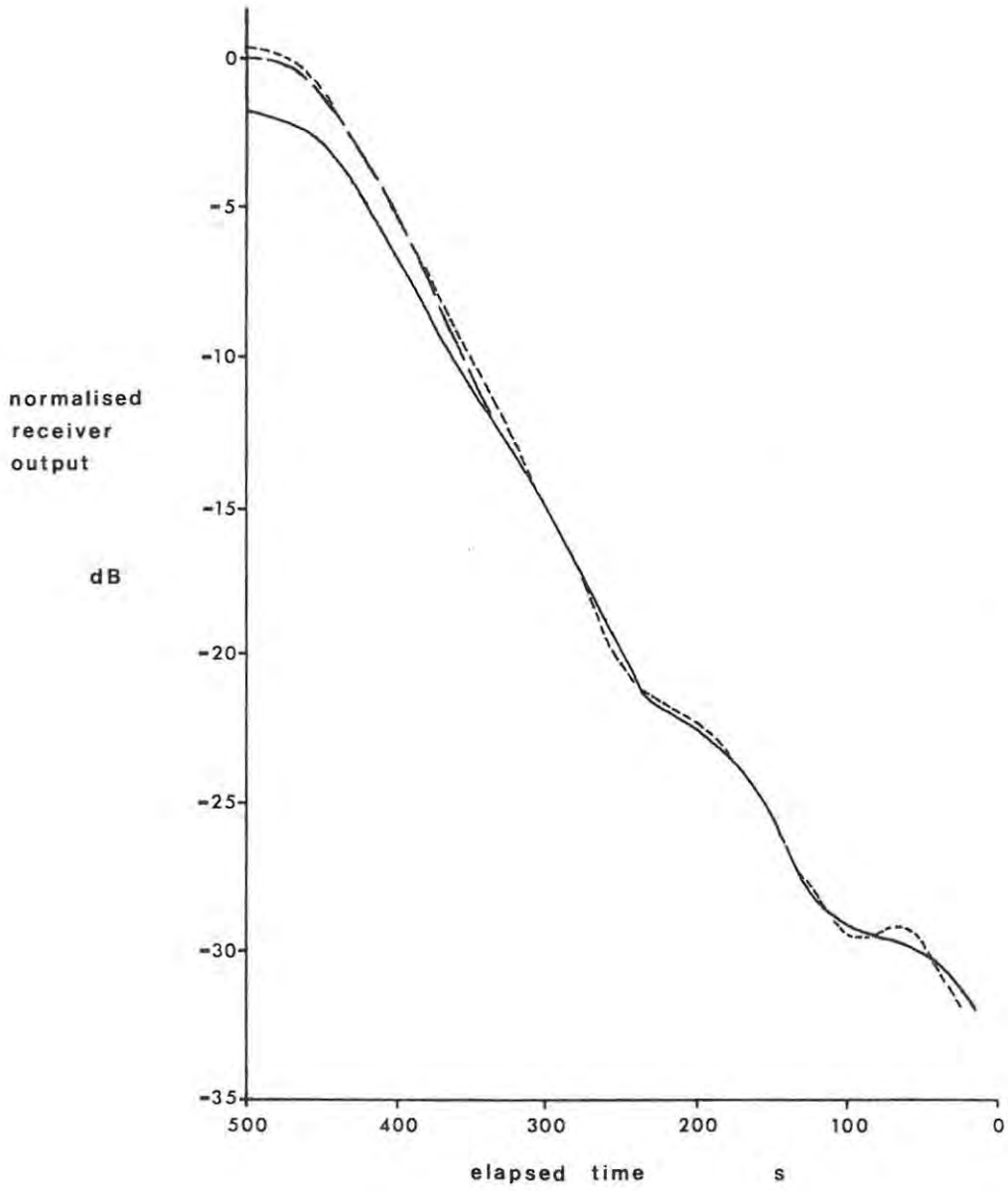

——— solar transit
— — — scaled-up lunar transit
------- best-fit beam pattern convolved

figure 6.3 COMPARISON OF REAL AND COMPUTED TRANSITS

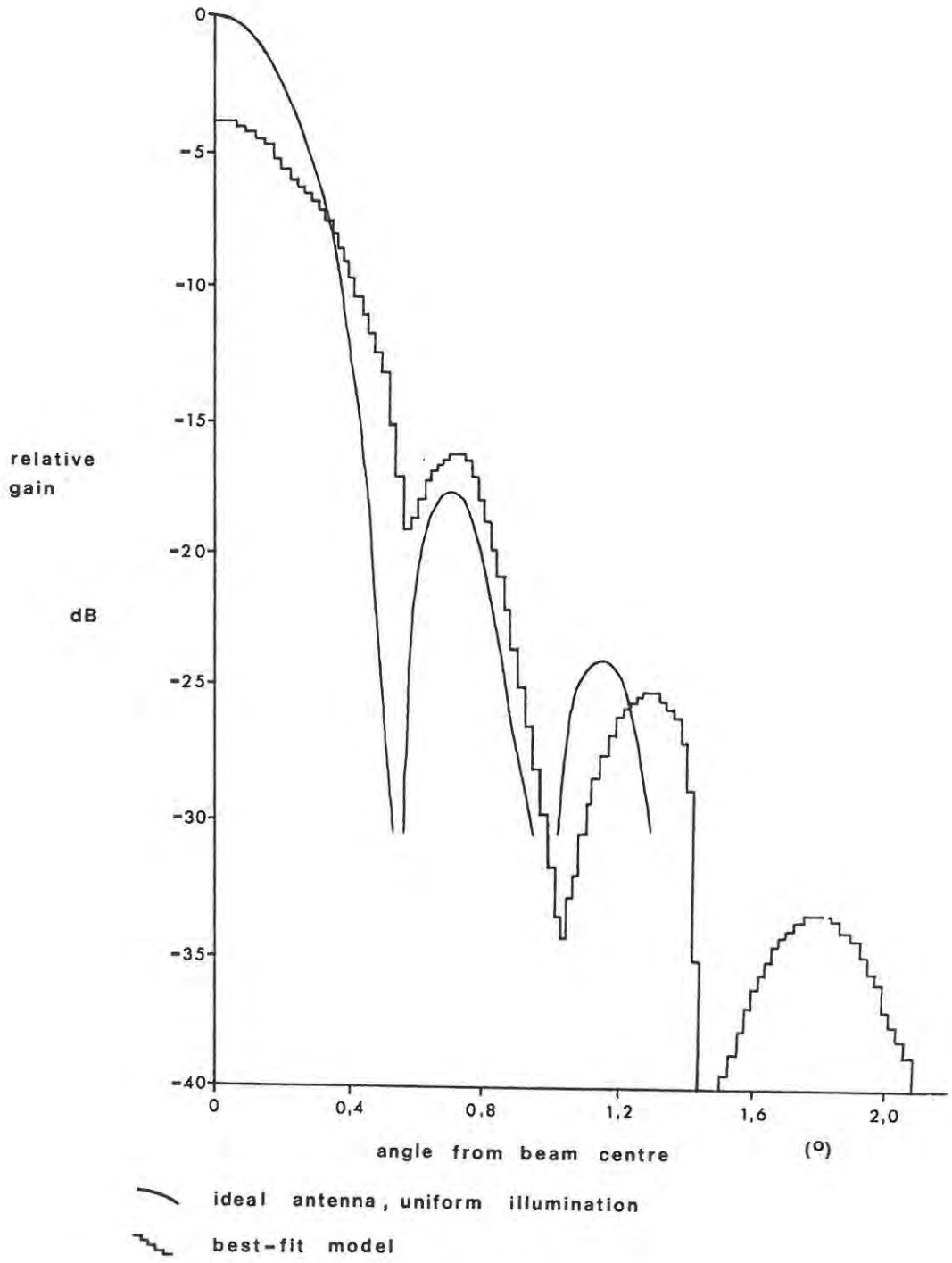

figure 6.4 ANTENNA BEAM PATTERNS

6.6 The Beam Pattern Models

The beam pattern used to provide the approximate sidelobe contours from which the model pattern was developed,was that for an ideal, uniformly illuminated, circular aperture (Silver, 1965, page 193), illustrated in figure 6.4, where the mainlobe and first two sidelobes are shown in cross-section. At this time the telescope had a beam separation of $0{,}6^{\circ}$ in the elevation plane. To allow for the loss of signal caused by the beam overlap, for each programmed transit through the primary beam a transit was run with the source passing $0{,}6^{\circ}$ from the beam centre and the two sets of data were subtracted. The reduction in peak signal was strongly dependent on the first sidelobe level, and was 5% in the best-fit model pattern discussed below.

Twenty three models were evaluated, and that giving the best fit to the composite transit is shown as the stepped function in figure 6.4. The real pattern would be a smooth curve through the steps. The mainlobe level of the model pattern was normalised by assuming the 47% aperture efficiency calculated in section 5.8, the uniform illumination pattern being 100% efficient. Owing to the transit scaling assumptions the absolute accuracy is approximately $\pm$ 1 dB. The reasons for the differences between the two illustrated antenna patterns are discussed in the following section.

The fit given to the composite transit is shown in figure 6.3. The greatest error is 0,5 dB and the r.m.s. error is approximately 0,2 dB. Particularly noticeable in the transit is the 'smearing' of the first sidelobe with the mainlobe, the first null position being nearly indistinguishable. By contrast the passage of the sun through the outer sidelobes leaves them relatively well defined.

6.7 Factors Affecting the Beam Pattern

The gain and sidelobe levels for the computed beam pattern, and that predicted for the telescope, can now be compared. The angular extent and levels of the antenna beam sidelobes are primarily determined by the ratio of the wavelength λ to the aperture diameter d, and the power distribution of the antenna feed pattern.

The aperture distribution of the feed pattern was chosen by Nunn (1974) page 36, to maximise gain at the expense of high sidelobe levels. The subreflector edge illumination is 5,5 dB below the central value, while the space attenuation at the paraboloid edge is -3,0 dB, giving a final paraboloid edge illumination 8,5 dB below the central value. The shape of the aperture distribution is closely approximated by (Hansen, 1964, pages 64-7)

$$P(r) = 0,5 + 0,5\ (1 - r^2) \qquad 6.12$$

where r = fractional distance from aperture centre.
Assuming the antenna to be ideal, its beam pattern may be derived from this as the Fourier transform of the pattern is proportional to the complex autocorrelation function of the aperture distribution.

The characteristics of the computed best-fit beam model are compared in table 6.1 with the beam pattern of an ideal antenna with the aperture illumination given by equation 6.12, and with that of an ideal antenna with uniform illumination. The low gain of the antenna is evident, the gain being proportional to the aperture efficiency. The beam is broader than expected and the first sidelobe stronger; however the model beamwidth is probably larger than the real value owing to the scaling and non-linearity problems. Using the corrections detailed in section 5.7, a value of $0,453^{\circ}$ was obtained for θ_A from lunar observations, in good agreement with the predicted figure of $0,46^{\circ}$

Model:	computed best-fit	ideal antenna $0,5+0,5(1-r^2)$ illum.	ideal antenna uniform illum.
relative gain	0,47	0,92	1,0
θ_A (^{o})	0,54	0,46	0,415
first null (^{o})	0,58	0,54	0,497
first sidelobe (dB)	-13,5	-22,0	-17,6
second sidelobe (dB)	-22,5	-	-23,7
third sidelobe (dB)	-31,0	-	-

Table 6.1 Antenna Beam Characteristics

although the correction assumes a Gaussian mainlobe.

Several factors combine to reduce the gain and increase the sidelobe level. These are discussed below and include the Cassegrain geometry, aperture blocking by the subreflector and its supports, random surface errors, and defocusing.

(a) Antenna configuration The maximum possible efficiency of a Cassegrain antenna employing conventional paraboloid and hyperboloid surfaces has been estimated as 78% of that of an ideal antenna, although up to 98% is possible if specially shaped surfaces are used (Williams, 1965).

(b) Aperture blockage The subreflector causes a central, circular 'hole' in the aperture illumination pattern, which can be treated relatively easily owing to its circular symmetry. Hannan (1961) gives the ratio of the 'hole' pattern peak to the original pattern peak as

$$E_b/E_m = 2\ (d_b/d_m)^2 \qquad 6.13$$

where d_b=blocked aperture diameter (0,21 m)

d_m = full aperture diameter (1,86 m)

This gives a gain reduction of 6%, and an increase in first sidelobe level of 2,5 dB. Hansen (1964) page 73 quotes a corresponding gain loss of 5% and a first sidelobe increase of 3 dB.

The quadrupod subreflector support causes an asymmetric increase in sidelobe level as it does not possess circular symmetry. The power loss due to its aperture blocking is equal to the fractional area blocked, which amounts to 3,5% in this case. However there is an extra loss due to the wave diffracted from the upper strut of each pair being blocked by the lower strut (Rusch, 1974), which probably adds about 50% to the effective blocking area, giving a total loss of approximately 5%.

(c) Reflector surface errors The efficiency is reduced by random errors on the reflector surfaces, the magnitude of which were discussed in chapter two. Allowing for the aperture illumination taper, which reduces the effect of irregularities towards the dish edge, the mean r.m.s. surface error $< \varepsilon^2 >$ was approximately 0,2 mm during initial use, and 0,07 mm after reshimming the paraboloid. The correlation length C of the irregularities is of the order of 20 cm. Following the method of Baars (1973), these errors cause an r.m.s. phase fluctuation δ in the reflected wave, over the aperture, of

$$\delta = 4\pi \ (< \varepsilon^2 >)^{\frac{1}{2}} / \lambda \qquad 6.14$$

$$= 0,42 \text{ initially and } 0,25 \text{ after reshimming.}$$

The resulting error beam pattern has a Gaussian shape with a half power width $\theta_e = 0,43\lambda / C = 2^o$ 6.15

If ε_{apo} is the aperture efficiency when there are no surface errors, the actual aperture efficiency is ε_{ap}, where

$$\varepsilon_{ap} = \varepsilon_{apo} \exp(-\delta^2) \qquad 6.16$$

$$= 0{,}84\ \varepsilon_{apo} \text{ initially}$$

$$= 0{,}94\ \varepsilon_{apo} \text{ after reshimming}$$

Consequently an improvement in aperture efficiency of 12% was predicted from surface measurements following the refiguring of the paraboloid. In practice there was a greater improvement, due to better focusing of the antenna during its later use. The peak level of the error beam compared to the main beam is given by

$$f_e(o)/f_d(o) = 4c^2(\exp(\delta^2)-1)\ /(\varepsilon_{apo}\ d^2) \qquad 6.17$$

$$= -\ 18 \text{ dB initially}$$

$$= -\ 23 \text{ dB after reshimming.}$$

Comparison of these results with the computed best-fit beam model indicates that the peak value of the error beam has been calculated fairly accurately, as the power level at the first null of the model is approximately -16 dB. However the error beam appears to be much narrower than expected, as subsequent nulls are still clearly visible. This may indicate that the correlation length is greater than expected, or that the nulls between sidelobes have been overestimated (figure 6.4).

A further error beam is generated by the subreflector surface irregularities, but these are relatively small (0,03 mm r.m.s.) compared to those of the paraboloid. The main hyperboloid surface error is non-random (figure 2.12) and although this will affect the gain and sidelobe levels it cannot be treated by the random error method.

Gravitational deformation of the antenna causes semi-regular elevation-dependent paraboloid surface errors (section 2.10), which might be detected by mapping the beam pattern over a range of elevations.

(d) Defocusing Axial and radial defocusing and astigmatism all lower the efficiency. Cassegrain antennas are relatively insensitive to radial defocusing, but axial defocusing can cause an appreciable loss of gain (Baars, 1973). The subreflector is currently estimated to be within 2 mm of its correct axial location. According to Baars, an error of this magnitude would cause a 2% gain loss, and an increase in the first sidelobe level of about 1 dB. In contrast, the method of Rusch and Potter (1970), page 90, gives a gain reduction of up to 8%. A nominal value of 5% has been assumed.

Astigmatism cannot be eliminated through focusing (Cogdell and Davis, 1973), being due to a 'squeezing' of the reflector at opposite edges. This could occur when the paraboloid is pointing away from the zenith, caused by gravitational sag. It is most easily evaluated by measurement of beam broadening, half-power beam widths being measured along two perpendicular axes.

The reductions in gain, or efficiency, caused by the factors described above are summarised in table 6.2. The efficiency loss factors are multiplicative, and the aperture efficiency after allowing for each factor is given. The measured initial aperture efficiency was $0,47 \pm 0,05$ compared to the predicted value of 0,51, and that after refiguring was $0,57 \pm 0,04$, with 0,58 predicted. The same defocusing loss has been assumed, although it was reduced after the refiguring of the paraboloid. The close agreement between the predicted and calculated gains is probably fortuitous in view of the uncertainties involved.

Antenna factor	Efficiency loss (%)	Aperture efficiency
ideal antenna	0	1,00
conventional Cassegrain	22	0,78
aperture illumination	8	0,72
subreflector blockage	5	0,68
support blockage	5	0,65
surface error, initial	16	0,54
defocusing, initial	5	0,51
surface error, later	6	0,61
defocusing, later	5	0,58

Table 6.2 Loss of Efficiency in the Antenna

CHAPTER SEVEN

A SUMMARY OF THE TELESCOPE DEVELOPMENT

The aperture efficiency of the telescope has been raised from 0,47 to 0,57, primarily through re-shimming the paraboloid. Contour maps of the paraboloid surface indicated that the r.m.s. error has been reduced to less than $\lambda/32$, while the subreflector surface is of similar accuracy. Gravitational and thermal deformations of the antenna have been analysed and found to be similar in magnitude to the random surface errors.

The front end design and its improvement have been discussed, and the mixer performance measured. The operation of both the receiver back ends has been described and the predicted sensitivity compared to that obtained. The results of solar and lunar observations and atmospheric attenuation measurements are in agreement with those of other authors. They have been used to find the efficiency of the system and the antenna beam pattern, for which a computer program was developed. The causes of inefficiency in the antenna have been analysed and the predicted efficiency compared to that deduced from observations.

In its present form the telescope is immediately useful for monitoring the sun for flares, and for a reliable determination of the variation and phase lag of the lunar temperature. Accurate measurements of the sky temperature and atmospheric attenuation could be carried out simultaneously. When source-tracking is available further continuum and spectral line observations become possible.

The usefulness of the telescope would be greatly enhanced by a move to a less obstructed site where viewing is possible to the

horizon. An earth-bound far-field transmitter could then be used for gain and sidelobe measurements. The sidelobe levels would be significantly improved by the use of higher gain, narrower-beam horns to increase the aperture illumination taper. The only front end modification necessary would be the shortening of the waveguide to the horns, to keep their apertures in the antenna focal plane. Two more expensive alternatives are possible for improvement of the telescope viability, namely the replacement of the antenna with one of a larger diameter, or the use of a maser amplifier in the front end. Those available at this frequency typically have an effective temperature of 100 K and 25 MHz bandwidth (Hills et al., 1973). This would increase the spectral line receiver sensitivity by a factor of ten, and triple that of the continuum receiver.

LITERATURE CITED

Baars, J.W.M. (1970). Dual-beam parabolic antennae in radio astronomy. Wolters-Noordhoff, Groningen.

Baars, J.W.M. (1973). "The measurement of large antennas with cosmic radio sources," IEEE Trans. Antennas Propagat. AP-21, 461-74.

Baars, J.W.M. (1976). Private Communication.

Baart, E.E. (1975). Private Communication.

Benson, F.A. (1969). Millimetre and submillimetre waves. Iliffe books Ltd., London.

Beste, J.M. et al. (1974). Microwave antenna measurements. Scientific-atlanta, Atlanta, Georgia.

Bolz, R.E. and Tuve, G.L. (1973). Handbook of tables for applied engineering science. CRC Press, Cleveland, Ohio.

Bracewell, R.N. and Roberts, J.A. (1954). "Aerial smoothing in radio astronomy," Aust.J. Phys. 7, 615-40.

Burr, E.J. (1955). "Sharpening of observational data in two dimensions," Aust.J. Phys. 8, 30-53.

Carli, B. (1974). "Design of a blackbody reference standard for the submillimeter region," IEEE Trans.Mic.Theory Tech. MTT-22, 1094-9.

Castelli, J.P., Guidice, D.A. and Kalaghan,P.M. (1974). "Millimeter wave solar observations," IEEE Trans. Mic. Theory Tech. MTT-22, 1292-9.

Cogdell, J.R. and Davis, J.H. (1973). "Astigmatism in reflector antennas," IEEE Trans. Antennas Propagat. AP-21, 565-7.

Collin, R.E. (1970). Foundations of microwave engineering. McGraw-Hill, New York.

Conway, R.G. (1963). "Measurements of radio sources at centimetre wavelengths," Nature 199, 1177.

Cowles, P.R. and Parker, E.A. (1975). "Reflector surface error compensation in Cassegrain antennas," IEEE Trans.Antennas Propagat. AP-23, 323-8.

Crane, R.K. (1971). "Propagation phenomena affecting satellite communication systems operating in the centimeter and millimeter wavelength bands," Proc. IEEE 59, 173-88.

Duncan, J. (1949). Applied mechanics for engineers. Macmillan & Co., London.

Efanov, V.A. and Moiseev, I.G. (1971). "Observations of the solar radio emission at 8,13 and 15 mm," Izv. Krymskoj Astrofiz. Obs. 43, 21-5.

Elzner, L.R. (1976). "The centre-to-limb variation of optically thin uv-lines and at centimetric wavelengths and the influence of spicules," Astron. Astrophys. 47, 9-18.

Emerson, W.H. (1973). "Electromagnetic wave absorbers and anechoic chambers through the years," IEEE Trans. Antennas Propagat. AP-21, 484-90.

Findlay, J.W. (1971). "Filled aperture antennas for radio astronomy," Ann.Rev. Astron. Astrophys. 9, 271-92.

Findlay, J.W. and Payne, J.M. (1974). "An instrument for measuring deformations in large structures," IEEE Trans. Instrum. Meas. IM-23, 221-6.

Fogarty, W.G. (1975). "Total atmospheric absorption at 22.2 GHz," IEEE Trans. Antennas Propagat. AP-23, 441-4.

Fürst, E., Hachenberg , O. and Hirth, W. (1974). "The centre-to-limb variation of the sun at centimetric wavelengths," Astron. Astrophys. 36, 123-33.

Greve, A. (1975). "On the limitations of surveying radio reflectors by geodetical methods," Technischer Bericht Nr 32. Max-Planck-Institut für Radioastronomie, Bonn.

Goss, W.M., Knowles, S.H., Balister, M., Batchelor, R.A. and Wellington, K.J. (1976). "A survey of H_2O sources for wide-spectrum emission," Mon.Not. R.A.S. 174, 541-53.

Haar, D. ter and Pelling, M.A. (1975). "Interstellar hydroxyl and water masers and formaldehyde masers and dasars," Rep.Prog. Phys. 37 481-561.

Hachenberg, O., Grahl, B.H. and Wielebinski, R. (1973). "The 100-meter radio telescope at Effelsberg," Proc. IEEE 61, 1288-95.

Hagfors, T. (1971). "Microwave studies of thermal emission from the moon," Advan. Astron. Astrophys. 8, 1-28.

Hannan, P.W. (1961). "Microwave antennas derived from the Cassegrain telescope," IRE Trans. Antennas Propagat. AP-9, 140-53.

Hansen, R.C. (1964). Microwave scanning antennas, Volume 1, Apertures. Academic Press, New York.

Haroules, G.G. and Brown III, W.E. (1969). "The simultaneous investigation of attenuation and emission by the earth's atmosphere at wavelengths from 4 centimeters to 8 millimeters," J. Geophys. Res. 74, 4453-71.

Harvey, A.F. (1963). Microwave engineering. Academic Press, London.

Hills, R.E., Janssen, M.A., Thornton, D.D. and Welch, W.J. (1973). "The Hat Creek millimeter-wave interferometer," Proc. IEEE 61, 1278-82.

Janssen, M.A., Golden, L.M. and Welch, W.J. (1974). "Extension of the absolute flux density scale to 22,285 GHz," Astron. Astrophys. 33, 373-7.

Joshi, J.S. and Cornick, J.A.F. (1973). "Some general observations on the tuning characteristics of 'electromechanically' tuned Gunn oscillators," IEEE Trans. Mic. Theory Tech. MTT-21, 582-6.

Kraus, J.D. (1966). Radio Astronomy. McGraw-Hill, New York.

Krotikov, V.D. and Schuko, O.B. (1965). "Allowance for the averaging action of the antenna directivity diagram in measurements of lunar

radio emission," Astron. Zh. 42, 145-7.

Kundu, M.R. and Velusamy , T. (1974). "Fine structure of the sun at 1,3 cm wavelength ," Solar Phys. 34, 125-31.

Linsky, J.L. (1973). "The moon as a proposed radiometric standard for microwave and infrared observations of extended sources ," Astrophys. J. Suppl.25, 163-204.

Lo, K.Y., Burke, B.F. and Haschick, A.D. (1975). "H_2O sources in regions of star formation," Astrophys. J. 202, 81-91.

Mar. J.W. and Liebowitz, H. (1969). Structures technology for large radio and radar telescope systems. MIT Press, Cambridge, Mass.

Mutch, L.I. (1975). A 22 GHz radio telescope. M.Sc. thesis, Rhodes University.

Nunn, B.J. (1974). A 22 GHz water maser radiometer. M.Sc. thesis, Rhodes University.

O'Brien, K.C.,Heidt, R.C. and Owens , G.J. (1972). "A transportable 16 GHz solar telescope for atmospheric transmissivity measurements," Radio Sci. 7, 215-21.

Olson, K.W. (1971). "Apparent frequency dependence of the microwave power radiated from gas discharge noise sources,"IEEE Trans. Mic. Theory Tech. MTT-19, 776-8.

Payne, J.M., Hollis, J.M. and Findlay, J.W. (1976). "New method of measuring the shape of precise antenna reflectors," Rev. Sci. Instrum. 47, 50-5.

Rusch, W.V.T. and Potter, P.D. (1970). Analysis of reflector antennas. Academic Press, New York.

Rusch, W.V.T. (1974). "Double aperture blocking by two wavelength sized feed-support struts," Electron. Let. 10, 296.

Ruze, J. (1966). "Antenna tolerance theory - a review," Proc. IEEE 54, 633-40.

Schwartz, P.R. and Barrett, A.H. (1970). "Observations of water-vapour emission associated with infrared stars," Astrophys. J. Lett. Ed. 159, L123-7.

Shimabukuro, F.I. and Stacey, J.M. (1968). "Brightness temperature of the quiet sun at centimeter and millimeter wavelengths," Astrophys. J. 152, 777-82.

Silver, S. (1965). Microwave antenna theory and design. Dover, New York.

Skolnik, M.I. (1970). Radar handbook. McGraw-Hill, New York.

Slobin, S.D., Rusch, W.V.T., Stelzried, C.T. and Sato, T. (1970). "Beam switching Cassegrain feed system and its applications to microwave and millimeterwave radioastronomical observations," Rev. Sci. Instrum. 41, 439-43.

Staelin, D.H. (1966). "Measurements and interpretation of the microwave spectrum of the terrestrial atmosphere near 1-centimeter wavelength," J. Geophys. Res. 71, 2875-81.

Staelin, D.H., Gaut, N.E., Law, S.E. and Sullivan III, W.T. (1968). "Spectrum measurements of the sun near 1 cm wavelength," Solar Phys. 3, 26-7.

Staelin, D.H. (1969). "Passive remote sensing at microwave wavelengths," Proc. IEEE 57, 427-39.

Stutzman, W.L. and Ko, H.C. (1974). "On the measurement of antenna beamwidth using extraterrestrial radio sources," IEEE Trans. Antennas Propagat. AP-22, 493-5.

Sullivan III, W.T. (1971). "Variations in frequency and intensity of 1.35 centimeter H_2O emission profiles in Galactic H II regions," Astrophys. J. 166, 321-32.

Sullivan III, W.T. (1973). "Microwave water vapour emission from galactic sources," Astrophys. J. Suppl. 25, 393-432.

Wasburn, E.W. (1926). International critical tables, Volume 1. McGraw-Hill, New York.

Williams, W.F. (1965). "High efficiency antenna reflector," Microwave J. 8, 79-82.

Wrixon, G.T. and Hogg, D.C. (1971). "Absolute measurements of solar flux at 16 and 30 GHz," Astron. Astrophys. 10, 193-7.

Wrixon, G.T., Welch, W.J. and Thornton D.D. (1971). "The spectrum of Jupiter at millimeter wavelengths," Astrophys. J. 169, 171-83.

Zhuravlev, V.S., Petrovskii, A.A. and Pogrebnyi, B.P. (1966). "The 15-m universal radio telescope," Soviet Astron.-AJ 10, 176-80.

APPENDICES

2a Thermal effects in the paraboloid survey.

2b Antenna structure deformation.

2c Antenna structure deformation by subreflector supports.

3a Specifications of microwave components.

3b Production of waveguide bends.

4a Specifications of intermediate frequency components.

6a Listing of program CONVOLVE.

APPENDIX 2a

Thermal effects in the Paraboloid Survey

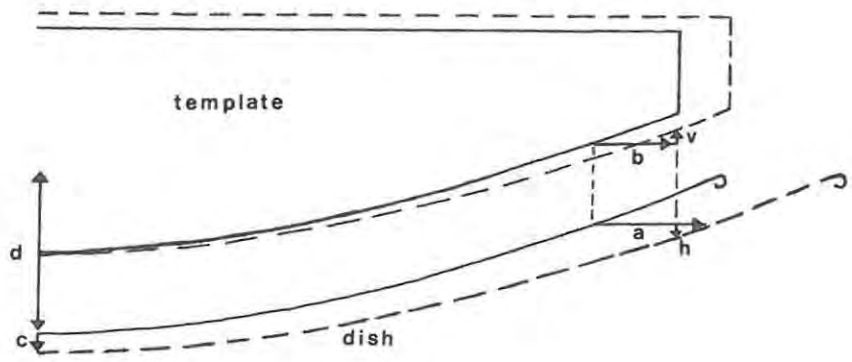

Exaggerated Paraboloid and template thermal expansion.

Vertical expansion of the dish at its centre causes an increase c in the depth d for a temperature rise t given by

$$c = \alpha_{Al}\, d\, t$$

$$= 0{,}0075 \text{ mm } K^{-1}.$$

At its rim the dish expands horizontally a distance a where

$$a = \alpha_{Al}\, r\, t$$

$$= 0{,}025 \text{ mm } K^{-1}$$

and the template expands laterally a distance b where

$$b = \alpha_{Fe}\, r\, t$$

$$= 0{,}012 \text{ mm } K^{-1}$$

The relative horizontal expansion e = a - b.

As the dish surface is at a 30° angle to the horizontal near its rim, this causes an apparent increase in depth h at the measuring radius of

$$h = e \tan 30^{o}$$

$$= 0{,}0075 \text{ mm K}^{-1}$$

The vertical expansion v of the template is given by

$$v = \alpha_{Fe}\, dt$$

$$= 0{,}0035 \text{ mm K}^{-1}$$

The relative change in height at the dish centre is c, and at the dish edge it is v + h. The difference between these gives the actual change in the reading; as c is numerically equal to h, to a first approximation the change in reading is given by the vertical template expansion alone, or 0,0035 mm K^{-1}.

APPENDIX 2b

Antenna structure deformation

The contraction e when a force F is applied longitudinally to one end of a beam of length L, Young's modulus E, and cross sectional area A is given by $e = Fl/EA$.

The dish support framework is made of square section steel tube, 25,4 mm outside dimension and 1,6 mm thickness, giving a cross-sectional area of steel of 160 mm^2. Beam lengths in the large octagon and its supports from the small octagon are approximately 0,8 m. Young's modulus for steel is $2 \times 10^{11} Nm^{-2}$ (Bolz and Tuve, 1973, page 118). For a 10 N force the beam compression would be $2,5 \times 10^{-7}$ m.

The deflection d of a structural beam is given by equation 2.6, where the moment of inertia I for square section tube is given by Duncan, (1949), page 151 as

$$I = (B^4 - b^4)/12$$

where B = external dimension.

b = internal dimension of cross section.

For the beams used $I = 1,22 \times 10^{-8} m^4$

For a 10 N force the beam deflection would be $2,1 \times 10^{-4}$ m; consequently the bending to compression ratio is approximately 10^3 for a given force.

APPENDIX 2c

Antenna structure deformation by subreflector supports.

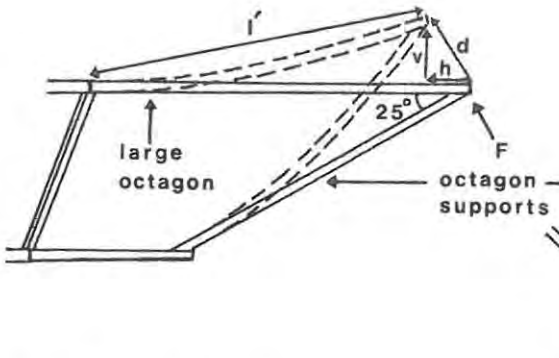

Figure 1 Side View

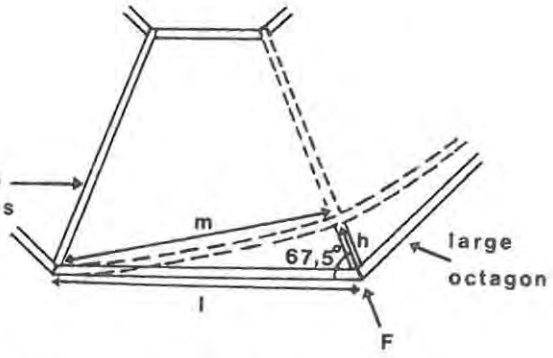

Figure 2 Top View

Exaggerated octagon support deflection by force F.

The weight of the subreflector structure acts nearly normally to the octagon supports. We wish to find how the octagon is likely to deform under these forces. Initially assume that the octagon arms are free to contract or expand longitudinally, and let the octagon support, which is at 25° to the octagon plane, be deflected a distance d by the force F (figure 1). The deflection has horizontal and vertical components h and v respectively, where

$$h = d \sin 25^{\circ}$$

$$v = d \cos 25^{\circ}$$

The component of the octagon arm, of normal length l, in the octagon plane is now m, (figure 2), where

$$m^2 = l^2 + h^2 - 2lh \cos 67,5^{\circ}.$$

Hence the actual arm length l´can be found from its horizontal and vertical components m and v:

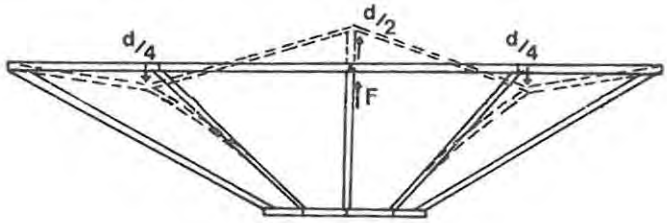

Figure 3 Octagon deformation by force F

$$1' = (m^2 + v^2)^{\frac{1}{2}}$$

$$\text{or } 1' = (1^2 - 0{,}32\ 1d + d^2)^{\frac{1}{2}}$$

for $d << 1$ $1' = 1 - 0{,}16d$.

Similarly, if the support is deflected downwards, $1'' = 1 + 0{,}16d$.

These equations give the linear distance between the deflected joint and neighbouring undeflected ones. Two corrections may be applied owing to the joint rigidity, and support and octagon arm curvature after deflection, but these are negligible for $d << 1$.

The net result is that the deflection of the octagon joint should cause a change in length of the two octagon arms to the joint which is proportional to the deflection. The force F does in fact cause a total deflection d, but in order to keep the octagon arm lengths constant (appendix 2b) this is spread over three joints. The deflection is now made up of d/2 at the joint to which the force is applied, and -d/4 at both the neighbouring joints (figure 3). The octagon arms to the joint being considered now have a length of $1 - 0{,}08d + 0{,}04d$, or $1 - 0{,}04d$, while the arms to the neighbouring joints have a length $1 + 0{,}04d$. The neighbouring joints are consequently bent sideways away from the centre joint by $0{,}04d$, to restore both arms to the original length 1. Part of the force F is required to do this, but as it is less than F/10 it is neglected.

APPENDIX 3a

Specifications of Microwave Components

K-band mixer:

Aerojet General, El Monte, California.

Model No. 1000 K Serial No. 4020

Operating range : 20 - 24 GHz

Input VSWR < 1,5 at 22,235 GHz

l.o. r.f. isolation > 18 dB

i.f. gain > 35 dB

noise figure : 4,4 dB (22 GHz); 4,3 dB (23 GHz)

Microwave switch:

Electromagnetic Sciences Inc., Atlanta, Georgia.

Model No. 560 - A1 Serial No. 10

Operating range : 21,6 - 22,8 GHz

Insertion loss $\leqslant$ 0,3 dB

Isolation $\geqslant$ 20 dB

VSWR $\leqslant$ 1,25

Maximum switch rate : 10 kHz

Switchable circulator:

Sonoma Engineering and Research Inc., Santa Rosa, California.

Model No. S4712 Serial No. 1

Operating range : 21,2 - 23,2 GHz

Insertion loss < 0,4 dB

Isolation > 20 dB

Argon Gas Discharge Tube:

Mid-Century Microwavegear Ltd., Croydon, England.

Tube : BS 386 (English Electric Valve) Serial No. 24322

Power Supply : EE/7A

ENR : 16,4 dB

VSWR : < 1,25

Gunn diodes:

Varian Inc., Palo Alto, California.

Type VSK-9014 L Serial No. 9E

Power output : 61 mW at 22,23 GHz

Type VSK- 9014S Serial No. 22E

Power output : 49 mW at 22,2 GHz (measured)

Mechanical tuning : 21,8 - 22,6 GHz (measured)

Mid-Century Microwavegear Ltd.

Type MC 20/34B Serial No. 1953

Power Output : 135 mW at 22,2 GHz (measured)

Mechanical tuning : 18,0 - 24,4 GHz

APPENDIX 3b

Production of Waveguide Bends

A length of straight waveguide, rectangular section copper or brass tube, is cut slightly overlong, cleaned internally and annealed. A flange is silver-soldered to one end, which is trimmed flush with the flange face. Thorough internal cleaning of the waveguide between all operations proved to be essential as the presence of foreign matter leads to pitting of the surface. Woods metal, a low melting-point lead-based alloy, is melted in a waterbath and poured into the prewarmed waveguide, the lower flange being immersed in cold water. The waveguide should fill uniformly with the metal.

The flange is screwed to a steel jig and hardwood formers of the upper and lower shape of the waveguide are produced from a drawing of the complete component. After bending the waveguide to their shape the Woods metal is removed with boiling water. The waveguide is replaced in the jig and a moveable upright used to locate the second flange in position, which is then silver-soldered on. The waveguide is trimmed flush with the flange face, cleaned with etching acid and polished internally and on the flange faces.

A similar procedure is used for bending waveguide at the National Institute for Telecommunications Research, Johannesburg.

APPENDIX 4a

Specifications of Intermediate Frequency Components

1 - 2 GHz mixer and preamplifier

RHG Electronics Laboratory, Inc., New York.

Model No. MP 1-2/2C Serial No. 7-590-1

i.f. centre frequency : 30 MHz

i.f. bandwidth : 12 MHz

r.f. - i.f. power gain : 28 dB

noise figure : 6,5 dB at 1,5 GHz

Wideband i.f. amplifier

Trontech Inc., Deal, New Jersey.

Model No. W150 A Serial No. 012

1 dB bandwidth : 5-175 MHz

Gain : 61 dB

noise figure : 1,3 - 1,4 dB

1 dB compression point : + 18 dBm

Narrowband i.f. amplifier

RHG Electronics Laboratory, Inc., New York.

Model No. EST 3010 Serial No 7-093-1

Centre frequency : 30 MHz

3 dB bandwidth : 10,5 MHz

Max. power gain : 80 dB

1 dB compression point : + 14 dBm

AGC time constant : 15 µs

AGC compression ratio : 60 dB / 1,5 dB

APPENDIX 6a

Listing of Program CONVOLVE

```
      TRACE 2
      SHORTLIST
      MASTER CONVOLVE
      DIMENSION Z(900),V(900),VOLEX(900)
C     NP=NUMBER OF POINTS DEFINING BEAM PATTERN
C     KK=NEAREST LOWEST MULTIPLE OF 10 TO NP
C     KJ=NP-KK
C     Z(N)=BEAM POWER FOR R BETWEEN N AND N-1 *DELR  N=1,NP
C     KEY=1 AT START OF EACH SET OF DATA  KEY=0 TO TERMINATE
C     DELR=DISTANCE BETWEEN POINTS DEFINING BEAM
C          IN DECIMALS OF A DEGREE
C     DEC=DECLINATION OF OBJECT IN DEGREES
C     RMIN=MINIMUM DISTANCE OF APPROACH OF OBJECT
C          TO BEAM CENTRE IN DEGREES
C          NEGATIVE IF BEAM FURTHER FROM NEARER POLE THAN OBJECT
C          POSITIVE IF BEAM CLOSER TO NEARER POLE THAN OBJECT
C     RO=RADIUS OF OBJECT IN DEGREES
C     DELT=TIME INTERVAL BETWEEN POINTS ON
C          CONVOLUTION ENVELOPE IN SECONDS
C
      READ(5,100)KK,KJ
      READ(5,101)(Z(N),N=1,KK)
      IF (KJ-0)2,2,1
    1 READ(5,102)(Z(N+KK),N=1,KJ)
    2 READ(5,99)KEY
      IF(KEY-0)330,330,3
    3 READ(5,103)DELR,DEC,RMIN,RO,DELT
      WRITE(6,104)DEC
      WRITE(6,105)RMIN
      WRITE(6,106)RO
      WRITE(6,107)DELT
      WRITE(6,108)
      DO 7 N=1,900
      V(N)=0
    7 VOLEX(N)=0
      NP=KK+KJ
      DEC=ABS(DEC)*0.017453293
      CRM=COS(RMIN*0.017453293)
      CD=COS(DEC)
      CDR=COS(DEC+RMIN*0.017453293)
      SD=SIN(DEC)
      DELQ=DELT/240.0*0.017453293
      MM=1
      Q=3.1415927
    8 CQ=COS(Q)
      RD=ACOS(CRM-CD*CDR*(1.-CQ))
      RD=RD*57.29578
   10 RT=RD-RO
      RS=RD+RO
      IF(RT-(NP*DELR))20,310,310
   20 IF(RT-0)30,30,150
   30 AB=ABS(RT)/DELR
      II=INT(AB)
      IF(AB-(II+0.5))50,40,40
   40 JJ=II
      GO TO 60
   50 JJ=II-1
   60 VDASH=3.1415927*DELR*DELR*Z(1)
      K=1
   70 IF(K-JJ)80,80,90
```

```
 80 VDASH=VDASH+6.2831854*DELR*DELR*(K+0.5)*Z(K+1)
    K=K+1
    GO TO 70
 90 M=2
    I=JJ+1
    GO TO 200
150 VDASH=0.0
    N=NP-1
155 IF(RT-(N*DELR))160,160,170
160 N=N-1
    GO TO 155
170 IF(RT-((N+0.5)*DELR))190,190,180
180 I=N+1
    GO TO 195
190 I=N
195 M=I
200 IF(RS-(M*DELR))220,220,210
210 M=M+1
    IF(M-NP)200,220,220
220 IF(RS-((M-0.5)*DELR))230,240,240
230 J=M-2
    GO TO 250
240 J=M-1
250 IF(I-J)270,270,260
260 V(MM)=VDASH
    GO TO 295
270 K=I
    VOL=0.0
275 G=(K+0.5)*DELR
    H=(RD*RD+G*G-RO*RO)/(2.0*G*RD)
    THETAK=2.0*ACOS(H)
    RLK=G*THETAK
    VK=Z(K+1)*RLK*DELR
    VOL=VOL+VK
    IF(K-J)280,290,290
280 K=K+1
    GO TO 275
290 V(MM)=VOL+VDASH
295 VOLEX(MM)=10.0**V(MM)
    MM=MM+1
310 Q=Q-DELQ
    IF(Q-0)325,325,8
325 IX=MM/3
    IY=IX*3+3
    WRITE(6,109)(V(N),VOLEX(N),N=1,IY)
    GO TO 2
330 STOP
 99 FORMAT(I0)
100 FORMAT(2I0)
101 FORMAT(10E0.0)
102 FORMAT(E0.0)
103 FORMAT(5E0.0)
104 FORMAT(1H1,40X,14HDECLINATION  =,F15.4)
105 FORMAT(1H0,40X,14HMIN APPROACH =,F15.4)
106 FORMAT(1H0,40X,15HOBJECT RADIUS =,F14.4)
107 FORMAT(1H0,40X,15HTIME INTERVAL =,F14.4)
108 FORMAT(1H0//1H ,3(8X,4HLOGV,18X,1HV,9X))
109 FORMAT(6E20.4)
    END
```